PFC/RR-88-12

DOE/ET-51013-255
UC420

Methods for the Design and Optimization of Shaped Tokamaks

Scott William Haney

May 1988

Plasma Fusion Center
Massachusetts Institute of Technology
Cambridge, Massachusetts 02139 USA

METHODS FOR THE DESIGN AND OPTIMIZATION OF SHAPED TOKAMAKS

by

SCOTT WILLIAM HANEY

B.S., Physics and Nuclear Engineering
University of California, Santa Barbara
(1983)

Submitted to the Department of Nuclear Engineering
in partial fulfillment of the requirements for the degree of

Doctor of Philosophy

at the

MASSACHUSETTS INSTITUTE OF TECHNOLOGY

May 1988

Signature of Author .....
Department of Nuclear Engineering
May 5, 1988

Certified by .....
Jeffrey P. Freidberg
Professor of Nuclear Engineering
Thesis Supervisor

Accepted by .....
Allen F. Henry
Chairman, Departmental Committee on Graduate Students

METHODS FOR THE DESIGN AND OPTIMIZATION OF SHAPED TOKAMAKS

by

SCOTT WILLIAM HANEY

Submitted to the Department of Nuclear Engineering
on May 5, 1988, in partial fulfillment of the
requirements for the degree of
Doctor of Philosophy

Abstract

Two major questions associated with the design and optimization of shaped tokamaks are considered. (1) How do physics and engineering constraints affect the design of shaped tokamaks? (2) How can the process of designing shaped tokamaks be improved? The first question is addressed with the aid of a completely analytical procedure for optimizing the design of a resistive-magnet tokamak reactor. It is shown that physics constraints — particularly the MHD beta limits and the Murakami density limit — have an enormous, and sometimes, unexpected effect on the final design. The second question is addressed through the development of a series of computer models for calculating plasma equilibria, estimating poloidal field coil currents, and analyzing axisymmetric MHD stability in the presence of resistive conductors and feedback. The models offer potential advantages over conventional methods since they are characterized by extremely fast computer execution times, simplicity, and robustness. Furthermore, evidence is presented that suggests that very little loss of accuracy is required to achieve these desirable features.

Thesis Supervisor: Jeffrey P. Freidberg
Title: Professor of Nuclear Engineering

Acknowledgements

I would like to dedicate this thesis to the numerous people who have helped me to complete my education at M.I.T.

First and foremost, I would like to thank my advisor, Prof. Jeffrey P. Freidberg, for the four delightful years I have spent doing research under his supervision. His generous willingness to spend many hours discussing plasma physics and engineering have proved to be an invaluable part of my graduate education. In addition, I will always be in debt to Prof. Freidberg for his good advice and support during the past four years.

I would also like to acknowledge several other faculty members in the Department of Nuclear Engineering — Dr. Daniel Cohn, Prof. Mujid Kazimi, Prof. Ian Hutchinson, and Prof. Dieter Sigmar — for their efforts on my behalf both inside and outside the classroom.

I would like to express my appreciation to Dr. Daniel Cohn, Prof. Ian Hutchinson, and Dave Humphreys for reading parts of the thesis manuscript. Their constructive criticisms greatly improved the quality of this work.

During my years as a graduate student, I have had the opportunity to visit other institutions and to interact with a number of extremely talented researchers. I would specifically like to thank Dr. John Perkins, Dr. Max Fenstermacher, and Dr. Bob Campbell at Lawrence Livermore National Lab. and Dr. Joanne Helton and Dr. Alan Turnbull at GA Technologies, Inc. for spending time with me and making my experiences at LLNL and GA technologies, Inc. fun and intellectually exciting.

I am grateful to my friends at the M.I.T. Plasma Fusion Center — Jim Crotinger, Dave Humphreys, Dr. Pekka Hakkarainen, Manos Chaniotakis, and Ron Miller — for many great times. My dear friends Brad and Elizabeth Valenti have also been a constant source of much needed support.

I would also like to acknowledge the financial support I received from the U.S. Department of Energy: this research was performed in part in conjunction with the Magnetic Fusion Energy Technology Fellowship Program with is administered for the United States Department of Energy by Oak Ridge Associated Universities.

Finally, I would like to thank my parents and my brother for their continued support and love during my seemingly endless years in school.

Scott W. Haney

Contents

List of Tables

List of Figures

Chapter 1

Introduction

This thesis is concerned with the design and optimization of tokamaks, particularly those possessing relatively complicated cross-sectional shapes of the type shown in Fig. 1.1. In the plot, a is the plasma minor radius, R_0 is the plasma major radius, κ_a is the plasma elongation, and δ_a is the plasma triangularity.

Two major questions will be addressed:

- How do physics and engineering constraints affect the design of shaped tokamaks?
- How can we improve the process of designing shaped tokamaks?

The first question is an extremely basic one. Unfortunately, the answer is quite dependent on the type of device being considered. For the purposes of this thesis, we focus on the resistive-magnet tokamak reactor concept. We will show, using a completely analytic procedure, that the physics and engineering constraints have an enormous, and in some cases unexpected, impact on the final design.

The answer to the second question is somewhat subjective. However, one appealing argument goes as follows. In the process of designing a tokamak, it

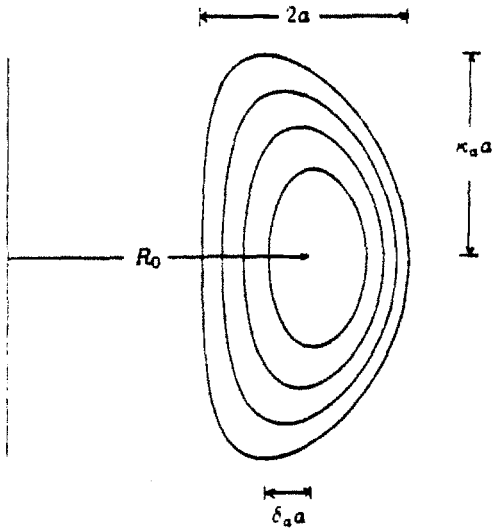

Figure 1.1: *Shaped tokamak geometry.*

is generally necessary to systematically vary a large number of parameters in order to find the optimal set. With this thought in mind, it would be desirable if the computer codes used to calculate a particular design were (a) fast, (b) easy to use, (c) robust, and (d) accurate. In the fusion community today, there exists a number of computer codes that very accurately solve many problems related to the design of shaped tokamaks. Unfortunately, shaped tokamaks are inherently very complicated devices. As a result, the computer codes that scientists and engineers use to study them have necessarily become quite complex as well. This complexity tends to make the codes relatively difficult for users to learn and to use. Furthermore, even with the extreme speed of modern supercomputers, execution times for many codes range from several seconds to as long as several hours. All of these issues make the careful examination of parameter space more difficult. Therefore, from the point of view of the tokamak designer, it may be valuable to have access to codes that are somewhat less accurate but much faster, simpler, and more robust.

In this thesis, we will propose methods for creating such codes in the areas of

- Plasma equilibrium generation,
- Poloidal field coil current estimation,
- Axisymmetric Magnetohydrodynamic (MHD) stability analysis.

The various chapters in this thesis deal with these issues in detail. Chapter 2 describes the design and optimization of the resistive-magnet tokamak reactor. Chapter 3 presents a fast method for computing equilibria for shaped tokamaks. Chapter 4 describes a fast and robust procedure for the computation of the poloidal field (PF) and ohmic heating (OH) coil currents needed to support a specified plasma equilibrium. Chapter 5 presents an analysis which leads to general relations relating to the behavior of a plasma in the presence of a resistive wall. Finally, Chapter 6 describes a method for quickly and accurately computing the axisymmetric stability properties of a tokamak in the presence of a resistive wall, discrete resistive conductors, and feedback. More introductory remarks regarding each of these topics will be made later in this chapter. However, first, it is necessary to provide motivation as to why we study shaped tokamaks in the first place.

1.1 Effects of Plasma Shaping

The advent of the tokamak concept [1] in the USSR in the mid 1960's greatly enhanced the prospects for eventually developing magnetic fusion as a commercial source of electricity. However, early on, a major concern was that

the circular tokamak might not prove suitable for a power reactor. This is because the parameter β_t, defined as

$$\beta_t = \frac{\text{plasma pressure}}{\text{magnetic pressure}} \tag{1.1}$$

$$= \frac{2\mu_0 p}{B_0^2}, \tag{1.2}$$

is typically quite low ($< 1\,\%$) for conventional tokamaks. (In Eq. (1.2), p is the average plasma pressure and B_0 is the toroidal magnetic field measured at the plasma center.) Small beta values are undesirable because, in a simplistic sense, they imply low performance (p) obtained at high cost (B_0).

To see this point in slightly more specific terms, consider the simplified reactor power balance

$$P_E = \eta\, P_F, \tag{1.3}$$

where P_E is the desired electrical power, η is the thermal-electrical conversion efficiency, and P_F is the total fusion power which can be written

$$P_F = \frac{1}{4} n^2 \langle \sigma v \rangle\, V_p\, E_F. \tag{1.4}$$

In Eq. (1.4), n is the average plasma density, $\langle \sigma v \rangle$ is the Maxwellian reaction rate parameter, V_p is the volume of the plasma, and E_F is the energy produced by a single fusion reaction. Recognizing that $p = 2nT$ (where T is the average temperature), we can substitute Eqs. (1.2) and (1.4) into Eq. (1.3) to give the plasma volume necessary to obtain a given electric power

$$\beta_t^2 V_p = \frac{64\mu_0^2 P_E}{\eta B_0^4 E_F} \left(\frac{T^2}{\langle \sigma v \rangle} \right)_{min}. \tag{1.5}$$

The ratio $T^2/\langle\sigma v\rangle$ is simply a function of temperature. Hence, the plasma temperature can be chosen so as minimize that quantity. When this is done, Eq. (1.5) implies that, for a given P_E and B_0, small values of β_t result in correspondingly large values of V_p. Since, to some extent, the cost of a fusion reactor scales with the volume of the plasma, we conclude that low values of β_t are undesirable.

A similar conclusion applies to ignition experiments, but for a different set of reasons. In order to achieve ignition, it is necessary to satisfy a power balance between losses and production

$$P_L = P_\alpha, \tag{1.6}$$

where P_L is the power lost due to thermal conduction and P_α is the power carried by alpha particles that are produced in fusion reactions. A simple form for P_L can be written

$$P_L = \frac{3nT}{\tau_E}, \tag{1.7}$$

where τ_E is the energy confinement time. The alpha power is simply

$$P_\alpha = \frac{1}{4} n^2 \langle\sigma v\rangle V_p E_\alpha, \tag{1.8}$$

where E_α is the energy carried by a single alpha particle. Substituting Eqs. (1.7) and (1.8) and Eq. (1.2) into Eq. (1.6) gives

$$\beta_t \tau_E = \frac{48\mu_0}{B_0^2 E_\alpha} \left(\frac{T^2}{\langle\sigma v\rangle} \right)_{min}. \tag{1.9}$$

Here we see that low values of β_t increase the value of τ_E needed to achieve ignition. Given the current uncertainties regarding the magnitude, or even the form, of the energy confinement time, one again concludes that low β_t values are undesirable.

In tokamaks, β_t is limited by a combination of high-n ballooning modes and low-n pressure driven external kink modes [2]. The ballooning modes represent localized perturbations that are driven unstable by the pressure gradient in regions of unfavorable magnetic curvature. If this effect is averaged over the entire plasma (where there are alternating regions of favorable and unfavorable curvature), it can be shown that a limit on β_t alone results. In contrast, the high-β kink mode is driven unstable by both the pressure gradient and the current parallel to the magnetic field. Therefore, one finds that the pressure driven external kink modes yield a limit not only on β_t, but also on I_p (the total plasma current).

Since ballooning and kink modes depend on the curvature of the magnetic field, one might reason that the β limits could be increased by modifying the plasma shape from circular. As a result, a number of extensive numerical studies have been performed to find the tokamak configuration yielding the maximum stable value of β_t. One of the first studies, by Sykes, *et al.* [3], showed that finite aspect ratio plasmas possessing both elongation and outward pointing triangularity (as in Fig. 1.1) yielded higher maximum β_t values than the large aspect ratio circle. Furthermore, this maximum β_t value was shown to scale according to a remarkably simple formula

$$\beta_t = c'_\beta \frac{I_p}{aB_0}, \tag{1.10}$$

where $c'_\beta = 0.044$ is a constant of proportionality. Note that in Eq. (1.10) the units are $a\,(\mathrm{m})$, $I_p\,(\mathrm{MA})$, and $B_0\,(\mathrm{T})$.

Equation (1.10) can be recast into a more useful form by defining the "kink" safety factor

$$q_i = \frac{2\pi a^2 \kappa_a B_0}{\mu_0 R_0 I_p}. \tag{1.11}$$

Substituting Eq. (1.11) into Eq. (1.10) yields

$$\beta_t = c_\beta \frac{\epsilon \kappa_a}{q_i}, \tag{1.12}$$

where $c_\beta = 5c'_\beta = 0.22$ and $\epsilon = a/R_0$. Notice that Eq. (1.12) explicitly shows the favorable scaling with inverse aspect ratio and elongation. A similar study by Yamazaki, *et al.* [4] resulted in a slightly different scaling law that additionally gave the (favorable) dependence of β_t on triangularity.

Sykes's analysis considered only the effects of ballooning and Mercier modes. A later study by Troyon, *et al.* [5] considered ballooning modes, Mercier modes, $n = 1$ internal kink modes, and high-β kink modes. Again, it was found that finite aspect ratio, high triangularity, and high elongation were desirable from the point of view of stability. In addition, a scaling law of the form given in Eq. (1.10) resulted, but with a slightly smaller numerical value for the constant of proportionality $c'_\beta = 0.028$. However, by virtue of the fact that kink modes were included in the study, Troyon also found a limit on I_p. A similar analysis by Bernard, *et al.* [6] gave essentially the same scaling law except that the effect of triangularity was explicitly included. The Troyon scaling law along with the limit on total current have been verified experimentally [7] in the Doublet-III experiment at GA Technologies, Inc. though the data suggests that $c'_\beta = 0.033$.

Substituting various values for ϵ, κ_a, and q_i into Eq. (1.12) suggests that β_t values as high as 6–10 % are obtainable. This is supported by recent DIII-D experiments where stable β_t's of 6 % have been obtained [8]. A number of fusion systems studies [9–11] have shown that β_t's in this range are approaching that which is required to build a cost-effective tokamak reactor. Therefore, the importance, and indeed the necessity, of shaping is demonstrated.

1.2 Desirability of Approaches to Achieving High Beta

The simple arguments leading to Eqs. (1.5) and (1.9) imply that raising β_t is always desirable. This would probably be a true statement in general if it were not for the fact that the MHD scaling laws closely couple the maximum achievable β_t value with the specific configuration of the plasma. This coupling complicates matters greatly because the parameters that affect β_t — a, R_0, κ_a, and q_i — independently affect the performance of a tokamak to an extent at least as large as the β_t value itself does. We must therefore conclude that simple scaling arguments, such as those previously presented, have limitations to their validity. In particular, more detailed calculations are required to assess the effect of the MHD scaling laws on tokamak performance.

To examine this issue, we present in Chapter 2 a detailed design of a resistive-magnet tokamak reactor. The goal of the design is to minimize C, the cost/watt of electricity produced by the reactor. This minimization is, in turn, carried out subject to power balance and MHD stability requirements along with a number of additional straightforward physics and engineering constraints. Perhaps the most appealing feature of the calculation is that it is almost completely analytic in nature. Nevertheless, the results agree quite well with more sophisticated calculations [10].

The major result of the calculation is that raising β_t does not necessarily improve reactor performance. An illustration of this behavior is shown in Fig. 1.2. Here, C is plotted as a function of ϵ with $\kappa_a = 2.0$, $q_i = 1.5$, and $c_\beta = 0.165$. Initially, raising ϵ reduces C. However, after some point ($\epsilon = 0.37$), continued increases in ϵ actually result in increases in C. This result is unexpected given the monotonic variation in β_t with ϵ implied by Eq. (1.12). Similar behavior is seen Fig. 1.3 for the case of the elongation κ_a. Here, C initially decreases and then saturates with increasing κ_a. The

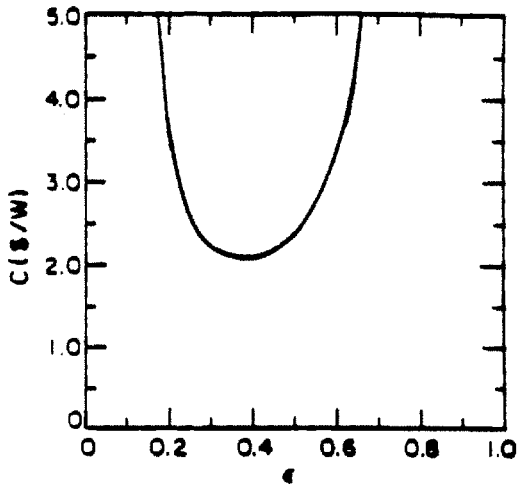

Figure 1.2: *Variation in C with ϵ for fixed values of κ_a, c_β, and q_i.*

overall conclusion is that shaping can be quite beneficial up to a point; after that, stronger shaping yields no significant gains in performance and may, in fact, result in a degradation of performance.

Another major result of the calculation is the extreme effect of a single physics constraint — the Murakami density limit — on reactor performance. By analyzing the data from a number of experiments around the world, Murakami, *et al.* [12] found evidence of a hard density limit after which disruptions would occur. This limit was found to scale as

$$n_0 < \frac{3c_M B_0}{2R_0}, \tag{1.13}$$

where n_0 is the central plasma density and $c_M \approx 0.8 \times 10^{20}\,\mathrm{m^{-2}} \cdot \mathrm{T^{-1}}$ for current experiments. Figure 1.4 shows the variation in C and T_0 (the central plasma temperature) with c_M. It is seen that substantial penalties are paid if the value of c_M cannot be increased (presumably through clever experimental techniques).

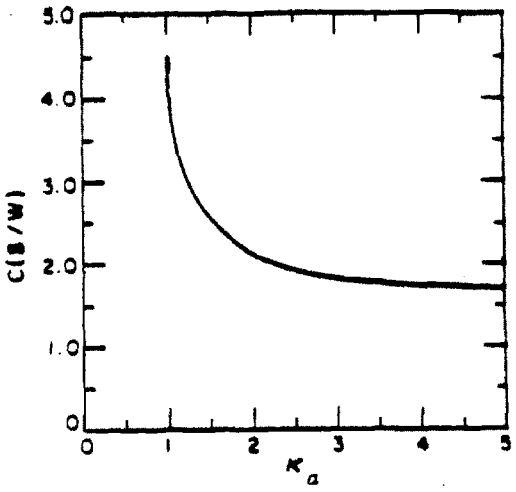

Figure 1.3: *Variation in C with κ_a for fixed values of c_β, and q_i.*

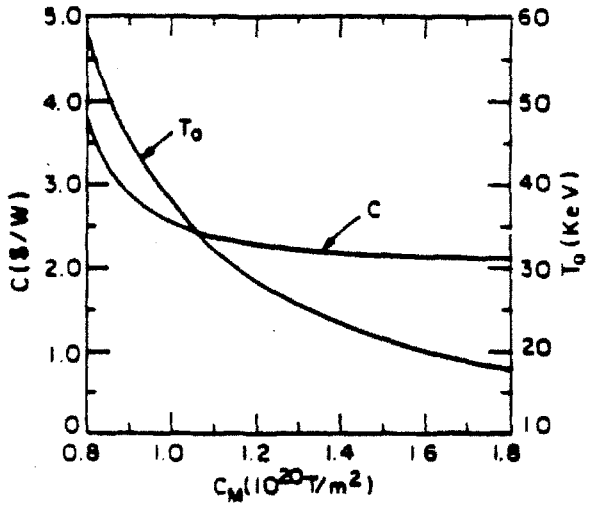

Figure 1.4: *Variation in C and T_0 with c_M.*

1.3 Variational Equilibrium

Having discussed some important design issues associated with shaped tokamaks, we turn to the next major topic of this thesis: the development of new tools for designing shaped tokamaks. The particular subject of Chapter 3 is the fast calculation of plasma equilibria.

The problem of plasma equilibrium consists of solving the Grad-Shafranov equation [13,14] in the presence of complicated geometry. Since the Grad-Shafranov equation is non-linear, this represents an extremely difficult computational chore so, despite the use of sophisticated numerical techniques, most present-day equilibrium codes require 0.5–5.0 minutes to execute on a Cray supercomputer. In this thesis, we propose a method that reduces this time to less than 1 sec on a Vax (which is typically 10–60 times slower than a Cray) at the cost of a small amount of accuracy.

The dramatic increase in speed is obtained through the use of variational techniques. A Lagrangian representing the Grad-Shafranov equation is derived and shown to represent a correct variational principle. Then, trial functions or "guesses" for the solution are substituted into this Lagrangian which, in turn, tells us which guesses are closest to the correct solution. Since good trial functions are readily derived, the procedure for searching for the optimal ones is extremely fast.

Despite the speed, the procedure is also quite accurate. Shown in Table 1.1 is a comparison between the parameters computed using the variational techniques and those computed using an exact equilibrium code. In the table, β_{max} is the value of β_t computed using the pressure at the magnetic axis $R = R_m$, β_p is the poloidal beta, $q(0)$ and q_s are the MHD safety factors at the magnetic axis and at the plasma surface respectively, ψ_0 is the flux evaluated at the magnetic axis, and κ_0 is the elongation of the innermost flux surface.

Table 1.1: *Comparison Between Variational and Exact Equilibria*

Parameter	Variational	Exact
$a\,(\mathrm{m})$	1.7	1.7
$R_0\,(\mathrm{m})$	4.7	4.7
κ_a	2.0	2.0
δ_a	0.4	0.4
β_t	0.082	0.083
β_{max}	0.224	0.222
β_p	0.805	0.830
$q(0)$	1.03	1.04
q_a	2.74	3.07
$\psi_0\,(\mathrm{Wb})$	-9.29	-9.19
$R_m\,(\mathrm{m})$	4.95	4.94
κ_0	1.69	1.79
Cray CPU Time (sec)	0.03	31.0

In addition to accurately computing the global plasma parameters in Table 1.1, the variational methods also yield good accuracy for such local quantities as the flux surface shape. This is shown in Fig. 1.5.

1.4 Estimation of PF Coil Currents

Chapter 4 describes a method for quickly estimating the coil currents necessary to support a specified plasma configuration in equilibrium. This method employs efficient numerical techniques based on an application of the scalar version of Green's theorem [15] to compute the tangential component of the vacuum magnetic field at the plasma surface in the form

$$\hat{B}_p(\mu) = b^{(1)}(\mu) + \sum_{j=1}^{J} b_j^{(2)}(\mu)\, I_j, \tag{1.14}$$

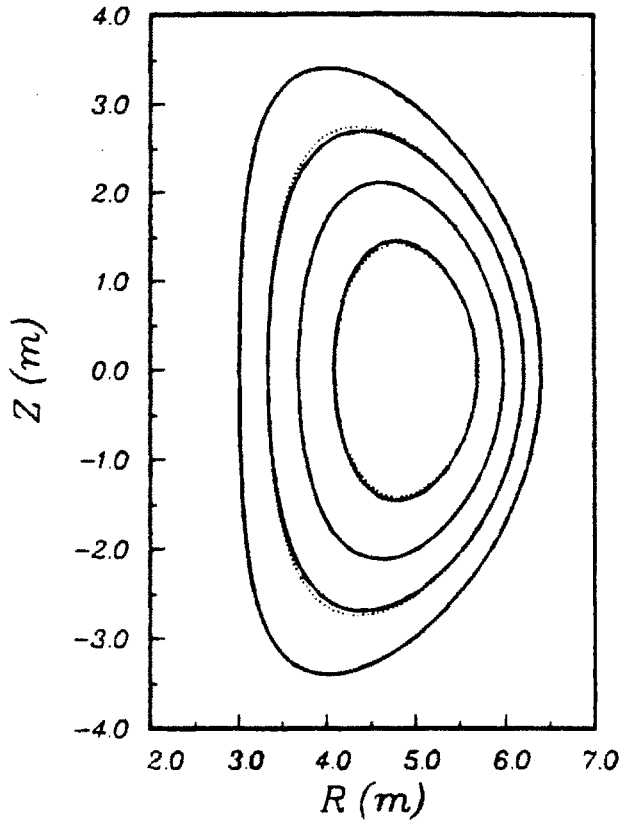

Figure 1.5: *Comparison between flux surface shapes computed exactly (solid lines) and those computed using variational techniques (dotted lines).*

where μ is a poloidal angular variable and I_j is the (as yet unknown) current in the j-th PF or OH coil. The currents are actually found by minimizing a functional of the form

$$\epsilon_I = \frac{\int_{S_p} (\hat{B}_p - B_p)^2 \, dS}{\int_{S_p} B_p^2 \, dS}, \tag{1.15}$$

where B_p is the poloidal field just inside the plasma surface. Equation (1.15) represents an attempt to ensure that the discontinuity in the tangential component of the magnetic field is as small as possible. The analysis explicitly ensures that the normal component of the field is exactly continuous across the plasma surface.

It can be shown that the set of currents that minimize ϵ_I satisfy a simple set of linear equations. Therefore, they can be found without the need for a potentially fragile and time-consuming iteration process. As a result, the procedure is extremely fast and robust, particularly when used in combination with the variational equilibrium methods from Chapter 3. For a typical plasma-coil configuration such as that shown in Fig. 1.6, the approximate solution of the Grad-Shafranov equation and the estimation of the required PF coil currents often takes less than 0.5 sec of Cray CPU time.

1.5 Stability in the Presence of a Resistive Wall

As Fig. 1.3 demonstrated, elongated shapes with $\kappa_a \approx 2$ yield dramatic increases in performance over circular shapes. However, elongated plasmas possess one major disadvantage: they tend to be unstable to vertical axisymmetric ($n = 0$) external MHD modes [16]. Clearly, this is unacceptable from the point of view of either reactor or experiment operation since the MHD instability timescale is on the order of microseconds. One way to prevent this is to place a perfectly conducting wall (the vacuum chamber) close to

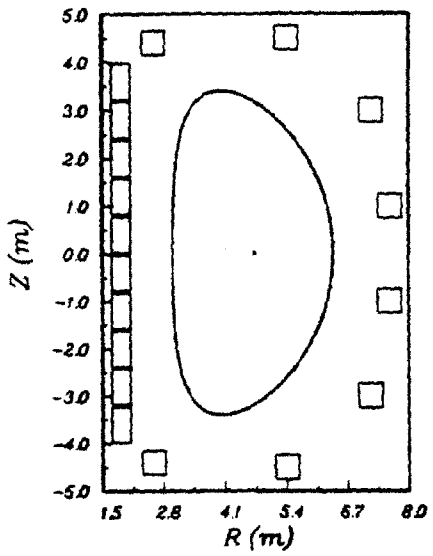

Figure 1.6: *Typical plasma and PF/OH coil configuration.*

the plasma. Numerous studies [17–21] have shown that this will completely stabilize $n = 0$ modes (along with $n \neq 0$ modes). However, in practice, vacuum chamber walls are not perfectly conducting. Instead, they tend to be made of materials, such as stainless steel, that have relatively high resistivities in order to allow for fast penetration of shaping and ohmic heating fields. This resistivity unfortunately also leads to a de-stabilization of the MHD modes. In particular, they begin to grow on a millisecond timescale which, while much slower than the MHD timescale, is still too fast to be acceptable in experiment or reactor designs. Therefore, understanding the effect of resistivity on external MHD modes is very important. Chapter 5 deals with exactly this issue.

Although the analysis in Chapter 5 is motivated by concerns about tokamak vertical stability, the calculations presented are valid for arbitrary three-dimensional perturbations acting on an arbitrary shaped plasma surrounded by an arbitrary shaped, but thin, resistive wall. As in Chapter 3, variational

techniques are employed in the calculations. In particular, a Lagrangian describing the plasma dynamics in the presence of a resistive wall is derived. This Lagrangian is then used to derive a very simple form for the growth rate γ of modes de-stabilized by the resistivity of the wall

$$\gamma\tau_D = -\frac{\delta W_\infty}{\delta W_b}, \tag{1.16}$$

where δW_∞ is the ideal MHD δW with a wall at infinity and δW_b is the ideal MHD δW with a perfectly conducting wall located at the position of the resistive wall. The resistive diffusion time τ_D is written

$$\tau_D = \mu_0 \sigma d \bar{b}, \tag{1.17}$$

where σ is the electrical conductivity of the wall, d is its thickness, and $\bar{b}$ is its average radius. Equation (1.16) is then used to investigate the effect of peaked current profiles and triangularity on tokamak vertical stability. Also, the effects of Finite Larmor Radius (FLR) and plasma rotation on stability are discussed.

1.6 Vertical Stability of Tokamaks in the Presence of Resistive Conductors and Feedback

Building on the physics background developed in Chapter 5, Chapter 6 describes the development of computer models for analyzing tokamak vertical stability. This turns out to be a very complicated problem because the effects of a resistive wall, discrete resistive coils, and feedback coupled with the non-uniform vertical displacement of the plasma must be considered. Despite this complication, efficient numerical methods are derived that require only a few seconds of Cray CPU time in order to analyze the linear exponential stability of the system. This represents an enormous saving over the time

required to compute the exact time-dependent evolution. Often, *hours* of Cray CPU time are required to solve that problem.

Again, variational methods are employed to speed up the calculation. Specifically, a Lagrangian which describes the motion of the plasma in the presence of J conducting wire loops is derived. The loops result from the finite differencing of all components in the poloidal field circuit: the resistive wall, the PF and OH coils, and any additional coils placed for purposes of enhancing stability. An example conductor configuration is shown in Fig. 1.7.

In addition to the Lagrangian, a series of J equations describing the inductive coupling between the plasma and the conductors is derived with the aid of a vector version of Green's theorem [22]. These relations are combined with the Lagrangian to yield a generalized matrix eigenvalue problem

$$\mathbf{R} \cdot \delta\mathbf{i} = \gamma \mathbf{M} \cdot \delta\mathbf{i}, \tag{1.18}$$

where γ (the eigenvalue) is the growth rate and $\delta\mathbf{i}$ (the eigenvector) is the set of currents induced by the plasma perturbation.

One of the most appealing aspects of this analysis is the fact that the plasma is relatively realistically modeled using the equations of ideal MHD. This allows the consideration of rather general plasma displacements of the form

$$\xi(R) = \xi_Z \left(\frac{R_m}{R}\right)^{\nu} \mathbf{e}_Z, \tag{1.19}$$

where ξ_Z is a constant and ν is a parameter controlling the non-uniformity in the displacement. The assumption of non-uniformity in ξ turns out to be quite important since, for finite aspect ratio dee-shaped plasmas, the growth rate found when $\nu \neq 0$ is significantly higher than that for the case of a uniform shift ($\nu = 0$). This point is illustrated in Fig. 1.8.

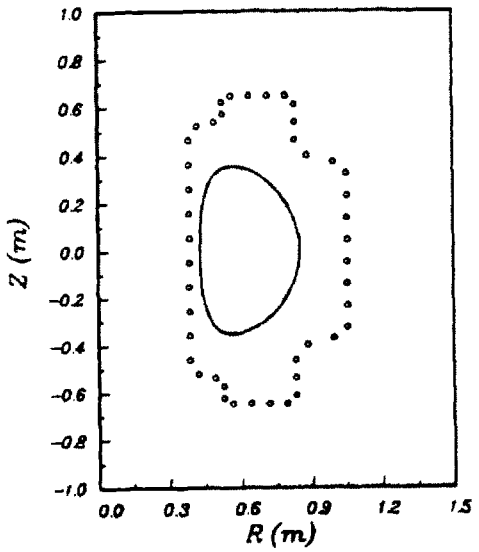

Figure 1.7: *Conductor configuration resulting from finite differencing the Alcator C-Mod vacuum chamber wall.*

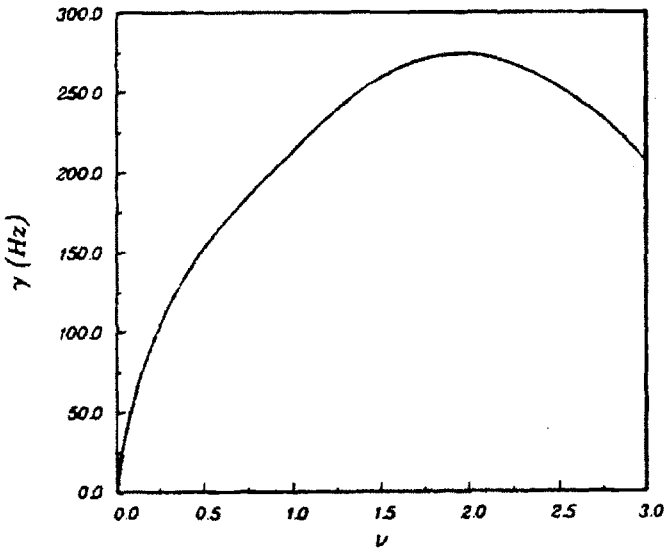

Figure 1.8: *Variation in γ with displacement non-uniformity parameter ν for dee-shaped plasma.*

Chapter 2

Desirability of Approaches to Achieving High Beta

Both simple scaling arguments of the type that led to Eqs. (1.5) and (1.9) and detailed fusion system studies [9–11] have indicated that tokamak reactor performance can be substantially improved if operation at high values of beta is possible. This realization has, in turn, provided motivation for the formulation of scaling laws predicting the maximum achievable beta in a tokamak [3–7]. These scaling laws provide a clear prescription for the means of achieving high beta and, ostensibly, improving reactor performance. In particular, they show [Eq. (1.12)] that beta scales favorably with increasing inverse aspect ratio ϵ, increasing vertical elongation κ_a, and decreasing safety factor q_i. However, one should note that each of the parameters which optimize beta may also have a comparably large (and sometimes adverse) impact on other aspects of reactor performance. This suggests that certain approaches to achieving high beta may be more desirable than others when considered in the context of a complete reactor design.

In this chapter, we address these issues by means of a simple analytical model of a long-pulse, resistive-magnet tokamak reactor. The design

is optimized to yield the minimum cost/watt of electricity subject to two constraints:

- Favorable plant power balance,
- First stability region beta scaling.

In addition, the design is required to satisfy a series of inequalities, derivable from straightforward physics and engineering considerations, which further limit the range of values that reactor parameters can assume. The model is deliberately idealized in order to transparently show how these constraints and inequalities affect the relative desirability of the various approaches to achieving high beta. Even so, the results of this model agree well with more sophisticated reactor systems code calculations [10].

2.1 Model

The design methodology to be discussed here is general in the sense that it can be applied to a wide variety of toroidal fusion systems including reactors and ignition experiments utilizing resistive or superconducting magnets. However, the results are necessarily device dependent. The present work centers on the design and optimization of an idealized fusion power plant producing a net electric power P_E. The plant is assumed to consist of a resistive-magnet tokamak reactor and its associated thermal conversion equipment.

Here, the bulk of the modeling effort focuses on the fusion island. In order to allow the possibility of an analytical optimization procedure, we consider an idealized configuration—consisting of a plasma region, an intermediate region, and a coil region—shown in Fig. 2.1. Even with the simplified nature of this description, the number of parameters needed to characterize the behavior of the fusion island is relatively large. Therefore, it is useful to list the relevant variables region by region and discuss, in some detail, the assumptions that go into their derivation.

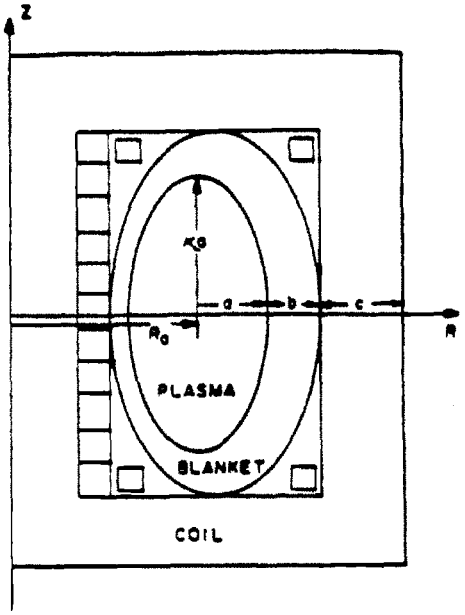

Figure 2.1: *Resistive-magnet tokamak reactor geometry.*

2.1.1 Plasma Region

As Fig. 2.1 shows, R_0 is the plasma major radius and a is the plasma minor radius. Since the existence of a scrape-off region is neglected, a also represents the distance from the plasma center to the first wall. For the sake of simplicity, in all geometrical calculations the plasma shape is taken to be elliptical with a vertical elongation κ_a. Also, the effect of toroidicity is ignored.

The plasma parameter of central importance to this analysis is the volume averaged toroidal beta which, to lowest order, is defined as

$$\beta_t \equiv \frac{4\mu_0}{B_0^2}\left(\frac{1}{V_p}\int_{V_p} nT\,dV\right), \tag{2.1}$$

where B_0 is the toroidal field at the plasma center and the integration is carried out over the plasma volume. Assuming parabolic temperature and density profiles, Eq. (2.1) gives

$$\beta_t = \frac{4\mu_0 n_0 T_0}{3B_0^2}, \tag{2.2}$$

where n_0 is the peak ion density and T_0 is the peak plasma temperature.

The fusion power output of the plasma P_F can be expressed as

$$P_F = \frac{E_F}{4} \int_{V_p} n^2 \langle \sigma v \rangle \, dV, \tag{2.3}$$

where E_F is taken to be 17.6 MeV and $\langle \sigma v \rangle$ is the Maxwellian D-T reaction rate parameter (approximated here using the results of Hively [23]). Using Eq. (2.2) to eliminate n_0 in favor of β_t yields

$$P_F = 2\pi^2 a^2 R_0 \kappa_a W(T_0) \beta_t^2 B_0^4. \tag{2.4}$$

Here,

$$W(T_0) \equiv \frac{9E_F}{64\mu_0^2 T_0^5} \int_0^{T_0} T^2 \langle \sigma v \rangle \, dT. \tag{2.5}$$

Of great technological importance is the neutron wall loading P_W which is related to the fusion power according to

$$P_W = \frac{P_F}{5\pi^2 R_0 a} \left[\frac{1 + \kappa_a^2}{2} \right]^{-1/2}, \tag{2.6}$$

indicating that 80 % of the energy from a given fusion reaction is assumed to appear in the form of 14.1 MeV neutrons.

The description of the plasma region is completed by specification of a scaling law for the energy confinement time τ_E. Several experimentally determined expressions for this quantity exist in the literature. For completeness, we will consider Neo-Alcator scaling [24]

$$\tau_{E,NA} = 0.095 \, n_0 \, a R_0^2, \tag{2.7}$$

Mirnov scaling [25]

$$\tau_{E,M} = 0.39 a I_p, \tag{2.8}$$

and Kaye-Goldston scaling [26]

$$\tau_{E,KG} = 0.055\,\kappa_a^{.28}\,B_0^{-.09}\,I_p^{1.24}\,n_0^{.26}\,P_\alpha^{-.58}\,a^{-.49}\,R_0^{1.65}, \tag{2.9}$$

where I_p is the plasma current and P_α is the alpha heating power given by

$$P_\alpha = \frac{P_F}{5}. \tag{2.10}$$

Note that in all practical formulae the units are $a\,(\mathrm{m})$, $R_0\,(\mathrm{m})$, $I_p\,(\mathrm{MA})$, $B_0\,(\mathrm{T})$, $P_{F,\alpha}\,(\mathrm{MW})$, $T_0\,(\mathrm{KeV})$, $n_0\,(10^{20}\,\mathrm{m}^{-3})$, and $\tau_E\,(\mathrm{sec})$.

2.1.2 Intermediate Region

The components between the plasma and the toroidal field (TF) coils—the first wall, the blanket, the ohmic heating (OH) coils, and the poloidal field (PF) coils—are assumed to make up the intermediate region.

The most important quantity describing the intermediate region is b: the thickness of the intermediate region at the horizontal and vertical midplanes of the device. On the outboard side b accounts for the space required for the blanket and the PF coils while on the inboard side b accounts for the space required for the OH coils and a thin inboard blanket. It is assumed that acceptable tritium breeding can be achieved despite the thinner inboard blanket.

The details of the blanket and thermal cycle design are largely ignored in this model. Instead, it is simply assumed that thermal power can be converted to electricity with an efficiency η. Also, credit is given for energy-producing neutron reactions in the blanket which multiply the thermal power output of the plant by a factor M.

Since the OH and PF coils are assumed to be placed inside the TF coils, they are necessarily resistive. Therefore, the power dissipated in these coils P_{PF} can be significant and must be taken into account. In general, P_{PF} depends in a complicated manner on the plasma shape, the plasma current, and the exact coil placement. These issues are outside of the scope of the present model so, for simplicity, it is assumed that the PF and OH dissipated power is some fraction of the power dissipated in the TF coils P_{TF}:

$$P_{PF} = f_{PF} P_{TF}. \tag{2.11}$$

2.1.3 Coil Region

The remainder of the nuclear island consists of TF coils and support structure. As Fig. 2.1 shows, the thickness of each of the four legs of the TF coils is represented by c. In addition, the inboard leg is assumed to fill the entire distance between the intermediate region and the device centerline. Hence,

$$c = R_0 - a - b. \tag{2.12}$$

Different thicknesses for each leg as well as the inclusion of a center-post have been investigated. These effects make small quantitative differences in the results, but greatly obscure the analysis. Hence, for purposes of simplicity, we focus attention on the model illustrated in Fig. 2.1.

Finally, the coils are assumed to wedge (remain contiguous) out to R_0. The choice of frame-shaped TF coils was motivated by a desire to be consistent with designs that incorporate demountable coils. Demountable coils may provide significant advantages in the areas of maintenance and machine availability [10].

The power required to drive the TF coils is of fundamental interest in resistive-magnet tokamak reactors. Neglecting the effects of start-up, this can be written as

$$P_{TF} = I_{TF}^2 \hat{R}, \tag{2.13}$$

where

$$I_{TF} = \frac{2\pi R_0 B_0}{\mu_0} \tag{2.14}$$

is the current in the TF coils,

$$\hat{R} = \frac{\rho}{\pi(R_0 - a - b)} G_{TF}(R_0, a, b, \kappa_a) \tag{2.15}$$

is the resistance of the TF coils, and Eq. (2.12) has been used to eliminate c. In addition, ρ is the coil resistivity and G_{TF} is a function that accounts for the specific geometry of the TF coils. Assuming a uniform current density and straight current paths that follow the midline of the coils, G_{TF} is found to be

$$G_{TF} = \frac{R_0 + (2\kappa_a - 1)a + b}{R_0 - a - b} + \ln \frac{2R_0}{R_0 - a - b} + \frac{R_0 + \kappa_a a + b}{R_0}. \tag{2.16}$$

The first term in Eq. (2.16) accounts for the geometry of the coil region on the inboard side of the plasma. The second term represents the portions of the top and bottom legs of the coils that wedge to R_0. The third term gives the contribution of the separated TF coils on the outboard side of the plasma.

2.1.4 Summary

In summary, our simplified model of a resistive-magnet tokamak reactor is described by the following parameters:

Performance Parameters

P_E	net electric power
P_F	fusion power
P_W	wall loading
P_{PF}	PF and OH dissipated power
P_{TF}	TF dissipated power

Plasma Parameters

β_t	plasma beta
q_i	plasma safety factor
n_0	peak density
T_0	peak temperature
B_0	toroidal field at plasma center
I_p	toroidal plasma current
τ_E	energy confinement time

Geometric Parameters

a	plasma minor radius
R_0	plasma major radius
b	intermediate region thickness
c	coil thickness
κ_a	plasma elongation

2.2 Formulation

The formal optimization procedure used in the analysis is summarized as follows. The first step is the selection and definition of a figure of merit. This figure of merit, which is written in terms of a number of independent variables, serves as the basic measure of the attractiveness of a particular design. Next, constraints which give relationships between the independent variables are imposed on the design. Each of these constraints allows one independent variable to be eliminated from the calculation. Finally, a series of inequalities that specify a range of allowable values for some of the remaining independent variables is provided. A particular choice of the figure of merit and associated constraints and inequalities is not unique; however,

once a choice is made, a unique optimized design can be found. In principle, the design is optimized by varying the independent variables in order to find the most favorable value of the figure of merit. When this variation would require violation of an inequality, that inequality becomes an equality (i.e. a constraint) and the optimization is repeated. One of the primary advantages of the simple model presented in the previous section is that the number of degrees of freedom is sufficiently limited to allow the optimization to be performed essentially analytically. Having discussed the design methodology in formal terms, we now consider the details of the calculation.

2.2.1 Figure of Merit

For the purposes of the analysis, we select C, the direct capital cost of the plant per watt (electric), as the figure of merit which is obviously to be minimized. C includes contributions from both the fusion island and the balance of plant. This feature makes it more desirable as a figure of merit than, for instance, the fusion island weight which focuses only on one part of the plant. In addition, it is widely thought that fusion reactors will be expensive and complicated devices. Since it is possible that the suitability of fusion energy as a power source will depend on its economic attractiveness as compared to alternative concepts, it seems a judicious choice to use a figure of merit based on costs. Other studies have investigated the impact of the choice of figure of merit on the optimized design [27].

In general, C is a complicated function of several variables. Keeping the philosophy of the analysis in mind, we present a simple model which analytically displays the relevant dependencies. We write C (\$/watt) as the sum of a balance of plant contribution C_{BP} (\$) and a fusion island contribution C_{FI} (\$):

$$C = \frac{C_{BP} + C_{FI}}{P_E}. \tag{2.17}$$

C_{BP} includes contributions for such things as land and reactor buildings but is assumed here to be dominated by costs for thermal energy conversion facilities, specifically turbines and electrical switching equipment. Given this, one expects C_{BP} to scale with the thermal fusion power. We make the simplest choice for this dependence, namely

$$C_{BP} = K_{BP} P_F, \tag{2.18}$$

where K_{BP} is a proportionality constant.

With regard to the fusion island, we make the straightforward assumption that the capital cost is proportional to its volume V_{FI}. Hence, C_{FI} can be written

$$C_{FI} = K_{FI} V_{FI}, \tag{2.19}$$

where K_{FI} represents the average unit cost of the entire fusion island and, from Fig. 2.1,

$$V_{FI} = 8\pi R_0^2 [R_0 + (\kappa_a - 1)a]. \tag{2.20}$$

Combining results gives the following expression for the figure of merit

$$C = K_{BP} \left(\frac{P_F}{P_E} \right) + K_{FI} \left(\frac{V_{FI}}{P_E} \right). \tag{2.21}$$

This costing model is similar to that proposed by Spears and Wesson [28]

It could be argued that including the plasma region in Eq. (2.21) is unreasonable since it is mainly 'empty'. We justify its inclusion by the fact that the plasma region determines the requirements for the potentially expensive auxiliary heating, fueling, and burn-control systems.

It is beyond the scope of the model to actually calculate the two quantities K_{BP} and K_{FI}. Instead, the values of C_{FI} and C_{BP} were extracted from systems code runs [29] for particular P_E, P_F, and V_{FI}. Given these, Eqs. (2.18) and (2.19) predict that numerically,

$$K_{BP} = 0.55\,\$/\mathrm{W},$$

$$K_{FI} = 0.20\,\mathrm{M\$/m^3}.$$

For the purposes of simplicity, we make the assumption that K_{BP} and K_{FI} are constants. In reality, these quantities might be expected to be functions of, for instance, P_E, P_W, and V_{FI}. However, it will be shown later that the design optimization process is actually not very sensitive to the exact values of the unit cost coefficients.

2.2.2 Constraints

We now describe the constraints imposed on the design. These constraints are necessary because the formulation so far does not fully distinguish between different classes of tokamak devices and operation in different regimes of MHD stability physics. For instance, the model presented in the previous section is equally valid for commercial reactors, ignition devices, or experiments. In addition, the model makes no explicit assumptions regarding the details of the β limit characterizing the device.

In order to place the model in the regime of the commercial tokamak reactor, we impose the requirement for a favorable plant power balance

$$P_E = \eta M P_F - P_R, \tag{2.22}$$

where P_R is the total recirculating power which is assumed to be due entirely to the dissipation in the TF, PF, and OH coils

$$P_R = P_{TF} + P_{PF}. \tag{2.23}$$

Equation (2.22) is written by assuming near steady-state operation (i.e. high duty factor) and neglecting radiation losses. It can be stated in the convenient form

$$P_E = \eta M P_F (1 - f_R) \tag{2.24}$$

using the recirculating power fraction f_R defined as

$$f_R = \frac{P_R}{\eta M P_F}. \tag{2.25}$$

We further constrain the design by requiring that the device operate in the first region of MHD ballooning-kink stability. It should be noted that a second region of ballooning stability characterized by very large β values has been theoretically predicted [30,31]. See Ref. [10] for a discussion of the effects of this regime on resistive-magnet tokamak reactor performance.

In the first stable regime, the maximum allowable β_t obeys a scaling law of the form given in Eq. (1.10)

$$\beta_{t,max} \propto \frac{I_p}{aB_0}. \tag{2.26}$$

Note that in this context we are assuming that the plasma possesses some triangularity. Equation (2.26), restated in a more convenient form, thus becomes the second constraint

$$\beta_t = c_\beta \frac{a\kappa_a}{R_0 q_i}, \tag{2.27}$$

where c_β is a constant and q_i is the kink safety factor

$$q_i = \frac{2\pi a^2 \kappa_a B_0}{\mu_0 R_0 I_p}. \tag{2.28}$$

2.2.3 Inequalities

Having specified the model along with the engineering and physics regimes of interest, we next consider the physical domain over which the design optimization can be performed. Many of parameters of interest are limited to a range of allowable values by straightforward engineering and physics requirements. These requirements lead to a series of inequalities which must be satisfied by the design.

Inequalities for Plasma Region Parameters

The performance of the plasma is largely limited by stability considerations. In particular, one of the most important inequalities is due to MHD kink/disruption limits which set a lower bound on the value of the safety factor or, conversely, an upper bound on the plasma current. This limit is usually written in terms of the MHD safety factor

$$q_s > 2.0. \tag{2.29}$$

Here, q_s is defined:

$$q_s = \frac{1}{2\pi}\int_0^{2\pi} [\frac{rB_t}{RB_p}]_s \, d\theta, \tag{2.30}$$

where the subscript 's' indicates that the integration is carried out over a particular flux surface.

Stating the kink/disruption limit in terms of q_s turns out to be a misleading choice from the point of view of the reactor designer. This is because the actual β limit depends on q_i rather than q_s and, except in the case of circular low β plasmas, these two quantities do not have the same value. Furthermore, q_s is strongly dependent on the proximity of separatrices and shaping of the inner plasma edge. In fact, it is possible to satisfy the limit given in Eq. (2.29) for arbitrarily large currents by placing a separatrix sufficiently close to the plasma. This contradicts recent experimental results which suggest a hard disruptive limit to the plasma current [7]. For these reasons, it may be more accurate and appropriate to state the kink/disruption limit in terms of q_i. However, the form of this limit is currently unknown and one might expect the limiting q_i to be dependent upon the plasma shape (elongation, indentation, triangularity, aspect ratio, etc) and, perhaps, β_t itself. For the purposes of this analysis, we make the simplifying assumption that

$$q_i > 1.5, \tag{2.31}$$

the limiting value being chosen to approximately correspond to $q_* = 2.0$ given the parameters in Troyon's paper.

Various values for the constant of proportionality in the beta limit have been discussed previously in this thesis. We choose the maximum value of c_β to be that found experimentally by Stambaugh, *et al.* [7]. Consistent with the Sykes q-prescription, this inequality is thus written

$$c_\beta < 0.165. \tag{2.32}$$

MHD stability considerations also provide an upper limit on the plasma elongation. This limit results from analyses that suggest that elongated plasmas are particularly susceptible to axisymmetric ($n = 0$) modes [32]. It is assumed that these modes can be feedback stabilized for plasmas with

$$\kappa_a < 2.0. \tag{2.33}$$

Murakami *et al.* [12] have suggested that, in order to prevent disruptions, the central plasma density must be kept below some critical value. This leads to an inequality of the form

$$n_0 < \frac{3c_M B_0}{2R_0}, \tag{2.34}$$

where c_M is a parameter that may depend on κ_a and q_i. For simplicity, we will assume that c_M is a constant. Typically, $c_M \approx 0.8 \times 10^{20}\,\mathrm{m^{-2}} \cdot \mathrm{T}^{-1}$ for current experiments. Given operation at some β_t, Eq. (2.34) implies an inequality for the temperature

$$T_0 > \frac{\beta_t B_0 R_0}{2\mu_0 c_M}. \tag{2.35}$$

Due to uncertainties with regard to the behavior of first wall materials on exposure to large neutron fluxes, an upper limit is set on the neutron wall loading

$$P_W < 5.0\,\mathrm{MW/m^2}. \tag{2.36}$$

Finally, on the basis of the assumption of ignited operation, the confinement time is required to satisfy a Lawson condition [33]

$$n_0 \tau_E > 6.0 \times 10^{20}\,\mathrm{m^{-3}} \cdot \mathrm{sec}. \tag{2.37}$$

Inequalities for Intermediate Region Parameters

In contrast with the plasma region, engineering considerations largely account for the inequalities associated with the blanket and thermal cycle. These inequalities depend sensitively on the blanket/first wall concept utilized. For purposes of illustration, we assume a vanadium first wall and a liquid lithium blanket. In the blanket, liquid lithium acts as both a coolant and a tritium breeder. Given this choice, we can state the following inequalities which are based on the results of detailed blanket design studies [34]:

$$\eta < 42\,\%, \tag{2.38}$$

$$M < 1.20, \tag{2.39}$$

$$b > 1.0\,\mathrm{m}. \tag{2.40}$$

The maximum value of η is a strong function of the blanket/first wall concept and results from considerations of power plant thermodynamics. The limit on M is consistent with the assumption of no fissionable materials in the blanket. Finally, the minimum value of b is primarily determined on the basis of shielding and tritium breeding requirements. Because the shielding requirements for normal coils are much less stringent than for superconducting coils, the intermediate region thickness characteristic of resistive-magnet tokamaks is significantly smaller than for superconducting tokamaks.

Since the present model does not include detailed plasma equilibrium calculations, the power dissipated in the OH and PF coil systems must be

estimated using results from more detailed analyses [10]. An inequality that gives rough agreement is

$$f_{PF} > 33\,\%. \tag{2.41}$$

To keep the design in the regime of typical commercial power plants it is finally required that the net electric power output not get unacceptably high

$$P_E < 1200\,\mathrm{MW}. \tag{2.42}$$

Inequalities for Coil Region Parameters

The value of ρ in a resistive tokamak is primarily set by the operating temperature of the TF coils and the fraction of the coil cross-sectional area that is available to carry current (the rest being required for cooling and structure). Here, operation at room temperature with coils that consist of 90 % copper (by area) is assumed. With this,

$$\rho > 1.88 \times 10^{-8}\,\Omega \cdot \mathrm{m}. \tag{2.43}$$

2.2.4 Problem Statement

Given the previous discussion, it is now possible to formulate the design optimization procedure in mathematical terms. But first, it is convenient to make the change of variables

$$\epsilon = a/R_0, \tag{2.44}$$

$$\epsilon_b = b/R_0, \tag{2.45}$$

where ϵ can be recognized as the plasma inverse aspect ratio and ϵ_b can be thought of as a dimensionless thickness for the intermediate region. In terms of the analysis, ϵ replaces a and ϵ_b replaces R_0 as independent variables. This set of variables is motivated by the fact that the beta limit depends directly on ϵ as opposed to a and R_0 separately. Other choices of variables lead to a much more complicated analysis.

Using the new variables along with Eqs. (2.20) and (2.24), the figure of merit given in Eq. (2.21) becomes

$$C = K_{BP}\left(\frac{1}{\eta M(1-f_R)}\right) + K_{FI}\left(\frac{8\pi b^3[1+(\kappa_a-1)\epsilon]}{P_E\epsilon_b^3}\right). \tag{2.46}$$

It is possible to eliminate the β scaling constraint immediately by substituting β_t from Eq. (2.27) into Eq. (2.4). This gives the following expression for the fusion power:

$$P_F = \frac{2\pi^2 W(T_0) c_\beta^2 b^3 B_0^4 \epsilon^4 \kappa_a^3}{q_i^2 \epsilon_b^3}. \tag{2.47}$$

P_R can be also be written in terms of the new variables

$$P_R = \frac{4\pi\rho b B_0^2(1+f_{PF})}{\mu_0^2\epsilon_b(1-\epsilon-\epsilon_b)} G_{TF}(\epsilon,\epsilon_b,\kappa_a), \tag{2.48}$$

where G_{TF} now becomes

$$G_{TF} = \frac{1+(2\kappa_a-1)\epsilon+\epsilon_b}{1-\epsilon-\epsilon_b} + \ln\left(\frac{2}{1-\epsilon-\epsilon_b}\right) + \kappa_a\epsilon + \epsilon_b + 1. \tag{2.49}$$

Eliminating B_0 from Eq. (2.47) using Eqs. (2.25) and (2.48) allows us to express the plant power balance constraint given by Eq. (2.24) as a function of the independent variables

$$G(\epsilon, \epsilon_b, \kappa_a) = \frac{E(q_i, c_\beta, \eta, M, f_{PF}, P_E, b, \rho, f_R)}{W(T_0)}. \tag{2.50}$$

Here,

$$G \equiv \frac{\epsilon^4(1-\epsilon-\epsilon_b)^2\kappa_a^3}{\epsilon_b G_{TF}^2} \tag{2.51}$$

describes the geometrical aspects of the constraint and

$$E \equiv \frac{8}{\mu_0^4}\left(\frac{q_i^2}{c_\beta^2}\right)\left(\frac{\rho^2(1+f_{PF})^2}{\eta M P_E b}\right)\left[\frac{1-f_R}{f_R^2}\right] \tag{2.52}$$

describes the physics and engineering aspects of the constraint. The T_0 dependence is separated out due to subtleties associated with the application of the Murakami density limit.

At this point, the mathematical basis for the design optimization is completed. Equation (2.46) is to be minimized subject to the constraint given in Eq. (2.50). This minimization is performed over the independent variables

$$\epsilon,\ \epsilon_b,\ \kappa_a,\ q_i,\ c_\beta,\ \eta,\ M,\ f_{PF},\ P_E,\ b,\ \rho,\ f_R,\ T_0$$

with the quantities

$$K_{BP},\ K_{FI}$$

held fixed.

We show that C varies monotonically with respect to several of the independent variables. In such cases, the minimization can be simply accomplished by invoking the inequalities discussed in the previous section. Thus, despite the relatively large number of variables and the complexity of the governing equations, the optimization can be performed essentially analytically. However, of interest as well is the sensitivity of the cost/watt to variations in

limiting values prescribed by the inequalities. Deriving this behavior requires straightforward numerical calculations.

Once the independent variables are calculated they may be used to determine the values of other important derived quantities given by

$$C,\ \beta_t,\ n_0,\ P_F,\ P_R,\ P_W,\ \tau_E,\ a,\ R_0,\ c,\ B_0,\ I_p.$$

In the context of our model, specification of the independent and derived quantities fully describes the design.

2.3 Optimization I

One of the most important parameters affecting reactor performance turns out to be the Murakami parameter c_M. Due to subtleties associated with the application of the Murakami limit, it is convenient to consider two separate optimization procedures (leading to two different reactor designs). In the first case (Optimization I), C will be minimized independent of the Murakami limit and c_M will be calculated so as to satisfy Eq. (2.35). In the second case (Optimization II), C will be minimized with c_M held fixed at a value consistent with results from current experiments. We will see that the current Murakami limit provides very stringent limits on resistive-magnet tokamak reactor performance.

In Table 2.1, designs resulting from the assumptions of both optimization procedures are displayed. These designs are quite dependent on the inequalities and constraints derived previously: application of a different set of assumptions could lead to a different and, perhaps, more desirable design. In the discussion to follow, we outline the analysis consistent with the assumptions of Optimization I and examine the sensitivity of the results to variations in the inequalities.

Table 2.1: *Base Design Parameters*

Parameter	Optimization I	Optimization II
ϵ	0.37	0.40
$a\,(\mathrm{m})$	1.7	2.9
$b\,(\mathrm{m})$	1.0	1.0
$c\,(\mathrm{m})$	2.0	3.3
$R_0\,(\mathrm{m})$	4.7	7.1
κ_a	2.0	2.0
q_i	1.5	1.5
c_β	0.165	0.165
η	0.42	0.42
M	1.2	1.2
$f_{PF}\,(\%)$	0.33	0.33
$P_E\,(\mathrm{MW})$	1200	1200
$\rho\,(10^{-8}\,\Omega\cdot\mathrm{m})$	1.9	1.9
$f_R\,(\%)$	0.25	0.25
$n_0\,(10^{20}\,\mathrm{m}^{-3})$	3.5	0.88
$T_0\,(\mathrm{KeV}))$	17.5	57.6
$c_M\,(10^{20}\,\mathrm{m}^{-2}\cdot\mathrm{T}^{-1})$	1.8	0.8
$\beta_t\,(\%)$	8.1	8.8
$P_{TF}\,(\mathrm{MW})$	300	300
$P_W\,(\mathrm{MW/m^2})$	5.0	2.0
$\tau_{E,NA}\,(\mathrm{sec})$	12	12
$\tau_{E,M}\,(\mathrm{sec})$	13	34
$\tau_{E,KG}\,(\mathrm{sec})$	0.73	1.4
$B_0\,(\mathrm{T})$	4.5	3.9
$I_p\,(\mathrm{MA})$	19	30
$W(T_0)\,((\$/\mathrm{W}))$	2.0	3.7

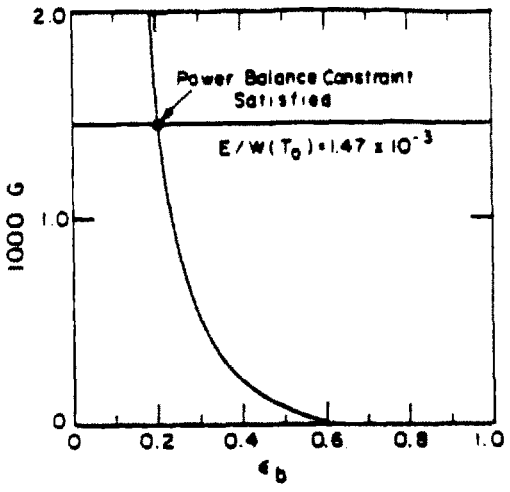

Figure 2.2: *Graphical representation of power balance constraint.*

2.3.1 Application of Power Balance Constraint

The power balance constraint [Eq. (2.50)] allows one of the variables to be calculated in terms of those remaining. For this analysis, we choose to solve for ϵ_b. We see that Eq. (2.50) is a complicated transcendental equation which, in general, must be solved numerically. However, it is possible to gain qualitative insight about the behavior of ϵ_b which will allow many of the optimizations to be performed analytically.

Critical to the analysis is the observation that G [Eq. (2.51)] is a monotonically decreasing function of ϵ_b if ϵ and κ_a are assumed fixed. This behavior is shown in Fig. 2.2. On this plot, the power balance constraint is satisfied at the points of intersection between the decreasing function $G(\epsilon_b)$ and the horizontal line $G = E/W(T_0)$. These intersections give the value of ϵ_b for a particular choice of the other parameters.

Two important facts can be inferred from Fig. 2.2. First, ϵ_b is maximized by reducing the value of $E/W(T_0)$. Second, the resulting value of ϵ_b varies

less than linearly with $E/W(T_0)$. These observations, which hold for all values of ϵ and κ_a, will be used extensively in the optimizations to follow.

2.3.2 Optimization with respect to Inverse Aspect Ratio

For many of the independent variables, C is shown to vary monotonically. Hence, it is possible to perform design optimizations by invoking the appropriate engineering and physics inequalities. In the case of ϵ, however, C exhibits a minimum. By a straightforward calculation of the partial derivative of C with respect to ϵ, it is possible to derive an approximate expression for the value of the "optimum" inverse aspect ratio ϵ_{opt}. First, we notice that most of the ohmic power dissipated in the TF coils is due to the inner TF leg. Hence, with little error, it is possible to neglect the contributions of the top and outside TF legs. This yields the simplified expression for G_{TF}

$$G_{TF} \approx \frac{1 + (2\kappa_a - 1)\epsilon + \epsilon_b}{1 - \epsilon - \epsilon_b}. \tag{2.53}$$

Plugging Eq. (2.53) into the plant power balance constraint and solving for ϵ_b gives

$$\epsilon_b = 1 - \epsilon - \frac{1}{\epsilon}\left[\frac{E}{W(T_0)\kappa_a^3}\{(1 + (2\kappa_a - 1)\epsilon + \epsilon_b)^2\epsilon_b\}\right]^{1/4}. \tag{2.54}$$

We now neglect the variation of the quantity $(1 + (2\kappa_a - 1)\epsilon + \epsilon_b)^2\epsilon_b$ since it does not contribute in any fundamental way to the existence of the minimum in C. This turns out to be a good approximation for a fairly wide range of elongations and aspect ratios if we take $(1 + (2\kappa_a - 1)\epsilon + \epsilon_b)^2\epsilon_b \approx 1$. With this,

$$\epsilon_b \approx 1 - \epsilon - \frac{1}{\epsilon}\left[\frac{E}{W(T_0)\kappa_a^3}\right]^{1/4}. \tag{2.55}$$

Finally, we note from Eq. (2.46) that, except at large elongations, the minimum in C with respect to ϵ largely corresponds to the maximum in ϵ_b. Thus, setting the derivative of Eq. (2.55) with respect to ϵ to zero yields the desired result

$$\epsilon_{opt} \approx \left[\frac{E}{W(T_0)\kappa_a^3}\right]^{1/8}. \tag{2.56}$$

The existence of ϵ_{opt} is explained by Eq. (2.51) which suggests that as ϵ approaches either zero or one, ϵ_b must decrease accordingly in order for the power balance constraint to be satisfied. Decreasing ϵ_b is equivalent to increasing R_0 so the volume of the fusion island and C increase correspondingly. Physically, in the limit of small ϵ, both a and the allowed β_t decrease. Thus, a larger major radius is required to maintain a constant fusion power. In the limit of large ϵ, a smaller relative fraction of the space on the inboard side of the device is available for the TF coil. Hence, a larger major radius is required to keep the recirculating power constant. Figure 2.3 is a plot of C vs. ϵ with ϵ_b varying so as to satisfy Eq. (2.50) and all other variables taking on the values shown in Table 2.1. This curve shows that the minimum in cost/watt is quite strong.

The existence of an optimal aspect ratio is not a unique feature of resistive tokamak reactors. Freidberg and Wesson [35] have demonstrated that in a superconducting tokamak reactor the cost is minimized for $\epsilon_{opt} = 1/6$. This result is a consequence of a constraint on superconducting magnets that requires that the field at the coil be less than some critical field (usually 10–12 T).

On the basis of the β limit alone, one might conclude that it is desirable to make the aspect ratio as tight as technologically possible [36]. However, the introduction of the power balance constraint leads to an optimum ϵ which, for the parameters assumed here, generally lies in the range $\epsilon_{opt} \approx 0.3$–$0.5$.

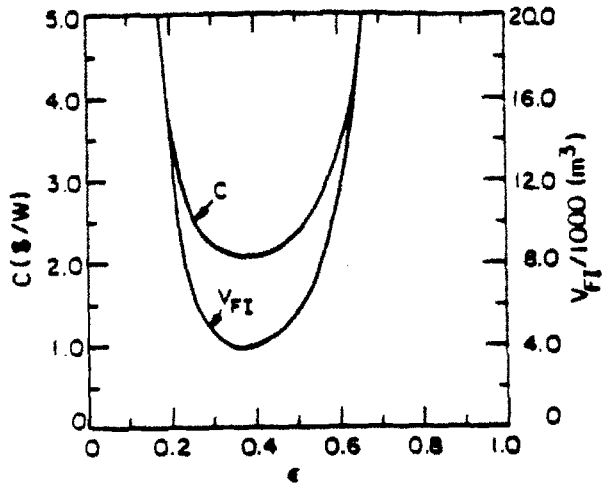

Figure 2.3: *Dependence of C and V_{FI} on ϵ for $c_M = 1.8 \times 10^{20}\,\mathrm{m}^{-2} \cdot \mathrm{T}^{-1}$ with ϵ_b chosen to satisfy the power balance constraint and all other parameters fixed at their base design values.*

Furthermore, Eq. (2.56) shows that this value is a slowly varying function of the other parameters so it would not be expected to change greatly upon application of different assumptions. Alternatively, optimizations on other reactor parameters can yield a significant reduction in the cost/watt without the need for tight aspect ratio. Since operation at ϵ_{opt} appears to be desirable from the point of view of minimizing the cost, this model suggests that ultra-tight aspect ratio might not be necessary for improving resistive tokamak reactor performance.

2.3.3 Optimization with respect to Parameters Appearing Only in the Physics/Engineering Constraint

From Eq. (2.46) we see that the variables q_i, c_β, ρ, and f_{PF} do not appear explicitly in the expression for C. Instead, they enter the calculation only

indirectly through ϵ_b. Since C is a monotonically decreasing function of ϵ_b, the cost/watt can be be minimized with respect to these variables by maximizing ϵ_b. From the discussion above, this is accomplished by minimizing E. In particular, Eq. (2.52) implies that q_i, ρ, and f_{PF} must be minimized and c_β maximized. Since E varies monotonically with respect to these quantities, the inequalities given in Eqs. (2.31), (2.32), (2.41), and (2.43) must be invoked. This leads to values $q_i = 1.5$, $\rho = 1.88\,\Omega \cdot \mathrm{m}$, $f_{PF} = 33\,\%$, and $c_\beta = 0.165$ used in the base design.

A large value of the ratio c_β/q_i is desirable because of the resulting favorable effects on the maximum allowed β_t. In particular, the sensitivity of C to c_β/q_i is given in Fig. 2.4. In this plot, C is seen to decrease monotonically with c_β/q_i with all other variables except for ϵ and ϵ_b fixed at the values given in Table 2.1. ϵ_b is calculated numerically using Eq. (2.50) for $\epsilon = \epsilon_{opt}$ at each value of c_β/q_i. Thus, each point on the curve represents an optimized design for a given c_β/q_i. Note, however, that not all of these designs are acceptable since they would lead to violation of the wall loading inequality [Eq. (2.36)].

Figure 2.4 shows that C is a moderately strong function of q_i and c_β. Even so, we see that there appears to be little improvement in reactor performance to be gained by relaxing the limits on these physics parameters somehow (possibly through the judicious use of plasma shaping and profile control). On the other hand, if the base design values cannot be realized, a substantial cost penalty must be paid. This point is particularly important given the current ambiguity associated with the statement of the MHD kink limit. One should note that q_i and c_β only appear in the calculation as a consequence of the introduction of the first-stability β limit. Hence, in this case, increasing β_t actually does result in the total cost being lowered although the effect becomes less pronounced once some minimum level of performance (more or less specified by the base design values) is obtained.

Small values of ρ are clearly desirable since they reduce the coil volume needed to achieve a given f_R. One might thus be tempted to speculate

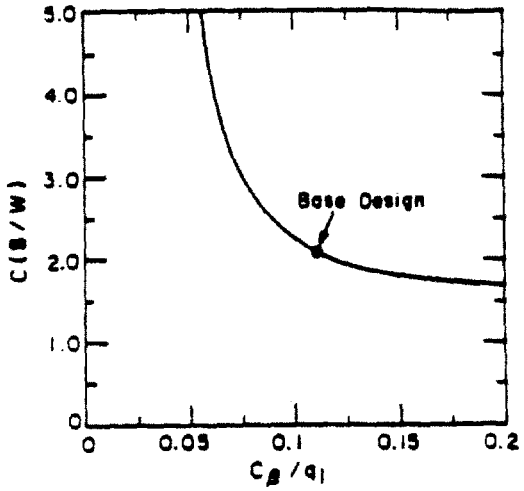

Figure 2.4: *Sensitivity of C to variations in c_β/q_i for $c_M = 1.8 \times 10^{20}\,\mathrm{m}^{-2} \cdot \mathrm{T}^{-1}$ and all other parameters fixed at their base design values.*

that resistive-magnet tokamak reactors with TF coils operating at cryogenic temperatures would realize a large increase in performance in view of the resulting large reductions in coil resistivity. The present formulation of the model is unable to adequately address this question because of the additional requirement to include the (adverse) effects of cryogenic cooling systems on the cost and the power balance relations. However, more detailed studies show this cost to be prohibitive [10]. Note also that the model presented here cannot be applied to reactors with superconducting coils since an entirely different set of inequalities and constraints would be required.

Decreasing f_{PF} allows a larger value of P_{TF} for a given value of f_R thus reducing the coil volume and C. This effect, although favorable, is relatively small for reasonable variations in f_{PF}.

2.3.4 Optimization with respect to Net Electric Power

E decreases with increasing P_E so, consequently, ϵ_b is an increasing function of P_E. In addition, Eq. (2.46) shows that the cost/watt of the balance of plant is independent of P_E. As a result, we recover the usual result that the cost/watt is minimized by setting P_E to its maximum allowable value which, from Eq. (2.42), is 1200 MW. The fact that ϵ_b increases with P_E is somewhat surprising in that this implies that the fusion island volume actually decreases with increasing P_E. This occurs because f_R is held constant as P_E is varied. Hence, small values of P_E necessarily require small values of P_R. To attain small recirculating powers requires a large coil volume. Since the volume of the nuclear island is dominated by the volume of the coils, the fusion island volume increases accordingly. The variation of C with P_E is shown in Fig. 2.5. In general, a fairly large penalty must be paid if operation at low power outputs is desired. At the same time, C is not significantly reduced by increasing P_E over the base design value.

2.3.5 Optimization with respect to Intermediate Region Thickness

From Eq. (2.52), E is seen to be a function of $1/b$. This, in turn, implies that ϵ_b is a decreasing function of b. As previously stated, $\epsilon_b(E)$ increases at a rate less than linear. Hence, the ratio b/ϵ_b, which appears in the fusion island contribution to the cost/watt, is actually an increasing function of b. Thus, unsurprisingly, we find that minimizing b minimizes C. Invoking the inequality given in Eq. (2.40) gives the design value $b = 1.0\,\mathrm{m}$. The sensitivity of the cost/watt to b is shown in Fig. 2.6.

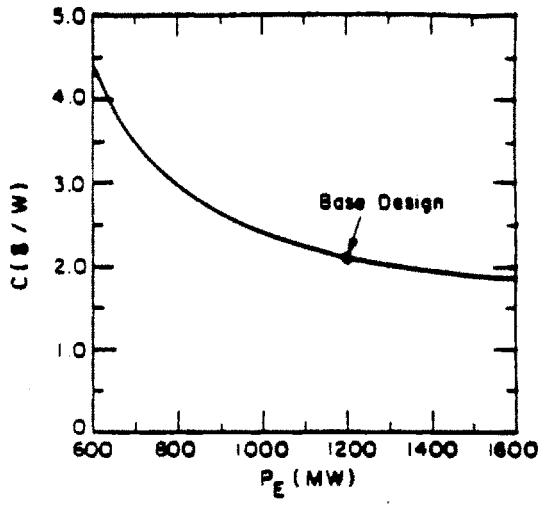

Figure 2.5: *Sensitivity of C to variations in P_E for $c_M = 1.8 \times 10^{20}\,\mathrm{m}^{-2} \cdot \mathrm{T}^{-1}$ and all other parameters fixed at their base design values.*

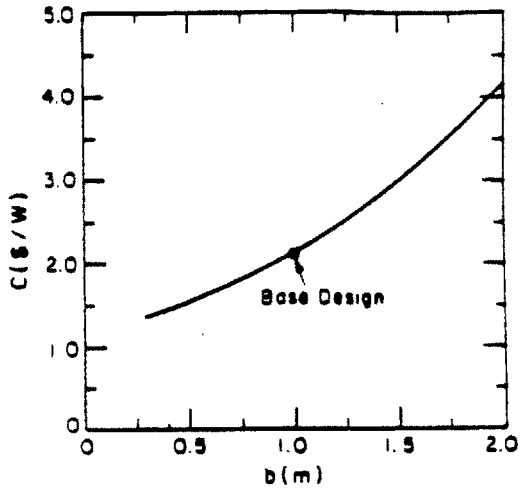

Figure 2.6: *Sensitivity of C to variations in b for $c_M = 1.8 \times 10^{20}\,\mathrm{m}^{-2} \cdot \mathrm{T}^{-1}$ and all other parameters fixed at their base design values.*

2.3.6 Optimization with respect to Thermal Conversion Parameters

In Eq. (2.46) we see that maximizing the quantity ηM reduces the cost of both the fusion island and the balance of plant. This, along with Eqs. (2.38) and (2.39), leads to the choices $\eta = 42\,\%$ and $M = 1.2$ for the design. Large values of ηM are beneficial because they reduce the amount of fusion power that must be generated to produce a given P_E. This, in turn, reduces the plasma volume and the turbine plant size.

2.3.7 Optimization with respect to Elongation

Equation (2.51) shows that ϵ_b increases with κ_a. Hence, Eq. (2.46) predicts that C is minimized by operation at large vertical elongations. Referring to Eq. (2.33)), the base design is characterized by $\kappa_a = 2.0$.

The Troyon limit suggests that values of κ_a above the vertical stability limit might be beneficial for reactor performance in that larger β_t values are then allowed. This has led to proposals for reactor configurations characterized by extremely high elongations [37]. However, vertical stability issues aside, it may be too optimistic to assume that β_t increases linearly with κ_a for large values of κ_a. Some authors have reported that the κ_a scaling in the Troyon limit may saturate or even eventually decrease with κ_a [4]. We model this effect by writing the β limit in the form

$$\beta_t = \hat{c}_\beta(\kappa_a, \kappa_s)\,\frac{\epsilon\kappa_a}{q_i}, \tag{2.57}$$

where

$$\hat{c}_\beta \equiv c_\beta\,\frac{1+\kappa_s}{\kappa_a+\kappa_s} \tag{2.58}$$

and κ_s is a parameter that reflects the saturation of β_t with increasing κ_a. With this modification the power balance constraint takes the form

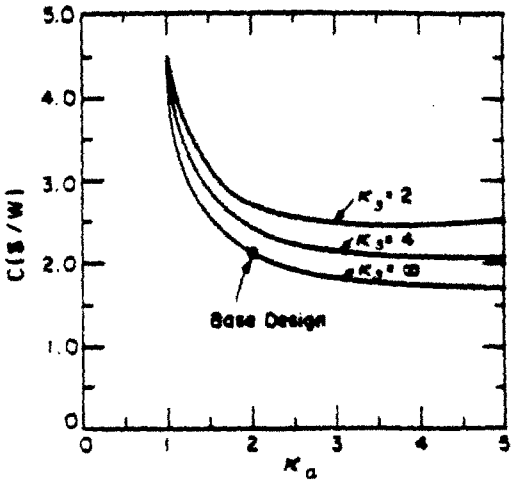

Figure 2.7: *Sensitivity of C to variations in κ_a and κ_s for $c_M = 1.8 \times 10^{20}\,\mathrm{m}^{-2} \cdot \mathrm{T}^{-1}$ and all other parameters fixed at their base design values.*

$$\hat{G}(\epsilon, \epsilon_b, \kappa_a, \kappa_s) \equiv \frac{\epsilon^4(1-\epsilon-\epsilon_b)^2\kappa_a^3(1+\kappa_s)^2}{\epsilon_b G_{TF}^2(\kappa_a+\kappa_s)^2}. \tag{2.59}$$

Note that as κ_s approaches infinity (i.e. no saturation) we see that $\hat{G}$ reduces to G.

Figure 2.7 shows that, in the case where $\kappa_s = \infty$, increasing the elongation always improves reactor performance. This is due to the favorable κ_a scaling of the β limit. However, the decrease in C becomes less pronounced as κ_a increases and C becomes almost constant when $\kappa_a \approx 3$. The reason for this is that as the plasma elongates, the length of the inner TF leg also tends to increase. The resulting increase in coil resistance partially cancels the beneficial contribution of increased β_t.

Unsurprisingly, Fig. 2.7 also shows that the benefits of high elongations are reduced as the value of the parameter κ_s decreases. In fact, for moderate values of κ_s a broad minimum in the cost is observed; that is, there is an

optimum κ_a. The observation that the C vs. κ_a curve saturates or even displays a minimum are, again, unexpected from considerations of the β limit alone.

2.3.8 Optimization with respect to Recirculating Power Fraction

The value of C exhibits a minimum for some f_R between zero and one. This behavior is explained as follows. In the limit of large f_R, C is dominated by C_{BP} which, from Eq. (2.46), is seen to increase with f_R. Specifically, increasing f_R at constant P_E necessitates a corresponding increase in P_R. Power balance then requires that P_F increase as well. This increased thermal output leads to the need for larger thermal conversion facilities which, in turn, causes C_{BP} to increase. In the limit of small f_R, C_{FI} dominates C since the TF coil thickness must be increased in order to attain small values of P_R. This leads to an increase in the volume and cost of the fusion island.

As Fig. 2.8 shows, C is minimized for a value $f_R = 0.32$. Unfortunately, this optimum design is characterized by a wall loading which exceeds the maximum value given by Eq. (2.36). We thus choose $f_R = 0.25$ to satisfy that constraint. Because of the broad nature of the minimum, this choice results in only a marginally higher value of C.

In the context of this model there are relatively large uncertainties associated with the optimization of f_R. First, the wall loading inequality used here is not a sharp limit; there is a substantial variation in the maximum P_W allowed by different scientists working in the field. Second, the exact location of the minimum is actually not well known anyway since it is sensitive to the details of the costing model which is highly idealized in this analysis. Finally, the model does not consider factors (such as the cost of TF magnet power supplies) which might further limit the desirability of large values of

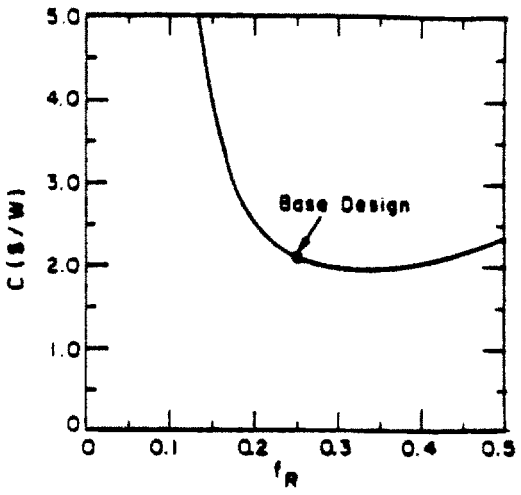

Figure 2.8: *Sensitivity of C to variations in f_R for $c_M = 1.8 \times 10^{20}\,\mathrm{m}^{-2} \cdot \mathrm{T}^{-1}$ and all other parameters fixed at their base design values.*

f_R. However, even with these considerations, the base design value $f_R = 0.25$ is consistent with results obtained by more sophisticated studies [10].

2.3.9 Optimization with respect to Peak Temperature

We see from Eq. (2.50) that ϵ_b increases with $W(T_0)$. Equation (2.46) then suggests that $W(T_0)$ should be maximized in order to yield the lowest cost. Integrating Eq. (2.5) numerically shows that $W(T_0)$ has a broad maximum at $T_0 = 17.5\,\mathrm{KeV}$ where $W(T_0) = 2.25\,\mathrm{MW} \cdot \mathrm{m}^{-3} \cdot \mathrm{T}^{-4}$. Clearly, this is the desired operating point in the absence of other constraints.

2.3.10 Calculation of Derived Variables

Given the independent variables, it is now possible to complete the design by calculating the derived quantities (including, in this case, c_M). These values are shown in Table 2.1. These results show that resistive-magnet

tokamak reactors possess several unique features. In particular, we see that the base design is characterized by low field ($B_0 = 4.5\,\mathrm{T}$), moderate beta ($\beta_t = 8.1\,\%$), moderate wall-loading ($P_W = 5.0\,\mathrm{MW/m^2}$), and large plasma current ($I_p = 19\,\mathrm{MA}$). We also notice that both Neo-Alcator and Mirnov scaling predict longer confinement times than that required by the ignition constraint, Eq. (2.37). However, ignition is clearly not possible according to Kaye-Goldston scaling. Finally, we see that resistive-magnet tokamak reactors are particularly vulnerable to the Murakami limit due to the low values of B_0. Specifically, $c_M \approx 1.8 \times 10^{20}\,\mathrm{m^{-2} \cdot T^{-1}}$ is required to allow operation at the maximum $W(T_0)$.

2.4 Optimization II

The value of c_M calculated in the previous section is more than a factor of two higher than that obtainable in present-day experiments. In view of the experimental progress already made towards extending the Murakami limit, it does not seem unreasonable to assume that eventually values of c_M of this magnitude might be achievable in tokamaks. If, on the other hand, c_M cannot be increased, then Eq. (2.35) becomes an additional constraint on the design, T_0 is eliminated as an independent variable, and the optimization procedure is again performed. Qualitatively, the procedure is identical to that just presented so the details are omitted. The results of this modified optimization are shown in Table 2.1 for $c_M = 0.8 \times 10^{20}\,\mathrm{m^{-2} \cdot T^{-1}}$.

In Table 2.1 we see that a significant rise in T_0 has accompanied the decrease in c_M. This effect is explained on the basis of Eq. (2.34). As c_M decreases n_0 must decrease accordingly. Since P_E is fixed, β_t is more or less fixed and T_0 must rise to produce the necessary plasma pressure. Reducing β_t (by raising q_i for example) would lower T_0 but, as the previous results have shown (see Fig. 2.4 for example), this would lead to a large increase in C.

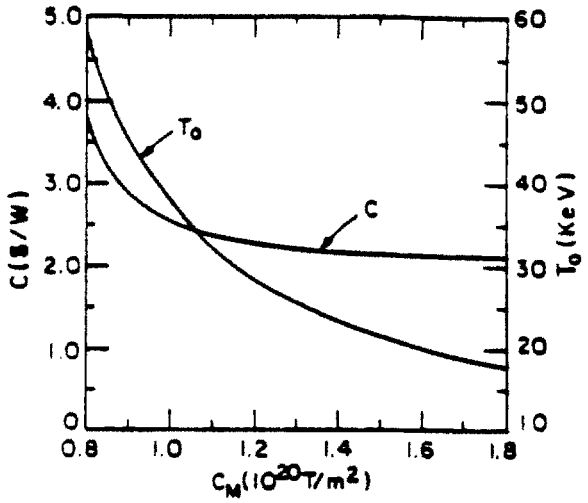

Figure 2.9: *Sensitivity of C and T_0 to variations in c_M with all other parameters fixed at their base design values.*

Table 2.1 also shows that, in addition to imposing stiffer requirements on plasma heating technology, the temperature increase causes the reactor to become larger and costlier due to a decrease in $W(T_0)$. Despite this, the ignition inequality is still satisfied if either Neo-Alcator or Mirnov scaling applies although the ignition margin is smaller. The sensitivity of C to variations in c_M is shown in Fig. 2.9. The economic penalty for operation at low values of c_M is seen to be substantial.

2.5 Discussion

We have developed a simple analytic model which provides reliable qualitative and semi-quantitative information about the design of a fusion reactor. As a specific example, a resistive-magnet tokamak reactor has been investigated. Our goal has been the design of a reactor, optimized with respect to

cost and subject to the constraints of favorable plant power balance and first region of stability beta scaling.

As a general comment, the results show that resistive-magnet tokamak reactors are somewhat more compact than their superconducting counterparts primarily because less shielding is required. The design is to a large measure dominated by the ohmic losses in the central leg of the TF coil. To keep the losses to an acceptable level, the toroidal field in the center of the plasma is approximately 3–5 T, a noticeably smaller value than anticipated in superconducting reactors. Thus, the resistive coils are not dominated by stress or current density considerations. Also, the low field may require operation at lower densities and higher temperatures than are optimal from the $\langle \sigma v \rangle$ reaction rate curve because of the Murakami density limit. These high temperatures have been shown to have a significant adverse effect on overall reactor performance. Experimental progress in raising the critical Murakami density could greatly enhance the prospects for resistive-magnet tokamak reactors.

The primary focus of the analysis has been the investigation of the desirability of high beta in an overall reactor design as achievable by different methods suggested by a first region of stability β_t limit [Eq. (2.27)]. The results from the analysis are as follows:

1. Raising the coefficient c_β is desirable. However, $c_\beta = 0.165$ used in the design is already near its maximum value since it has been determined by an optimization over profiles and cross-sections. In practice, it is more likely that c_β will be somewhat lower than 0.165 because the optimized profiles may not be realized. If the achievable value is much less than the base design value a large economic penalty could be paid. On the other hand, once the design value is obtained further improvements yield small cost savings.

2. Increasing ϵ raises the β_t limit but has a serious adverse effect when the aspect ratio becomes too tight. Specifically, as ϵ increases at fixed major radius, the cross-sectional area of the central TF leg decreases. This, in turn, raises the the ohmic power dissipated leading to an unfavorable plant power balance. In practice, there is an optimum aspect ratio which balances the favorable ϵ scaling of β_t with the unfavorable ϵ scaling of P_R. For our design, the optimum is a relatively steep function of ϵ and has a value $\epsilon = 0.37$.

3. Increasing κ_a raises the β_t limit and, for $\kappa_a < 2$, has a strong favorable effect on overall reactor performance. However, these desirable effects become less pronounced at high elongations. As κ_a increases, the center leg of the TF coil becomes longer. This leads to an increase in the ohmic dissipation. For very large κ_a, the gains in fusion power due to increased κ_a are essentially canceled by the increased ohmic losses. Consequently, once $\kappa_a > 3$, the net gain in reactor performance due to elongation saturates and further increases in κ_a do not lead to reduced costs. The benefits of elongation are further reduced by the possibility of a saturation in the β_t limit for large κ_a. In this case there is an optimum elongation although the optimum is quite broad as a function of κ_a. Finally, high elongation may be difficult to achieve in an actual experiment because of axisymmetric ($n = 0$) modes.

4. In general, operation at low q_i is desirable for improved reactor performance since increased toroidal current leads to higher values of β_t. This effect is relatively strong until the base design value, $q_i = 1.5$, is obtained. Then, lowering q_i does not significantly reduce plant costs. However, there are large uncertainties as to whether the base design value could be obtained in practice. First, large plasma currents could greatly complicate the design of the PF and OH coil systems. This

effect will be illustrated in Chapter 4. Second, and perhaps more important, there is some confusion as to whether q_i or q_a is the critical parameter for stability. In large aspect ratio circular plasmas these quantities are identical. In tight aspect ratio non-circular plasmas they are quite different and can lead to dramatically different design strategies. Because of arguments concerning the presence of a separatrix near the plasma surface, it appears that q_i is the relevant stability parameter. Finally, the scaling for the minimum of q_i for stability is not well established at present. The determination of the true form of the MHD kink/disruption limit, which might be a function of ϵ and κ_a, remains an important problem for the fusion physics community.

In summary, our simple analytic model demonstrates how theoretical and experimental physics laws impact the design of a tokamak reactor. We have investigated various paths to high beta based on first stability scaling laws and determined which of these is most promising from the viewpoint of overall reactor desirability. Perhaps surprising to some, our results show that, in certain cases, raising β_t can lead to a negligible or even adverse effect on overall reactor performance.

Chapter 3

Variational Equilibrium

Due to its obvious relevance to tokamak performance, the calculation of toroidally axisymmetric equilibria has long been the object of intense theoretical interest. In its simplest form, this problem consists of solving the Grad-Shafranov equation [13,14]

$$\Delta^*\psi = -\mu_0 R J_\varphi(R, \psi) \tag{3.1}$$

subject to the boundary condition

$$\psi\,|_{S_p} = 0 \tag{3.2}$$

(S_p denotes the surface of the plasma) and the constraint that the flux function ψ remains regular at the magnetic axis. Since it is assumed that the plasma shape does not vary during this calculation, this is often called the "fixed boundary" equilibrium problem.

The Δ^* operator is defined

$$\Delta^*\psi(R,Z) \equiv R\frac{\partial}{\partial R}\left(\frac{1}{R}\frac{\partial\psi}{\partial R}\right) + \frac{\partial^2\psi}{\partial Z^2} \tag{3.3}$$

and the toroidal current density J_φ is written

$$\mu_0 J_\varphi(R,\psi) = \mu_0 R p'(\psi) + \frac{1}{R} F F'(\psi), \tag{3.4}$$

where $p(\psi)$ and $F(\psi)$ are the usual free functions relating to the pressure and toroidal field profiles. Note that we have adopted the convention that the prime-operator ($'$) denotes differentiation of a function with respect to its argument.

Since the Δ^* operator is elliptic and the boundary condition is of the Dirichlet form, we can conclude that the problem is mathematically well-posed [38]. However, for most realistic choices of $p'(\psi)$ and $FF'(\psi)$, the Grad-Shafranov equation is nonlinear. Also, for reasons of MHD stability, plasma cross sections tend to have complicated dee or bean shapes. As a result, solving the Grad-Shafranov equation in general is quite difficult.

Nevertheless, analytic solutions have been found for special choices of geometry and/or profiles [39]. For instance, inverse aspect ratio expansions have been employed to describe conventional and high-beta tokamaks with circular cross-sections [40,41]. Also, judicious choices for the form of the free functions ($p'(\psi) = -A$, $FF'(\psi) = -C$ where A and C are constants) have produced good results for rather complex geometries [42,43]. Finally, by assuming that current flows only on the surface of the plasma, Freidberg and Haas were able to develop an analytic equilibrium model valid for arbitrary shapes [44]. These calculations have been very successful at yielding qualitative and semi-quantitative information regarding the properties of toroidal equilibria. However, in order to accurately analyze most present-day tokamaks, it is necessary to solve the Grad-Shafranov equation with all of its generality. This can be accomplished only through the use of numerical techniques.

Over the years, a number of computer programs have been written to solve for tokamak equilibria. Three of the most commonly used codes today are NEQ [45], developed at Oak Ridge National Laboratory; PEST [46,47],

developed at Princeton University; and GAEQ [48], developed at GA Technologies, Inc. These three codes employ sophisticated finite-difference techniques to solve the Grad-Shafranov equation to high accuracy. As a result, they have been very successful in predicting experimental equilibrium properties of tokamaks.

Despite their accuracy, there are some applications for which the exact equilibrium codes are simply not suitable. As an example, consider the classic problem of inverse equilibrium determination. Here, the goal of the analysis is to reconstruct the shape of the plasma flux surfaces and the toroidal current density profile from experimentally obtained magnetic probe and x-ray tomography data. Furthermore, in order to be a useful on-line experimental tool for between shot analysis, it is necessary that results be obtainable in a few seconds on a non-vectorizing mainframe computer such as a Vax 11/780. Unfortunately, a typical equilibrium calculated by NEQ, PEST, or GAEQ requires 20–400 secs of CPU time on a Cray-XMP supercomputer. Since a Vax is typically 10–60 times slower than a Cray, the wait for results would be unacceptably long.

Clearly an extremely fast equilibrium solver would be desirable for the purposes of inverse equilibrium calculation. Another application where speed is particularly important is the problem of scanning a range of plasma parameters to determine an optimal design. Suppose, for instance, one wished to incorporate equilibrium information into the resistive-magnet tokamak reactor design optimization discussed in the last chapter. To thoroughly investigate the variation of C with respect to even a few parameters could potentially require hundreds of equilibria which, even on a Cray, could require a prohibitive amount of computer time. Even if the computer time was available, the conventional equilibrium codes might still not be desirable for this purpose because of the obvious desire to accomplish the scan in a semi-automatic fashion. Specifically, NEQ, PEST, and GAEQ typically have complicated input files and their convergence to a reasonable answer

is relatively sensitive to various initial parameter specifications. Hence, it is not clear that a wide variety of cases could be considered without significant human intervention.

On the basis of the above examples, one can conclude that there are applications where the speed, ease-of-use, and robustness of an equilibrium solver are of primary importance. However, it should also be realized that these qualities cannot be obtained without cost since NEQ, PEST, and GAEQ use state-of-the-art numerical techniques to find the exact solution of the Grad-Shafranov equation as efficiently as is currently possible. In particular, dramatic increases in execution speed can be achieved only by giving up some accuracy in the solution. In many cases, this is a desirable trade-off. For example, in the case of the inverse equilibrium determination, it is probable that equilibrium errors on the order of the expected experimental measurement errors could be tolerated. This reasoning also holds for the resistive-magnet tokamak reactor design optimization where small errors in the equilibria would be offset by the fairly rough approximations made elsewhere in the model.

In this chapter we discuss methods, based on variational techniques, through which an approximate fixed boundary equilibrium—valid for general choices of geometry and profiles—can be obtained in less than one second on a Vax 11/780 and in a few minutes on a Macintosh personal computer. We then demonstrate that, despite the computational speed at which they are obtained, these approximate equilibria agree very well with exact calculations.

3.1 Variational Formulation

Variational techniques [49] are concerned with the search for functions that minimize an integral relation called a Lagrangian. When the Lagrangian is correctly defined, these techniques prove to be quite powerful tools for the solution of very complicated differential equations.

In the case of the Grad-Shafranov equation, the Lagrangian is written

$$\mathcal{L} = \int_{A_p} L \, dR \, dZ, \tag{3.5}$$

where the integration is over the cross-section of the plasma and L is the Lagrangian density defined

$$L = \frac{1}{R}(\nabla\psi)^2 - 2\mu_0 R p(\psi) - \frac{1}{R}F^2(\psi). \tag{3.6}$$

We can take the variation of the Lagrangian with respect to ψ by letting $\psi \rightarrow \psi + \delta\psi$. This variation in ψ produces a corresponding variation in $\mathcal{L}$ of the form

$$\begin{aligned} \delta\mathcal{L} \;=\; 2\int_{A_p} \Bigg\{ \frac{1}{R} \Bigg[& \frac{\partial\psi}{\partial R}\frac{\partial\delta\psi}{\partial R} + \frac{\partial\psi}{\partial Z}\frac{\partial\delta\psi}{\partial Z} - \\ & \Big(\mu_0 R^2 p'(\psi) - F F'(\psi)\Big)\,\delta\psi \Bigg] \Bigg\} \, dR \, dZ. \end{aligned} \tag{3.7}$$

Integrating Eq. (3.7) by parts and applying the condition that $\delta\psi = 0$ on the surface of the plasma yields

$$\delta\mathcal{L} = -2\int_{A_p} \left\{ \frac{1}{R}\left[\Delta^*\psi + \mu_0 R^2 p'(\psi) + F F'(\psi)\right]\delta\psi \right\} dR \, dZ. \tag{3.8}$$

On the basis of Eq. (3.8), we can see that since $\delta\psi$ is an arbitrary variation, the only choice for ψ that will make the Lagrangian stationary (i.e. $\delta\mathcal{L} = 0$) is a solution of the Grad-Shafranov equation. Hence, finding the stationary values of the Lagrangian is equivalent to solving the original partial differential equation.

For finding the exact solution to the Grad-Shafranov equation, variational techniques offer no obvious advantages over conventional techniques. The power of the method lies instead in the ability to use the Lagrangian to construct accurate approximate solutions. This is accomplished by substituting a set of trial functions or "guesses" into the Lagrangian. It is not necessary that the trial functions satisfy the Grad-Shafranov equation or even the boundary conditions though the closer they are to the correct solution, the better the final approximation will be. If the set of trial functions is general enough to include the exact solution, the discussion above demonstrates that this result can be identified since it causes the Lagrangian to be stationary. If, on the other hand, a limited set of trial functions is used, the one that causes the Lagrangian to be stationary represents the best guess for the solution out of all the trial functions considered. Moreover, it can be shown that should the optimal trial function be used to calculate certain integral quantities, their accuracy will be greater than that of the trial function itself.

The ability to use the Lagrangian to pick out optimal trial functions offers the potential for an enormous reduction in the difficulty associated with solving the Grad-Shafranov equation. This is because a small set of trial functions that very accurately approximate the exact solutions of the Grad-Shafranov equation can be readily deduced. As a result, the process of finding the optimal trial function turns out to be very simple and quick. For example, Lao, *et al.* [50,51] employed a variational approach to reduce the tokamak equilibrium problem to that of solving a set of coupled ordinary differential equations. Also, Choe and Freidberg [52] applied variational techniques to analytically compute stellarator and high beta tokamak equilibria for use in

ballooning calculations. In this thesis, a series of trial functions will be used to enable us to find accurate, approximate solutions to the Grad-Shafranov equation by simply minimizing a function of a few variables.

3.1.1 Introduction of Normalized Flux

In practice, it is not convenient to solve the equilibrium problem as it is formulated above [Eqs. (3.1) and (3.2)]. This is due to the nonlinear appearance of ψ in Eq. (3.4). Experience has shown that this nonlinearity tends to introduce instabilities into the numerical algorithms used to search for the optimal ψ. Since code robustness is a major goal of the present calculation, this behavior is unacceptable. Also unacceptable are problems associated with the accurate specification of profile shapes. For purposes of illustration, assume the pressure profile is written in the form

$$p(\psi) = p_0\psi^2(1 + \alpha\psi^2).$$

While it is clearly possible to guarantee that $p = 0$ at the plasma edge, it is very difficult to specify the pressure at the magnetic axis (ostensibly controlled by p_0) or the width of the pressure profile (ostensibly controlled by α) since the magnitude of ψ on axis is not known initially. Clearly, it would be desirable to be able to exercise more control over the profiles than this.

With minor modifications, it is possible to state the problem in an equivalent manner that alleviates the above concerns. Since the flux label in p and F is arbitrary, Eq. (3.4) can be re-written in the following manner

$$J_\varphi(R,\tilde{\psi}) = -\frac{C}{\mu_0}\left[b_p\frac{R}{R_0}h'_p(\tilde{\psi}) + (1-b_p)\frac{R_0}{R}h'_f(\tilde{\psi})\right], \tag{3.9}$$

where C and b_p are constants; $h'_p(\tilde{\psi})$ and $h'_f(\tilde{\psi})$ formally replace p' and FF' respectively; and $\tilde{\psi}$ is defined

$$\tilde{\psi} \equiv \frac{\psi}{\psi_0}. \tag{3.10}$$

ψ_0 specifies the flux at the magnetic axis which, for future reference, is assumed to be located at $R = R_m$, $Z = 0$. Hence, $\tilde{\psi}$ represents a version of the flux function normalized to unity at the magnetic axis. Substituting Eqs. (3.9) and (3.10) into Eq. (3.1) yields

$$\psi_0 \Delta^* \tilde{\psi} = -\mu_0 R J_\varphi(R, \tilde{\psi}) \tag{3.11}$$

as the new, but equivalent, form of the Grad-Shafranov equation which must be solved subject to the transformed boundary condition

$$\tilde{\psi} \mid_{S_p} = 0. \tag{3.12}$$

The major advantage of the modified form of the problem is that the free functions now depend only on the shape of the flux rather than its magnitude. This allows much greater control over profiles to be exercised while at the same time improving the numerical robustness of solution algorithms.

Another consequence of the reformulation is that the Lagrangian describing the Grad-Shafranov equation must be modified. Referring to Eq. (3.6), we can see that the modified Lagrangian takes the form

$$\tilde{\mathcal{L}} = \int_{A_p} \tilde{L}\, dR\, dZ, \tag{3.13}$$

where

$$\tilde{L} = \frac{\psi_0}{R}(\nabla\tilde{\psi})^2 + 2C\left[b_p \frac{R}{R_0} h_p(\tilde{\psi}) + (1 - b_p)\frac{R_0}{R} h_f(\tilde{\psi})\right]. \tag{3.14}$$

Furthermore, if we vary $\tilde{\psi}$, we can see that this yields a correct variational principle for Eq. (3.11), assuming that ψ_0 is held fixed.

In the original problem, ψ_0 was calculated as a natural result of the minimization of $\mathcal{L}$ with respect to ψ. In the modified problem, ψ_0 cannot be varied. This fundamentally different behavior can explained as follows. Suppose we minimize $\tilde{\mathcal{L}}$ with respect to a class of trial functions for $\tilde{\psi}$ that is completely general, satisfying only the boundary condition $\tilde{\psi} = 0$ on the surface and $\tilde{\psi} = 1$ at the magnetic axis. Since we have shown previously that the problem is mathematically well-posed, a $\tilde{\psi}$ that minimizes $\tilde{\mathcal{L}}$ will be found for any value of ψ_0. However, in general, the calculated $\tilde{\psi}$ will *not* satisfy Eq. (3.11). Specifically, only one particular value of ψ_0 will result in the Grad-Shafranov equation being exactly satisfied. Hence, in the modified problem, ψ_0 acts as a normalization constant that must be chosen in accordance with Eq. (3.11).

When the class of trial functions is general, ψ_0 can be chosen to ensure exact equality of the left and right sides of Eq. (3.11) throughout the entire plasma. However, in this thesis, a finite set of trial functions will be used to obtain approximate solutions; so, Eq. (3.11) will usually not be satisfied everywhere inside the plasma. Hence, the correct choice of ψ_0 is less clear. One possibility is to multiply Eq. (3.11) by $\tilde{\psi}^n$—where n is a constant—and integrate over the plasma cross-section (i.e., take the nth moment). This will yield an infinite number of correct relations; but, due to the approximate nature of the solutions for $\tilde{\psi}$, each will also give a slightly different value of ψ_0. The accuracy of the ψ_0 values resulting from a number of these moment equations has been investigated and it has been found that an iterative procedure based on the $n = 1$ moment

$$\psi_0 = -C \frac{\int_{A_p} \left[b_p \frac{R}{R_0} h_p'(\tilde{\psi}) + (1 - b_p) \frac{R_0}{R} h_f'(\tilde{\psi}) \right] \tilde{\psi} \, dR \, dZ}{\int_{A_p} \frac{1}{R} (\nabla \tilde{\psi})^2 \, dR \, dZ} \tag{3.15}$$

gives extremely good agreement with exact equilibria while, at the same time, being easy to implement in a computational sense. This procedure will be described in Section 3.1.4.

The last step required in order to completely define the modified problem is the specification of the free functions. A convenient choice that models a wide variety of profiles is

$$h'_{p,f} = \frac{\exp[-\alpha_{p,f}(1-\tilde{\psi})] - \exp(-\alpha_{p,f})}{1-\exp(-\alpha_{p,f})}, \tag{3.16}$$

where α_p and α_f are parameters that control the steepness of $h'_p(\tilde{\psi})$ and $h'_f(\tilde{\psi})$ respectively. As Fig. 3.1 shows, the more negative these values become, the flatter the profiles get. In any event, $h'_p(\tilde{\psi})$ and $h'_f(\tilde{\psi})$ are constrained to vary between 0 (indicating that the plasma current vanishes smoothly at the plasma edge) and 1.

The two constants b_p and C represent normalizations for the pressure and toroidal current profiles. From Eq. (3.9), we can see that b_p is related to the poloidal beta and that C is related to the total plasma current

$$I_p = \frac{C}{\mu_0}\int_{A_p}\left[b_p\frac{R}{R_0}h'_p(\tilde{\psi}) + (1-b_p)\frac{R_0}{R}h'_f(\tilde{\psi})\right]\,dR\,dZ. \tag{3.17}$$

3.1.2 Transformation to Inverse Coordinates

A few more manipulations are required to cast the problem into a form convenient for numerical computation. This extra work is required because the usual cylindrical (R,φ,Z) coordinates make evaluation of the Lagrangian difficult for the complicated plasma shapes we wish to study. It would be desirable to transform the equations to a coordinate system more closely tied to plasma and flux surface shape. Luckily, a suitable set of so-called "inverse" coordinates exists [53].

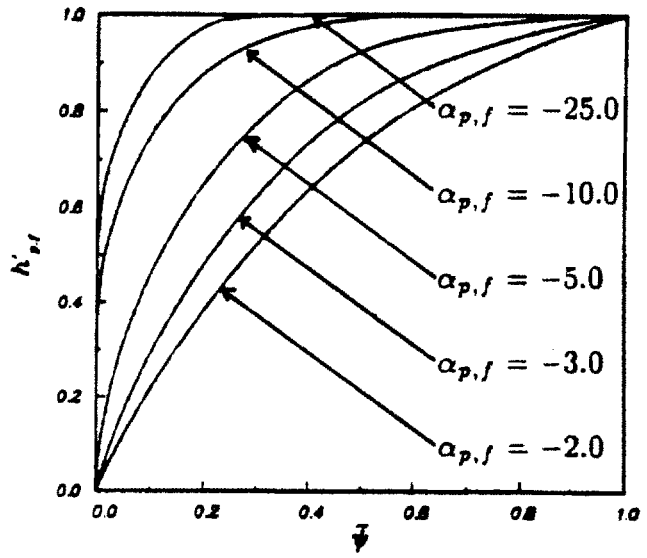

Figure 3.1: *Dependence of Profile Shape on* $\alpha_{p,f}$.

The inverse coordinates form a right-handed system consisting of ρ, a radial coordinate; φ, the usual ignorable toroidal angle coordinate; and μ, a poloidal angle coordinate. Without losing any generality, it is possible to parameterize the plasma surface by the expression $\rho = 1$ and fix the location of the magnetic axis at $\rho = 0$. Furthermore, we can assume that as μ varies from 0 to 2π, a single poloidal circuit is completed. A typical set of inverse coordinate contours for a dee-shaped plasma is depicted in Fig. 3.2. Note their close connection with plasma shape.

For now, we will assume that $\tilde{\psi}$ is a general function of both ρ and μ and examine the transformation to inverse coordinates in mainly formal terms. In the next section, the exact form of the coordinates employed in this thesis will be detailed.

To transform the Lagrangian, it is first necessary to transform the area element $dR\,dZ$. This is readily found to take the form

$$dR\,dZ = J\,d\rho\,d\mu, \tag{3.18}$$

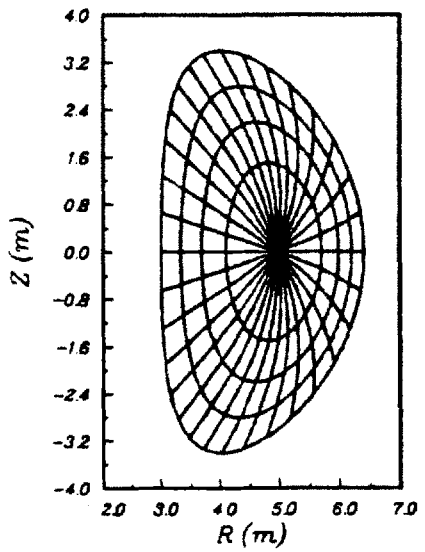

Figure 3.2: *Contours of constant ρ and μ for a typical plasma.*

where J represents the jacobian for the transformation

$$J = \begin{vmatrix} R_\rho & R_\mu \\ Z_\rho & Z_\mu \end{vmatrix} = R_\rho Z_\mu - R_\mu Z_\rho, \tag{3.19}$$

and we have adopted the convention that partial differentiation with respect to ρ and μ is denoted by a subscript. The components of $\nabla\tilde{\psi}$ can be similarly transformed (See Appendix A.):

$$\frac{\partial\tilde{\psi}}{\partial R} = \frac{Z_\mu}{J}\tilde{\psi}_\rho - \frac{Z_\rho}{J}\tilde{\psi}_\mu, \tag{3.20}$$

$$\frac{\partial\tilde{\psi}}{\partial Z} = -\frac{R_\mu}{J}\tilde{\psi}_\rho + \frac{R_\rho}{J}\tilde{\psi}_\mu. \tag{3.21}$$

Substituting into Eqs. (3.13) and (3.14) yields

$$\tilde{\mathcal{L}} = \int_0^{2\pi}\int_0^1 \tilde{L}\, d\rho\, d\mu, \tag{3.22}$$

where

$$\tilde{L} = \frac{\psi_0}{RJ}\left[(Z_\mu\tilde{\psi}_\rho - Z_\rho\tilde{\psi}_\mu)^2 + (R_\mu\tilde{\psi}_\rho - R_\rho\tilde{\psi}_\mu)^2\right] + 2CJ\left[b_p\frac{R}{R_0}h_p(\tilde{\psi}) + (1-b_p)\frac{R_0}{R}h_f(\tilde{\psi})\right]. \tag{3.23}$$

Since $\tilde{\mathcal{L}}$ is a scalar, its value should not be affected by a change of coordinates. In particular, the $\tilde{\psi}$ that makes the Lagrangian stationary should still be the one that solves the Grad-Shafranov equation. This can be verified by taking the variation of Eq. (3.22) with respect to $\tilde{\psi}$. After a little algebra involving several integrations by parts we find

$$\delta\tilde{\mathcal{L}} = -2\int_0^{2\pi}\int_0^1 \tilde{I}\,\delta\tilde{\psi}\,d\rho\,d\mu, \tag{3.24}$$

where

$$\tilde{I} = \frac{1}{R}\left[Z_\mu\frac{\partial\tilde{\psi}}{\partial R} - R_\mu\frac{\partial\tilde{\psi}}{\partial Z}\right]_\rho - \frac{1}{R}\left[Z_\rho\frac{\partial\tilde{\psi}}{\partial R} - R_\rho\frac{\partial\tilde{\psi}}{\partial Z}\right]_\mu - CJ\left[b_p\frac{R}{R_0}h_p'(\tilde{\psi}) + (1-b_p)\frac{R_0}{R}h_f'(\tilde{\psi})\right]. \tag{3.25}$$

Equation (3.24) shows that $\tilde{I} = 0$ is the condition required to make $\tilde{\mathcal{L}}$ stationary. From Appendix A, this condition is seen to be exactly equivalent to the Grad-Shafranov equation written in inverse coordinates.

The fact that $\tilde{\mathcal{L}}$, as a scalar, is unaffected by a coordinate transformation has a final very important implication. Namely, variations in R and Z—which are now functions of ρ and μ—subject to the constraint that the plasma shape doesn't change (i.e., $\delta R = \delta Z = 0$ on S_p), result in $\delta\tilde{\mathcal{L}} = 0$ only when $\tilde{\psi}$ satisfies the Grad-Shafranov equation. Specifically,

$$\delta\tilde{\mathcal{L}}^{(R)} = -2\int_0^{2\pi}\int_0^1 \tilde{I}\frac{\partial\tilde{\psi}}{\partial Z}\,\delta R\,d\rho\,d\mu, \tag{3.26}$$

$$\delta\tilde{\mathcal{L}}^{(Z)} = -2\int_0^{2\pi}\int_0^1 \tilde{I}\frac{\partial\tilde{\psi}}{\partial R}\,\delta Z\; d\rho\, d\mu. \tag{3.27}$$

These results are important because they imply that if we substitute trial functions for the shape of the flux surfaces, the variational principle will tell us which ones are optimal for approximating a solution to the Grad-Shafranov equation.

3.1.3 Choice of Trial Functions

Assuming up-down symmetry and topologically nested magnetic surfaces, it is possible to write R and Z in Fourier series in ρ and μ:

$$R(\rho,\,\mu) = \sum_{m=0}^{\infty} r_m(\rho)\cos m\mu, \tag{3.28}$$

$$Z(\rho,\,\mu) = \sum_{n=1}^{\infty} z_n(\rho)\sin n\mu. \tag{3.29}$$

This representation turns out to be quite general. For instance, by truncating the series at $m = 3, n = 1$, it is possible to model very exotic shapes ranging from spherical shells to "peapods" [54]. However, for this thesis, we will limit consideration to $m = 2, n = 1$. Nevertheless, as Fig. 3.3 shows, this choice includes the majority of shapes considered for experiments and reactors today: finite aspect ratio circles, ellipses, dees and beans.

The coordinate parameterization in Eqs. (3.28) and (3.29) is especially convenient if we also assume that ρ is a flux surface label. This corresponds to choosing the class of trial functions characterized by

$$\tilde{\psi} = \tilde{\psi}(\rho). \tag{3.30}$$

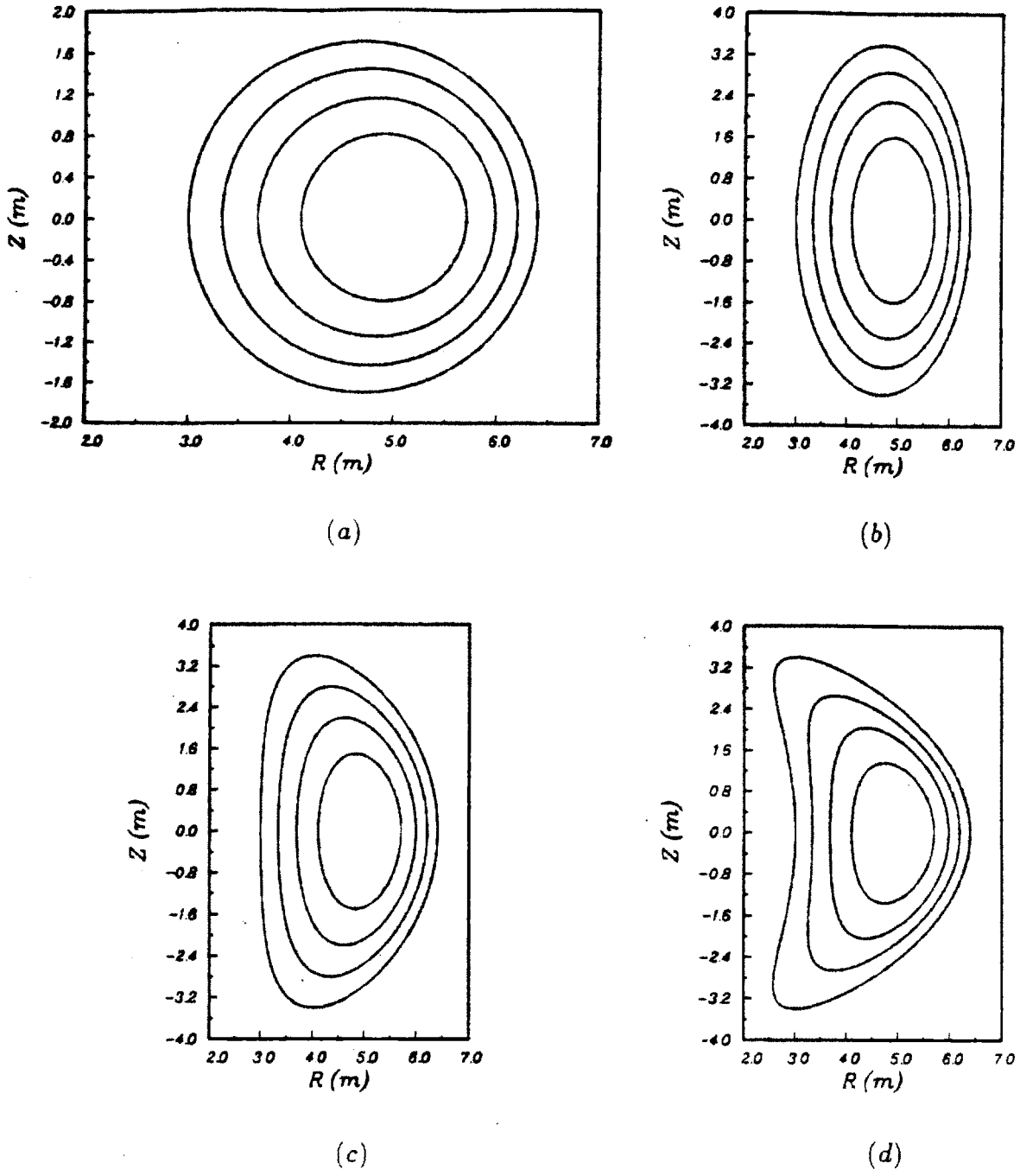

Figure 3.3: *Available shapes with assumed coordinate parameterizations.*

Then, $r_0(\rho)$ describes the shift of the flux surfaces, $r_1(\rho)$ and $z_1(\rho)$ describe their elongation, and $r_2(\rho)$ describes their triangularity. In many cases, this is an excellent approximation to the shape of flux surfaces in a tokamak.

Making ρ a flux surface label has the additional benefit of simplifying the form of the Lagrangian density in Eq. (3.23)

$$\tilde{L} = \psi_0 \frac{R_\mu^2 + Z_\mu^2}{RJ} [\tilde{\psi}'(\rho)]^2 + 2CJ \left[b_p \frac{R}{R_0} h_p(\tilde{\psi}) + (1 - b_p) \frac{R_0}{R} h_f(\tilde{\psi}) \right]. \quad (3.31)$$

This drastically reduces the computational effort required to evaluate the Lagrangian and is probably the single most critical assumption with respect to achieving the desired fast calculation speeds.

Before specifying the form of the shape functions $r_m(\rho)$ and $z_1(\rho)$, it is necessary to discuss their behavior near the magnetic axis and at the plasma surface. Near the magnetic axis, it is well known that the flux surfaces are very nearly shifted ellipses. In other words,

$$\lim_{\rho \to 0} R(\rho, \mu) = R_0 + a\sigma + a\rho \cos\mu + O(\rho^2), \quad (3.32)$$

$$\lim_{\rho \to 0} Z(\rho, \mu) = a\kappa_0 \rho \sin\mu + O(\rho^2). \quad (3.33)$$

In the relations above, σ represents the shift of the innermost flux surface and κ_0 represents its elongation. At the plasma surface, we choose the parameterization

$$R_p(\mu) = R_0 - \frac{a\delta_a}{2} + a\rho \cos\mu + \frac{a\delta_a}{2} \cos 2\mu, \quad (3.34)$$

$$Z_p(\mu) = a\kappa_a \sin\mu. \quad (3.35)$$

As was mentioned before, the set of shape functions that makes the Lagrangian stationary represents the optimal choice. If we do not further specify the functional form of the shape functions, the calculus of variations tells us that this optimal choice can be found using the Euler-Lagrange equations derived from Eq. (3.23). In this problem, these relations take the form of a set of coupled nonlinear ordinary differential equations whose boundary conditions are given by Eqs. (3.32)–(3.35). This type of system can be solved very efficiently on a vectorizing computer such as a Cray. However, an even simpler and potentially faster approach is to specify the functional form of the various shape functions in terms of a small number of parameters. Then, the Lagrangian can be minimized with respect to these parameters to find the optimal set.

For most applications, the following shape functions prove quite sufficient:

$$r_0(\rho) = R_0 + a\sigma(1-\rho^2) - \frac{a\delta_a}{2}\rho^2[\eta + (1-\eta)\rho^2], \tag{3.36}$$

$$r_1(\rho) = a\rho, \tag{3.37}$$

$$r_2(\rho) = \frac{a\delta_a}{2}\rho^2[\eta + (1-\eta)\rho^2], \tag{3.38}$$

$$z_1(\rho) = a\rho[\kappa_0 + (\kappa_a - \kappa_0)\rho^2]. \tag{3.39}$$

The variational parameters are σ, η, and κ_0. The shape function $r_1(\rho)$ has no variational parameter associated with it because the flux surface elongation is completely specified by Eq. (3.39) alone. Hence, any information imparted from Eq. (3.37) would be redundant.

The above choice of shape functions turns out to be very convenient. In particular, no iteration or searching is required to ensure that Eqs. (3.32)–(3.35) are satisfied: the construction of Eqs. (3.32)–(3.35) automatically guarantees that. Moreover, it is possible to continue to satisfy the boundary

conditions even when more variational parameters are introduced to achieve higher accuracy. For example, to obtain more information about flux surface elongation we could write

$$z_1(\rho) = a\rho[\kappa_0 + (\kappa_a - \kappa_0)\rho^2 + \lambda\rho^2(1-\rho^2)], \tag{3.40}$$

where λ is the new variational parameter. Notice that the additional term vanishes at both the magnetic axis and the plasma surface. This property also makes it easy to incorporate external information about flux surface shape. For instance, if κ_0 were known from experimental measurements, that variational parameter could be eliminated directly. Then, with no additional cost, a new variational parameter (such as λ) could be introduced.

In tokamaks, the normalized flux function $\tilde{\psi}$ is known to vary monotonically between the magnetic axis and the plasma surface. Furthermore, Ampere's law demands that $\tilde{\psi}'(0) = 0$ so that the poloidal magnetic field vanishes at the magnetic axis. This simple behavior suggests the parameterization

$$\tilde{\psi} = 1 - \nu\rho^2 - (1-\nu)\rho^4, \tag{3.41}$$

where ν is a variational parameter controlling the radial shape of the flux function. Note that this representation automatically satisfies the constraint that $\tilde{\psi}(0) = 1$ and the boundary condition Eq. (3.12).

3.1.4 Formal Statement of Solution Procedure

After many necessary theoretical preliminaries, it is now possible to summarize the solution procedure. In order to completely define the problem, there are nine inputs required. These are

$$R_0,\ a,\ \kappa_a,\ \delta_a,\ B_0,\ \alpha_f,\ \alpha_p,\ I_p,\ b_p.$$

Also, initially we must supply estimates for the variational parameters κ_0, σ, η, and ν. On the basis of these estimates, it is possible to calculate initial values of C and ψ_0 using Eqs. (3.15) and (3.17):

$$\psi_0 = -C \frac{\int_0^1 \int_0^{2\pi} \left[b_p \frac{R}{R_0} h_p'(\bar{\psi}) + (1 - b_p) \frac{R_0}{R} h_f'(\bar{\psi}) \right] \bar{\psi} \, J \, d\mu \, d\rho}{\int_0^1 \int_0^{2\pi} \frac{1}{R} (\nabla \bar{\psi})^2 \, J \, d\mu \, d\rho}, \tag{3.42}$$

$$\frac{1}{C} = \frac{1}{\mu_0 I_p} \int_0^1 \int_0^{2\pi} \left[b_p \frac{R}{R_0} h_p'(\bar{\psi}) + (1 - b_p) \frac{R_0}{R} h_f'(\bar{\psi}) \right] \, J \, d\mu \, d\rho. \tag{3.43}$$

With all other quantities being held fixed, the Lagrangian is formally only a function of the variational parameters

$$\bar{\mathcal{L}} = \bar{\mathcal{L}}(\kappa_0, \sigma, \eta, \nu).$$

The optimal choice of variational parameters is found by finding the stationary point of the Lagrangian, which for this case turns out to be a minimum. (The particular procedure for numerically finding this minimum is discussed in the next section.) Once this information has been obtained, an updated value of ψ_0 can be found using Eq. (3.42). Since the original ψ_0 was calculated on the basis of estimates, the updated ψ_0 will converge towards its exact value. To obtain a more accurate set of variational parameters, the minimization of $\bar{\mathcal{L}}$ can be repeated with the updated ψ_0. Usually, a few iterations of this procedure yields ψ_0 to excellent accuracy. After the final variational parameter values have been obtained, a final value of C can be obtained from Eq. (3.43) and a corresponding value of ψ_0 can be computed from Eq. (3.42). Since C and ψ_0 are both scaled by the same amount, there is no need to calculate a new set of variational parameters as Eq. (3.22) is seen to be invariant to such scalings.

The calculation of κ_0, σ, η, ν, ψ_0, and C completely specifies the equilibrium solution. These values can now be used be used to compute a series of additional quantities which further characterize the equilibrium.

To obtain the pressure and toroidal field profiles, $h'_p(\tilde{\psi})$ and $h'_f(\tilde{\psi})$ are integrated to yield

$$h_{p,f} = \frac{\exp[-\alpha_{p,f}(1-\tilde{\psi})] - \exp(-\alpha_{p,f})(1+\alpha_{p,f}\tilde{\psi})}{\alpha_{p,f}[1-\exp(-\alpha_{p,f})]} + const. \tag{3.44}$$

This result can then be used in the relations [obtained by comparing Eq. (3.4) and Eq. (3.9)]

$$p(\tilde{\psi}) = -\frac{C\psi_0 b_p}{R_0} h_p(\tilde{\psi}), \tag{3.45}$$

$$F^2(\tilde{\psi}) = B_T^2 R^2 = -C\psi_0 R_0(1-b_p)h_f(\tilde{\psi}) + B_0^2 R_0^2. \tag{3.46}$$

The constants of integration have been chosen to satisfy the boundary conditions $p(\tilde{\psi})\mid_{S_p} = 0$ and $F^2(\tilde{\psi})\mid_{S_p} = B_0^2 R_0^2$.

The poloidal field is computed using

$$\mathbf{B}_p = \frac{\psi_0 \nabla\tilde{\psi} \times \mathbf{e}_\varphi}{R} \tag{3.47}$$

along with Eqs. (3.20) and (3.21). Hence, the components are given by

$$B_R = \frac{R_\mu}{RJ}\psi_0\tilde{\psi}_\rho, \tag{3.48}$$

$$B_Z = \frac{Z_\mu}{RJ}\psi_0\tilde{\psi}_\rho \tag{3.49}$$

so the total poloidal field is written

$$B_p = \frac{\sqrt{R_\mu^2 + Z_\mu^2}}{RJ}\psi_0\bar{\psi}_\rho. \tag{3.50}$$

The profiles and fields may, in turn, be used to calculate such things as the MHD safety factor

$$q(\bar{\psi}) = \frac{F(\bar{\psi})}{2\pi}\int_0^{2\pi}\frac{\sqrt{R_\mu^2 + Z_\mu^2}}{R^2 B_p}\,d\mu, \tag{3.51}$$

the kink (Sykes) safety factor

$$q_i = \frac{aB_0}{R_0\bar{B}_p}, \tag{3.52}$$

the volume averaged toroidal beta

$$\beta_t = \frac{2\mu_0\langle p\rangle}{B_0^2}, \tag{3.53}$$

and the volume averaged poloidal beta

$$\beta_p = \frac{2\mu_0\langle p\rangle}{\bar{B}_p^2}, \tag{3.54}$$

where

$$\langle p\rangle = \frac{2\pi}{V_p}\int_0^{2\pi}\int_0^1 p(\bar{\psi})JR\,d\rho\,d\mu, \tag{3.55}$$

$$\bar{B}_p = \frac{\mu_0 I_p}{2\pi a\bar{\kappa}}, \tag{3.56}$$

and

$$V_p = 2\pi\int_0^{2\pi}\int_0^1 JR\,d\rho\,d\mu, \tag{3.57}$$

$$\bar{\kappa} = \frac{1}{2\pi a}\int_0^{2\pi}\sqrt{R_\mu^2 + Z_\mu^2}\,d\mu. \tag{3.58}$$

Table 3.1: *Representative Execution Times for ePFC on Various Systems*

Computer	Ellipse	Dee
Cray X-MP	0.023 sec	0.025 sec
Vax 11/780	0.67 sec	0.72 sec
Macintosh Plus	105 sec	124 sec
Amiga	13 sec	14 sec

3.2 Computer Implementation

The ideas of the previous section have been implemented in a computer program called "ePFC." This code, written in the C programming language [56], has been adapted to run on systems ranging from Cray X-MP supercomputers to Macintosh personal computers. Table 3.1 shows approximate execution times needed to calculate representative elliptical and dee-shaped equilibria. The times for elliptical equilibria are smaller because symmetry dictates that the variational parameter η is identically zero throughout the plasma so it need not be solved for. Table 3.1 shows that the desired <1 sec execution time for the Vax is readily achieved. In addition notice that, even when running on personal computers, ePFC is competitive timewise with conventional equilibrium codes that run only on supercomputers.

The fast execution times are largely attributable to simplifications resulting from the introduction of the normalized flux and the transformation to inverse coordinates. However, some equally important numerical optimizations were also applied. These are described below.

In a computational sense, our equilibrium problem consists of evaluating a function (the Lagrangian) many times. Since the Lagrangian is a double

integral, it is relatively time-consuming to compute; so, for speed, it is obviously desirable to minimize both the number of times the Lagrangian is evaluated and the amount of time required for a single evaluation.

The number of Lagrangian evaluations necessary to find the solution is largely a function of the efficiency of the numerical minimization algorithm employed. Several standard procedures — Powell's method, the Simplex method, and the Quasi-Newton method [55] — were investigated and discarded for various reasons. Instead, an intuitive procedure, consisting of the repeated minimization of the Lagrangian with respect to each of the variational parameters, was chosen. Specifically, the Lagrangian is varied with respect to one of the parameters with the others held fixed. Once a minimum is found, another parameter is varied with the previous parameter being held fixed at the value that minimized the Lagrangian. The parameters are cycled through in this manner until the Lagrangian stops decreasing. Though quite robust, this method is highly inefficient in general. However, it works well for this problem because very good initial guesses for the variational parameters can be supplied. For a typical problem requiring calculation of κ_0, σ, η, and ν, approximately 30–60 Lagrangian evaluations are required to find a minimum accurate to 0.01 %. (Here accuracy is defined as follows. Assume we have calculated two consecutive values of the Lagrangian: $\tilde{\mathcal{L}}^n$ and $\tilde{\mathcal{L}}^{n+1}$ where $\tilde{\mathcal{L}}^{n+1} < \tilde{\mathcal{L}}^n$. Each represents the minimum $\tilde{\mathcal{L}}$ with respect to two different variational parameters. The minimum $\tilde{\mathcal{L}}$ is considered determined if $\tilde{\mathcal{L}}^n - \tilde{\mathcal{L}}^{n+1} < 0.0001|\tilde{\mathcal{L}}^n|$.) Each time the Lagrangian is minimized, ψ_0 is recalculated using Eq. (3.15) and compared to the previous ψ_0. Generally 1–3 iterations are required to reduce the change in ψ_0 to less than 1 %. Thus, for most cases, 60–180 Lagrangian evaluations are needed to calculate an equilibrium.

The time required to evaluate the Lagrangian has been optimized primarily through the precalculation of many terms in the Lagrangian density.

This optimization is best described by example. Consider the fact that at a given (ρ, μ) position, it is possible to write schematically

$$R(\rho, \mu) = R^{(0)} + R^{(\sigma)}\sigma + R^{(\eta)}\eta, \tag{3.59}$$

where $R^{(0)}$, $R^{(\sigma)}$, and $R^{(\eta)}$ are functions *only* of ρ, μ, R_0, a, κ_a, and δ_a. Since, these values do not change during the minimization, they can be computed once initially and stored for later use. Then, for any given set of variational parameters, R can be computed using only two multiplications and three additions. Similar expressions can be written for Z, R_ρ, Z_ρ, R_μ, and Z_μ. By precalculating these quantities, thousands of unnecessary arithmetic operations and transcendental function evaluations can be saved. This optimization is extremely important. Its implementation results in nearly a factor of 20 speed increase over the case where no precalculation is performed.

3.3 Comparison with Exact Equilibria

To test the accuracy of the analysis just described, we will compare the results from ePFC with those from the exact two-dimensional code NEQ. Two cases will be focused on:

- A conventional ($\beta_p = 1$) tokamak somewhat modeled on the Versator experiment at M.I.T.,
- The resistive-magnet tokamak reactor base design presented in the previous chapter.

These cases were chosen because they straightforwardly illustrate the successes and limitations of the models.

Table 3.2: *Input Parameters for Conventional Tokamak Case*

Parameter	Value
R_0 (m)	0.40
a (m)	0.13
ϵ	0.33
κ_a	1.00
δ_a	0.00
B_0 (T)	0.70
α_p	-5.00
α_f	-3.32
I_p (MA)	0.01
b_p	1.0

3.3.1 Conventional Circular Tokamak

The input parameters for the conventional tokamak case are shown in Table 3.2. The plasma shape is that of a finite aspect ratio circle. Despite the simple geometry, this equilibrium cannot be calculated analytically due to the fact that the pressure profile is peaked. Another point of interest is the relatively large value of b_p: since this parameter is related to β_p, one expects that a finite Shafranov shift will result.

Various output parameters from ePFC and NEQ are compared in Table 3.3. Despite the large disparity in execution time, the results are seen to differ by no more than a few percent. This good agreement is also displayed in Fig. 3.4 which shows the flux surface shapes calculated by the two codes superimposed. The fact that the flux surface shapes agree well suggests that, despite their relative simplicity, the variational shape functions [Eqs. (3.36)–(3.39)] do an accurate job in modeling the plasma. This point is confirmed by Fig. 3.5 which shows that the relative flux surface shift

$$S \equiv \frac{R_{inner} + R_{outer} - 2R_0}{2a} \tag{3.60}$$

computed with ePFC and that computed by NEQ are almost identical. (Note that in Eq. (3.60) R_{inner} and R_{outer} describe the radial position at which the inner and outer edges of a specified flux surface cross the plasma midplane.) Finally, it is apparent from Fig. 3.6 that the flux function ψ is computed quite accurately. This supports the contention that, despite not being unique or variational, Eq. (3.15) represents an acceptable way to calculate ψ_0. It also implies that, in this case at least, Eq. (3.41) describes a reasonable parameterization for the radial variation in the flux function.

This case demonstrates that ePFC is capable of obtaining results in good agreement with those computed by NEQ. Furthermore, Table 3.3 shows that the ePFC results were calculated much faster than those from NEQ. However, one point regarding this comparison must be made. Namely, NEQ does not, in fact, solve the fixed boundary equilibrium problem described in Eqs. (3.1) and (3.2). It actually solves the more complicated "free boundary" problem which consists of the solution of the Grad-Shafranov equation and the simultaneous calculation of PF coil currents. For the cases displayed in this chapter, it is estimated that approximately 30 % of the execution time listed for NEQ is spent calculating the PF coil currents.

3.3.2 Strongly Shaped Tokamak

The achievement of high accuracy in the case of the circular tokamak is an important requirement for the validity of these variational techniques. However, this does not guarantee that the models will be successful in predicting equilibria for shaped tokamaks. Therefore, to assess this concern, we will compare ePFC and NEQ results for the case of the resistive-magnet tokamak reactor base design discussed in the previous chapter. This configuration should provide a good test for the variational method since, as

Table 3.3: *ePFC and NEQ Results for Conventional Tokamak Case*

Parameter	ePFC	NEQ
β_t	4.94×10^{-4}	5.03×10^{-4}
$\beta_{t,max}$	1.24×10^{-3}	1.23×10^{-3}
β_p	1.03	1.05
$q(0)$	9.28	9.05
q_a	18.0	18.2
ψ_0 (Wb)	-5.00×10^{-4}	-4.98×10^{-4}
σ	0.20	0.19
R_m (m)	0.426	0.425
κ_0	1.04	1.06
Cray CPU Time (sec)	0.03	31.0

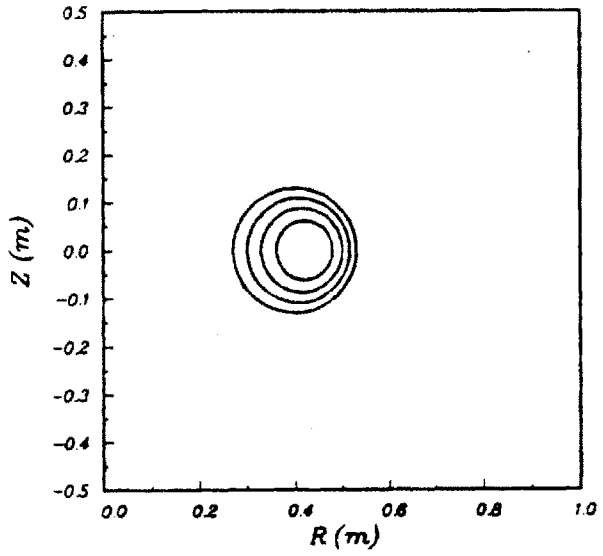

Figure 3.4: *Comparison of flux surface shapes computed by ePFC (dotted lines) and NEQ (solid lines) for conventional tokamak case.*

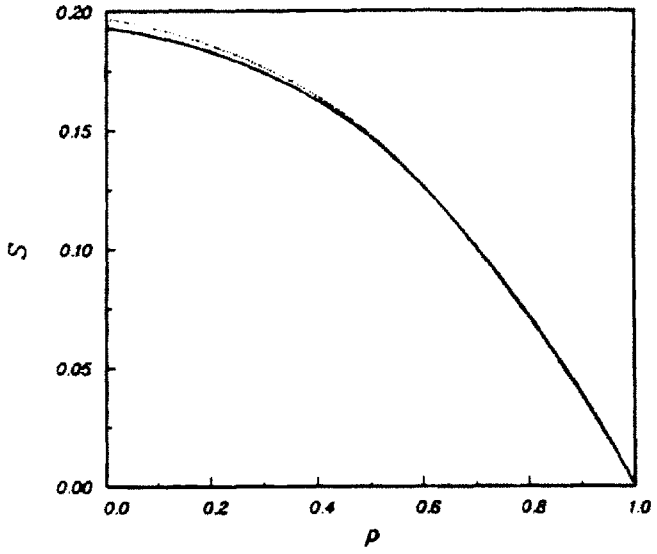

Figure 3.5: *Plot of relative flux surface shift vs. ρ as computed by ePFC (dotted lines) and NEQ (solid lines) for conventional tokamak case.*

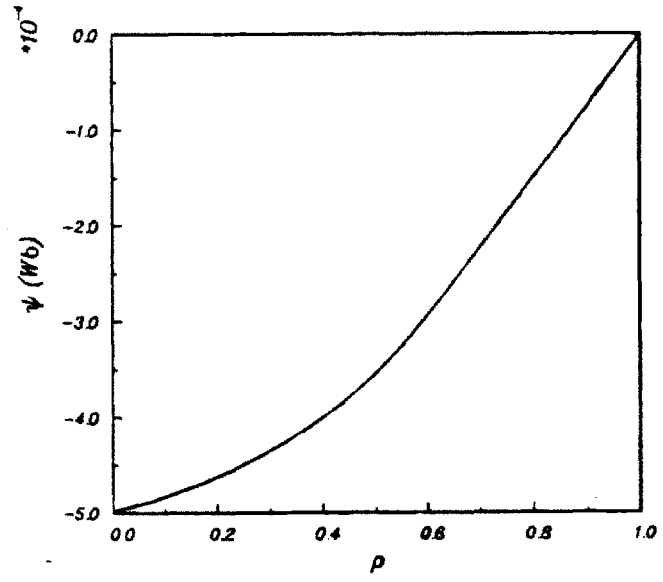

Figure 3.6: *Plot of flux function vs. ρ as computed by ePFC (dotted lines) and NEQ (solid lines) for conventional tokamak case.*

Table 3.4: *Input Parameters for Strongly Shaped Tokamak Case*

Parameter	Value
R_0 (m)	4.70
a (m)	1.70
ϵ	0.37
κ_a	2.00
δ_a	0.40
B_0 (T)	4.5
α_p	-3.32
α_f	-3.32
I_p (MA)	19.0
b_p	0.8

Table 3.4 shows, it is characterized by tight aspect ratio, peaked profiles, high elongation, high triangularity, and high beta.

A comparison of the output parameters from ePFC and NEQ [Table 3.5] again shows that, for the most part, the codes are in relatively good agreement. This is also confirmed by Figs. 3.7–3.11: Fig. 3.7 displays the flux surface shapes calculated by the two codes, Fig. 3.8 shows the radial variation of flux surface elongation

$$E \equiv \frac{2Z_{max}}{R_{outer} - R_{inner}} \tag{3.61}$$

Fig. 3.9 shows the radial variation of flux surface triangularity

$$T \equiv \frac{R_{inner} + R_{outer} - 2R_{max}}{R_{outer} - R_{inner}} \tag{3.62}$$

Fig. 3.10 shows the radial variation in the relative flux surface shape, and Fig. 3.11 shows the radial variation of the flux function. In the above formulae, (R_{max}, Z_{max}) is the location of the point on a particular flux surface that is farthest away from the plasma midplane.

The only result from the two codes that disagrees by any significant amount is the MHD safety factor at the plasma surface. The value calculated by ePFC is lower than that calculated by NEQ by approximately 10 %. This disagreement can be traced to inaccuracies in the poloidal field as calculated by the variational techniques. Specifically, Fig. 3.12 shows that the B_R is over-estimated in the region around $\mu = \pm\frac{\pi}{2}$ (i.e., the area around the tips of the dee). B_Z, on the other hand, is calculated quite well everywhere. Thus, the variational principle predicts a larger B_p than is correct. Since $q_s \sim \int \frac{d\ell}{B_p}$ emphasizes the regions where the field is small, this inaccuracy affects the MHD safety factor by a relatively large amount. However, the plasma current is calculated correctly since $I_p \sim \int B_p d\ell$ emphasizes the regions where the field is large.

This example points out a limitation in the current variational treatment. Namely, the poloidal field is calculated inaccurately in the region near a separatrix. This can be traced directly to the simple radial variation assumed for the trial functions. In particular, Eqs. (3.36)–(3.39) and Eq. (3.48) show that it is not possible for B_R to vanish at $\mu = \pm\frac{\pi}{2}$. Since this is exactly what is required when the separatrix moves close to the plasma, the error in B_p is not surprising. More elaborate trial functions would be required to accurately model the plasma edge in a vicinity of a separatrix. This could prove to be an interesting area for future research.

For many applications, the inaccuracy in B_p around the separatrix is not a major concern. Two such applications are the topics that will be discussed later in this thesis: the estimation of PF coil currents and the calculation of axisymmetric stability. It will be shown that the estimation of PF coil currents depends on the magnitude of B_p on the plasma surface. Since the equilibrium errors are in the region where the field is small, they affect the answers only marginally. In the case of the axisymmetric stability calculations presented here, the same result holds since all of the relevant integrals are of the form $\int B_p^2\, dS$. In any event, it should be emphasized that

Table 3.5: *ePFC and NEQ Results for Strongly Shaped Tokamak Case*

Parameter	ePFC	NEQ
β_t	0.082	0.083
$\beta_{t,max}$	0.224	0.222
β_p	0.805	0.830
$q(0)$	1.03	1.04
q_s	2.74	3.07
ψ_0 (Wb)	-9.29	-9.19
σ	0.149	0.142
R_m (m)	4.95	4.94
κ_0	1.69	1.79
Cray CPU Time (sec)	0.03	31.0

in the interior of the plasma the fields are calculated quite accurately. This contention is supported by the result (shown in Table 3.5) that the MHD safety factor at the magnetic axis as found by ePFC agrees well with the exact answer.

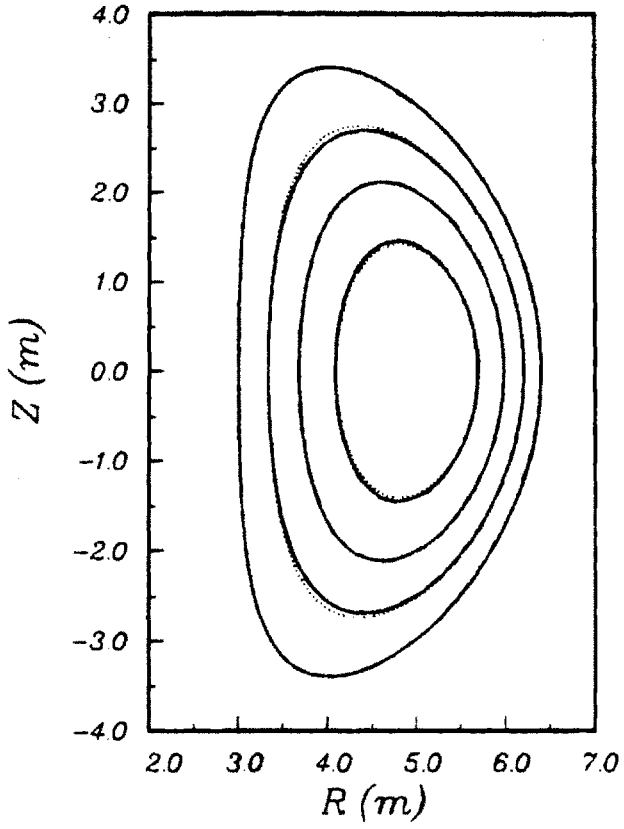

Figure 3.7: *Comparison of flux surface shapes computed by ePFC (dotted lines) and NEQ (solid lines) for strongly shaped tokamak case.*

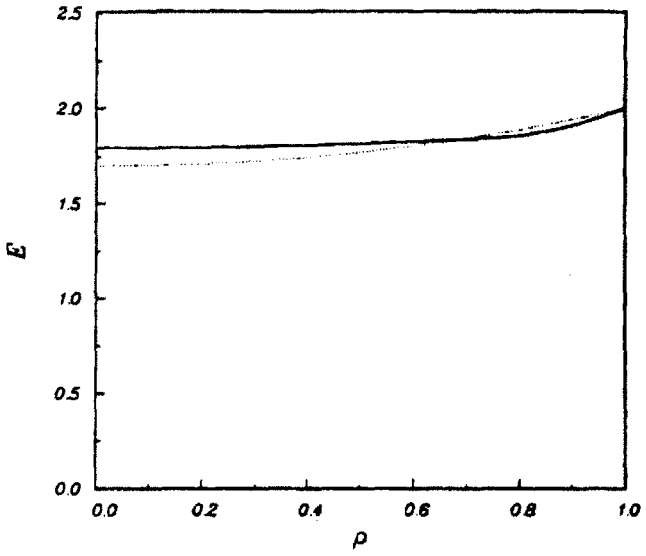

Figure 3.8: *Plot of flux surface elongation vs. ρ as computed by ePFC (dotted lines) and NEQ (solid lines) for strongly shaped tokamak case.*

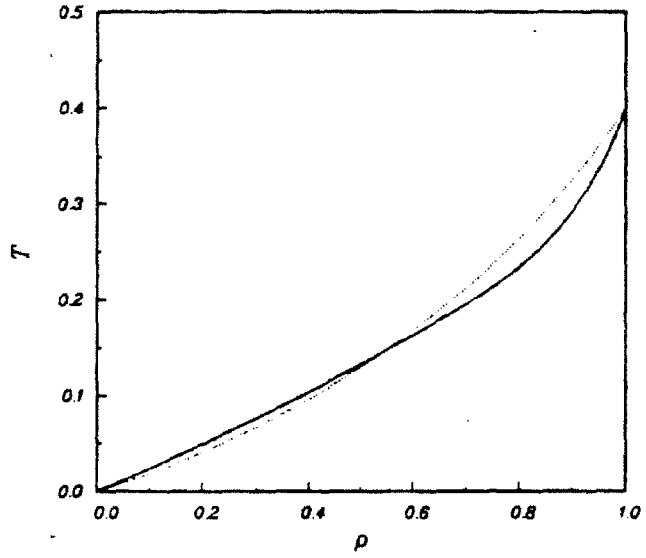

Figure 3.9: *Plot of flux surface triangularity vs. ρ as computed by ePFC (dotted lines) and NEQ (solid lines) for strongly shaped tokamak case.*

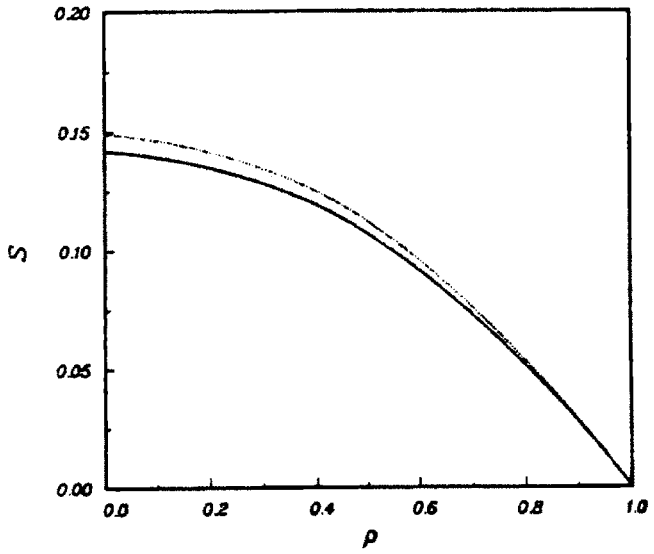

Figure 3.10: *Plot of relative flux surface shift vs. ρ as computed by ePFC (dotted lines) and NEQ (solid lines) for strongly shaped tokamak case.*

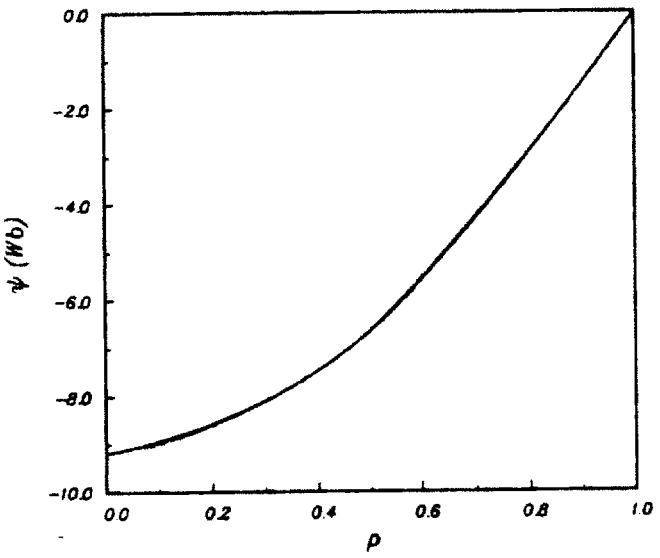

Figure 3.11: *Plot of flux function vs. ρ as computed by ePFC (dotted lines) and NEQ (solid lines) for strongly shaped tokamak case.*

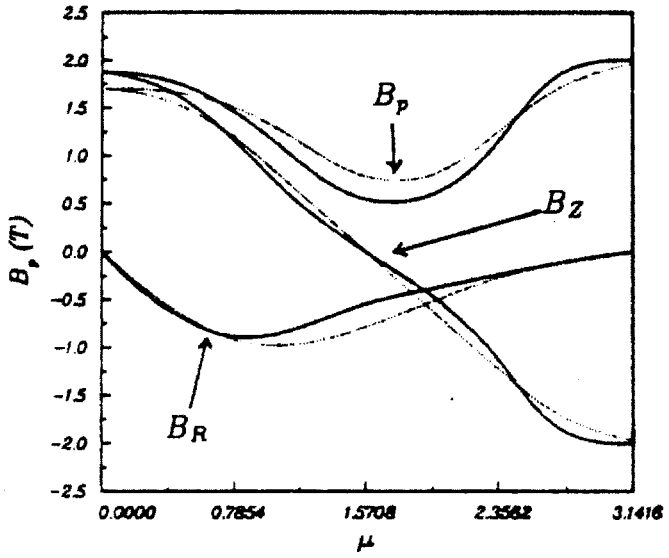

Figure 3.12: *Plot of B_R, B_Z, and B_p vs. μ as computed by ePFC (dotted lines) and NEQ (solid lines) for strongly shaped tokamak case.*

Chapter 4

Estimation of Poloidal Field Coil Currents

One of the major uses of equilibrium information is in the design of poloidal field (PF) systems. In this application, the plasma is assumed to be surrounded by a number of external conductors located in a vacuum region of infinite extent. Each of these conductors can represent a particular winding of PF coil or even an entire PF coil. The goal of the analysis is to calculate the set of conductor currents needed to hold the plasma in equilibrium.

To compute the conductor currents exactly requires the self-consistent solution of Maxwell's equations for the magnetic fields in the plasma and in the surrounding vacuum. The plasma field may be obtained by solving the Grad-Shafranov equation and the vacuum field may be obtained by solving Laplace's equation. The two solutions are then connected through a series of boundary conditions applied at the plasma surface. Since we will assume that the plasma current and pressure both vanish smoothly at the plasma edge, the exact boundary conditions are simply that the normal and tangential components of the fields must be continuous across the plasma-vacuum interface.

When the plasma shape is fixed and the conductors are placed in fixed locations, it is not generally possible to find a finite set of conductor currents which yield self-consistent solutions satisfying both the governing equations and the boundary conditions. This is because a finite set of conductor currents is insufficient to ensure that both boundary conditions are satisfied at an infinite number of points along the plasma surface. Hence, it is necessary to introduce another degree of freedom into the problem. The usual way of accomplishing this is to allow the plasma shape to vary along with the conductor currents. Since the plasma surface can move, this calculation is often called the "free boundary" equilibrium problem.

The major advantage of the free boundary method is that it enables us to exactly and self-consistently solve for the plasma and vacuum fields and the conductor currents. The major disadvantage is that this procedure represents an extremely difficult and time-consuming numerical chore. In fact, much of the complexity and relative slowness of NEQ, GAEQ, and some versions of PEST is derived from the fact that these codes attempt to solve the free boundary equilibrium problem. Moreover, for many applications — most notably stability calculations — this added complexity is unnecessary since conductor current information is not required.

As in the previous chapter, it turns out that many of these difficulties can be circumvented if some accuracy in the solution for the conductor currents can be sacrificed. In particular, it is advantageous to give up the notion of exact self-consistency by assuming that the plasma boundary is fixed. The major implication of this assumption is that it is usually not possible to find a set of conductor currents that result in the tangential component of the magnetic field being continuous across the plasma surface. Nevertheless, for any configuration of conductors, there will generally exist a set of currents that *minimizes* the jump in the tangential component of the field, at least in an integral sense. In many cases, these conductor currents are quite close to those that would have been found by a full free boundary calculation.

In this chapter, we will describe a procedure for estimating the PF coil currents in the above manner. A large part of this procedure consists of an involved, but relatively straightforward, calculation of the tangential component of the vacuum magnetic field at the plasma surface. Specifically, Green's theorem will be used to derive an integral equation for the scalar magnetic potential at the plasma surface. Then, using Fourier analysis, this integral equation will be transformed into an equivalent linear algebraic system that can be solved by standard matrix methods. Once computed, the scalar magnetic potential can be used to represent the tangential component of the vacuum magnetic field in terms of the unknown conductor currents which are then found by minimizing the jump in the tangential field across the plasma surface. The chapter will conclude with a discussion of the accuracy of these conductor currents particularly when they are calculated using plasma fields obtained from approximate equilibria such as those described in the previous chapter.

4.1 Problem Statement

Before proceeding to the details of the calculation, it will prove worthwhile to concisely state the problem in formal mathematical terms. This can be accomplished with the aid of Fig. 4.1. As the figure indicates, we assume the existence of a toroidally axisymmetric plasma, the surface of which is parameterized by the equations

$$R = R_p(\mu) \tag{4.1}$$

$$Z = Z_p(\mu), \tag{4.2}$$

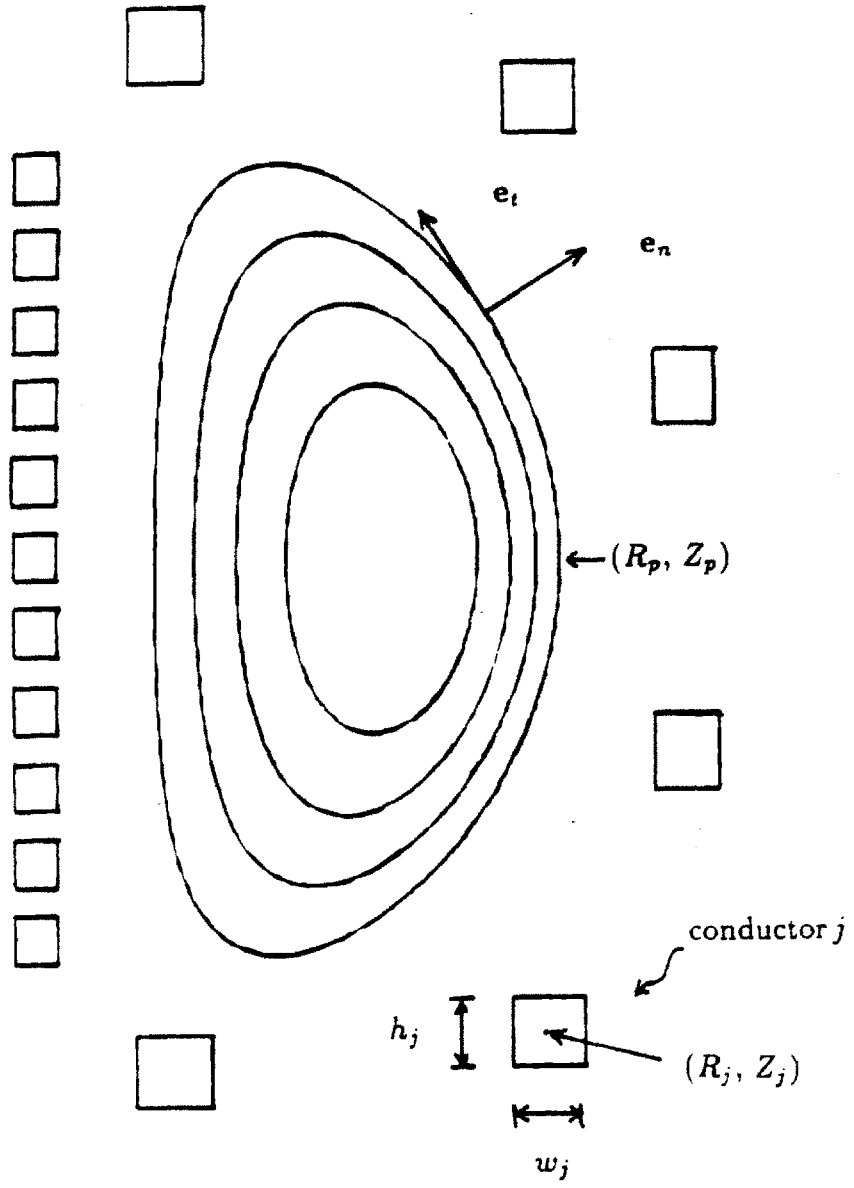

Figure 4.1: *Plasma/Conductor geometry for PF coil current calculation.*

where μ is an angular coordinate. R_p and Z_p may, for instance, be specified by Eqs. (3.34) and (3.35). However, this is not necessary, and, in particular, the calculation does not assume an up-down symmetric plasma.

On the basis of the above parameterization we can define a number of useful quantities including the outward facing unit normal vector,

$$\mathbf{e}_n = \frac{1}{Q}[Z_\mu \mathbf{e}_R - R_\mu \mathbf{e}_Z], \tag{4.3}$$

and the unit tangent vector,

$$\mathbf{e}_t = \frac{1}{Q}[R_\mu \mathbf{e}_R + Z_\mu \mathbf{e}_Z], \tag{4.4}$$

where $\mathbf{e}_R$ and $\mathbf{e}_Z$ are the unit vectors in the R and Z coordinate directions and

$$Q \equiv \sqrt{R_\mu^2 + Z_\mu^2}. \tag{4.5}$$

Using the definitions of the unit vectors, the operators expressing differentiation normal and tangent to the plasma surface can be written as follows:

$$Q\mathbf{e}_n \cdot \nabla \equiv \frac{\partial}{\partial n} = Z_\mu \frac{\partial}{\partial R} - R_\mu \frac{\partial}{\partial Z}, \tag{4.6}$$

$$Q\mathbf{e}_t \cdot \nabla \equiv \frac{\partial}{\partial \mu} = R_\mu \frac{\partial}{\partial R} + Z_\mu \frac{\partial}{\partial Z}. \tag{4.7}$$

Finally, we can write the incremental arc length in the form

$$d\ell = Q\, d\mu \tag{4.8}$$

and the differential surface area element as

$$dS = R\, d\ell d\varphi = RQ d\mu d\varphi. \tag{4.9}$$

The plasma is assumed to be completely surrounded by vacuum. Furthermore, in this vacuum region are suspended J external conductors located at the points $(R_j,\ Z_j)$. Like the plasma, these conductors are toroidally axisymmetric. For the purpose of calculating fields, these conductors are assumed to be infinitely thin filaments. However, in order to calculate the resistance, it is necessary to assume that the cross-section of each conductor is a rectangle of width w_j and height h_j where $w_j \ll R_j$ and $h_j \ll R_j$. The overall goal of the analysis is to estimate the set of currents I_j flowing through these conductors.

For purpose of calculating the conductor currents, all that is needed are the plasma and vacuum fields at the surface of the plasma. Inside the plasma, the field $\mathbf{B}$ is calculated from the flux function ψ which, in turn, is found by solving the Grad-Shafranov equation using methods such as those described in the previous chapter. In the vacuum region, the field is written

$$\hat{\mathbf{B}} = \tilde{\mathbf{B}} + \mathbf{B}_c, \tag{4.10}$$

where $\tilde{\mathbf{B}}$ is the induced field due to the plasma and $\mathbf{B}_c$ is the applied field due to the external conductors.

The induced field satisfies

$$\nabla \cdot \tilde{\mathbf{B}} = 0, \tag{4.11}$$

$$\nabla \times \tilde{\mathbf{B}} = 0 \tag{4.12}$$

and is required to remain regular everywhere throughout the vacuum. Hence, $\tilde{\mathbf{B}}$ can be written

$$\tilde{\mathbf{B}} = \nabla\phi + \mathbf{B}_i, \tag{4.13}$$

where, by virtue of Eqs. (4.11) and (4.12), ϕ is the scalar magnetic potential which, of course, satisfies Laplace's equation

$$\nabla^2\phi = 0. \tag{4.14}$$

Later, we will solve for ϕ using Fourier analysis so it is desirable that ϕ be single-valued. This necessitates the introduction of the additional field $\mathbf{B}_i$ so as to ensure that an application of Ampere's law around the plasma boundary correctly yields the plasma current. There is no unique requirement for choosing $\mathbf{B}_i$; the field produced by any set of currents, distributed or discrete, can be used as long as the total current is given by I_p. For the sake of convenience, we will simply choose $\mathbf{B}_i$ as the field produced by a single filament carrying a current I_p located at the plasma magnetic axis (R_m, Z_m). Then, using a classic result from magnetostatics, we can write

$$\mathbf{B}_i = \mu_0 I_p \frac{\nabla\Psi_P \times \mathbf{e}_\varphi}{R}, \tag{4.15}$$

where

$$\Psi_P = \frac{(RR_m)^{1/2}}{2\pi}\left[\frac{(2-k_p^2)K(k_P) - 2E(k_P)}{k_P}\right], \tag{4.16}$$

K and E are the complete elliptic integrals, and

$$k_P^2 = \frac{4RR_m}{(R+R_m)^2 + (Z-Z_m)^2}. \tag{4.17}$$

The applied field is found in a similar manner since the conductors are assumed to be thin and the fields are to be calculated at points far away compared to the spatial dimensions of the conductors:

$$\mathbf{B}_c = \sum_{j=1}^{J} \mu_0 I_j \frac{\nabla\Psi_j \times \mathbf{e}_\varphi}{R}, \tag{4.18}$$

where

$$\Psi_j = \frac{(RR_j)^{1/2}}{2\pi}\left[\frac{(2-k_j^2)K(k_j)-2E(k_j)}{k_j}\right], \tag{4.19}$$

and

$$k_j^2 = \frac{4RR_j}{(R+R_j)^2+(Z-Z_j)^2}. \tag{4.20}$$

As a consequence of the MHD model, the plasma is assumed to have infinite electrical conductivity. Therefore, the component of the magnetic field normal to the plasma surface is required to vanish both inside and just outside the plasma:

$$\mathbf{e}_n \cdot \mathbf{B} \mid_{S_p} = \mathbf{e}_n \cdot \hat{\mathbf{B}} \mid_{S_p} = 0. \tag{4.21}$$

The solutions to the Grad-Shafranov equation naturally possess this property (i.e., on the plasma surface $B = B_p(\mu)$). However, in the case of the vacuum solutions, it is necessary to apply Eq. (4.21) as an explicit constraint.

In the section to follow, it will be shown that this will allow us to write the (purely poloidal) vacuum field at the plasma surface in the form

$$\hat{B}_p(\mu) = b^{(1)}(\mu) + \mathbf{b}^{(2)}(\mu) \cdot \mathbf{i}, \tag{4.22}$$

where $\mathbf{i}$ and $\mathbf{b}^{(2)}$ are column vectors of length J whose elements are the set conductor currents I_j and the set of geometrical coefficients $b_j^{(2)}$ respectively. In the full free boundary calculation, it is necessary to vary $b^{(1)}$ and the $b_j^{(2)}$ by moving the plasma surface in order to find a set of conductor currents that result in the boundary condition

$$B_p = \hat{B}_p \text{ on } S_p \tag{4.23}$$

being satisfied. However, in this analysis, the plasma surface will remain fixed and Eq. (4.23) will be discarded. Instead, we will choose the I_j so as to minimize the functional

$$\epsilon_I(\mathbf{i}) \equiv \frac{\int_{S_p}(\hat{B}_p - B_p)^2\, dS}{\int_{S_p} B_p^2\, dS}. \tag{4.24}$$

This is not the only choice for ϵ_I that could be made. In particular, other analyses [45,57] have minimized a functional of the form

$$\epsilon_I(\mathbf{i}) = \sum_{n=1}^{N}\left[c_1(\hat{\psi}-\psi)_n^2 + c_2\left(\frac{\partial\hat{\psi}}{\partial n} - \frac{\partial\psi}{\partial n}\right)_n^2\right] + c_3\sum_{j=1}^{J} I_j^2, \tag{4.25}$$

where c_1, c_2, and c_3 are weight coefficients and the index n corresponds to evaluating the various quantities at a series of points around the plasma surface. Equation (4.25) is equivalent to minimizing the jump in both the normal and tangential field across the plasma surface subject to a conductor current smoothing constraint.

However, Eq. (4.24) has a few very desirable features. First, the normal component of the field is made to exactly vanish. This is desirable since the plasma is assumed to be a perfect conductor. Second, the minimization of ϵ_I in Eq. (4.24) has a tangible physical meaning. Namely, it is equivalent to minimizing the net deviation from exact radial pressure balance around the plasma boundary. Third, the form of ϵ_I makes it quite simple to determine the optimal set of conductor currents. In a later section, it will be shown that this can be accomplished by simply solving a small set of linear equations. Finally, the results are not dependent on a set of relatively arbitrary weighting coefficients. The variation of n, c_1, c_2, and c_3 in Eq. (4.25) can lead to a correspondingly large variation in the resulting conductor currents, even without changing the plasma shape or B_p.

4.2 Calculation of Vacuum Field

The procedure for determining the vacuum field will be based on an application of the scalar version of Green's theorem [15]. This is a natural choice since the field must be calculated only on the plasma surface. Also, a number of analyses [58–61] have demonstrated that the Green's theorem formalism lends itself quite well to fast numerical computation.

Green's theorem for the scalar magnetic potential is written in the classic form

$$\sigma\phi(\mathbf{r}) \;+\; \int_{S_p} \Big[\phi(\mathbf{r}')(\mathbf{e}'_n \cdot \nabla'\hat{G}(\mathbf{r},\mathbf{r}')) - \hat{G}(\mathbf{r},\mathbf{r}')(\mathbf{e}'_n \cdot \nabla'\phi(\mathbf{r}'))\Big]\, dS' = 0. \tag{4.26}$$

Here, $\mathbf{r}' \equiv (R',\, \varphi',\, Z')$ and $\mathbf{r} \equiv (R,\, \varphi,\, Z)$ where, to simplify the notation, we write $R' = R_p(\mu')$ and $Z' = Z_p(\mu')$. $\mathbf{r}$ denotes the observation point while the primed coordinates represent integration variables. Also, $\hat{G}$ is the infinite space Green's function

$$\hat{G}(\mathbf{r},\mathbf{r}') = -\frac{1}{4\pi|\mathbf{r}' - \mathbf{r}|}, \tag{4.27}$$

where

$$|\mathbf{r}' - \mathbf{r}| = \left[R^2 + R'^2 - 2RR'\cos(\varphi' - \varphi) + (Z' - Z)^2\right]^{1/2}. \tag{4.28}$$

Finally, σ is a quantity that depends on the location of the observation point in relation to the plasma surface

$$\sigma = \begin{cases} 1 & \text{if } \mathbf{r} \text{ outside plasma,} \\ 1/2 & \text{if } \mathbf{r} \text{ on } S_p, \\ 0 & \text{if } \mathbf{r} \text{ inside plasma.} \end{cases} \tag{4.29}$$

Since the goal of the analysis is to find ϕ on the plasma surface, we choose $\sigma = 1/2$ and accordingly $R = R_p(\mu)$ and $Z = Z_p(\mu)$. The rest of this section will be largely concerned with the efficient solution of Eq. (4.26).

4.2.1 Simplification of Green's Theorem

Green's theorem can be dramatically simplified by invoking the assumption of toroidal axisymmetry. Then, the φ-dependence of the infinite space Green's function can be analytically integrated. A short calculation yields

$$\frac{1}{2}\phi(\mu) + \int_0^{2\pi} \left[\phi(\mu') \frac{\partial G}{\partial n'}(\mu, \mu') - G(\mu, \mu') \frac{\partial \phi}{\partial n'}(\mu') \right] R' d\mu' = 0, \qquad (4.30)$$

where Eq. (4.6) has been used to simplify the notation and G is the reduced Green's function defined by

$$G = \int_0^{2\pi} \hat{G}\, d\varphi'. \qquad (4.31)$$

Upon performing the integration in Eq. (4.31), we find

$$G = -\frac{kK(k)}{2\pi(RR')^{1/2}}, \qquad (4.32)$$

where

$$k^2 = \frac{4RR'}{(R'+R)^2 + (Z'-Z)^2}. \qquad (4.33)$$

In order to solve Eq. (4.30), it is necessary to specify the normal derivatives of G and ϕ. Using the identities [62],

$$\frac{dE}{dk} = \frac{E(k) - K(k)}{k}, \qquad (4.34)$$

$$\frac{dK}{dk} = \frac{E(k)}{k(1-k^2)} - \frac{K(k)}{k}, \qquad (4.35)$$

along with Eqs. (4.6) and (4.32) gives

$$R'\frac{\partial G}{\partial n'} = \frac{1}{2\pi}\left(\frac{R'}{R}\right)^{1/2}[\Lambda k E(k) + \Gamma k(K(k) - E(k))], \tag{4.36}$$

where

$$\Lambda = \frac{Z'_\mu(R' - R) - R'_\mu(Z' - Z)}{(R' - R)^2 + (Z' - Z)^2}, \tag{4.37}$$

$$\Gamma = \frac{Z'_\mu}{2R'}. \tag{4.38}$$

The boundary condition on the normal component of $\hat{\mathbf{B}}$ can be used to write the normal derivative of ϕ in a very convenient form. Specifically, using Eqs. (4.15) and (4.18) along with Eq. (4.10) in Eq. (4.21) gives

$$R'\frac{\partial \phi}{\partial n'} = \frac{\partial}{\partial \mu'}\left(\mu_0 I_p \Psi_P + \sum_{j=1}^{J} \mu_0 I_j \Psi_j\right). \tag{4.39}$$

It should be noted that this constraint can be applied for arbitrary plasma shapes and conductor configurations. In other words, it is always possible to ensure that the normal component of the vacuum field exactly vanishes at the surface of the plasma.

4.2.2 Conductor Grouping

In many applications, several of the J conductors will be constrained to carry the same current or will have their currents fixed at values set from external considerations. As a result, the number of conductor currents that must be calculated is often significantly less than J. Accounting for these cases now can therefore save a significant amount of computation.

In general, a set of conductors can be constrained to carry the same current for one of two reasons. First, the conductors can be located in such

a manner that symmetry demands that they carry the same current. This usually occurs in the case of up-down symmetric plasmas where conductors are placed in symmetric positions above and below the plasma midplane. Second, the conductors can be electrically connected in series. This is the case for conductors that represent individual windings of a particular PF coil and for conductors that are considered part of the ohmic stack.

Conductor currents can be fixed at set values for a number of reasons. One example of particular interest is start-up. Here, it is often the case that the currents in an ohmic stack are programmed to follow a pre-defined evolution in order to optimize volt-second consumption. In order to calculate the currents needed in shaping coils at various times during a shot, the currents in the conductors representing the ohmic stack would be fixed at their programmed values for a given time and the currents in the shaping coils would be allowed to vary.

Mathematically, the notion of grouping is very easy to implement. In particular, we assume that the currents in F conductors, where $F \leq J$, will be fixed at prescribed values. Then, the rest of the conductors are assumed to be members of G groups of conductors with each conductor in each group being constrained to carry the same current I_g. It is these G currents that are actually solved for. Based on this discussion, we can write the vacuum field in the form

$$\hat{\mathbf{B}} = \nabla\phi + \mu_0 I_p \frac{\nabla\Psi_F \times \mathbf{e}_\varphi}{R} + \sum_{g=1}^{G} \mu_0 I_g \frac{\nabla\Psi_g \times \mathbf{e}_\varphi}{R}, \tag{4.40}$$

where

$$\Psi_F = \Psi_P + \frac{1}{\mu_0 I_P} \sum_{j=1}^{J} \mu_0 I_j \delta_j^{(F)} \Psi_j, \tag{4.41}$$

and

$$\Psi_g = \sum_{j=1}^{J} \delta_j^{(g)} \Psi_j. \tag{4.42}$$

Ψ_F accounts for the toroidal flux from the conductors with fixed currents and the filament representing the plasma current. Ψ_g accounts for the total toroidal flux from the *g-th* group of conductors. The functions $\delta_j^{(F)}$ and $\delta_j^{(g)}$ which are defined

$$\delta_j^{(F)} = \begin{cases} 1 & \text{if } I_j \text{ is a fixed current,} \\ 0 & \text{otherwise,} \end{cases} \tag{4.43}$$

$$\delta_j^{(g)} = \begin{cases} 1 & \text{if conductor } j \text{ is in group } g, \\ 0 & \text{otherwise,} \end{cases} \tag{4.44}$$

simply select the fixed-current conductors and grouped conductors out of the complete set of conductors.

Based on Eq. (4.40), the normal derivative of ϕ in Eq. (4.39) takes the form

$$R' \frac{\partial \phi}{\partial n'} = \frac{\partial}{\partial \mu'} \left(\mu_0 I_p \Psi_F + \sum_{g=1}^{G} \mu_0 I_g \Psi_g \right). \tag{4.45}$$

4.2.3 Fourier Analysis

The solution to Eq. (4.30) can be found by standard Fourier analysis techniques. This is accomplished by expanding ϕ and its normal derivative in Fourier series

$$\phi = \sum_{m=-M}^{M} a_m e^{im\mu}, \tag{4.46}$$

$$R \frac{\partial \phi}{\partial n} = \sum_{m=-M}^{M} \left(c_m + \sum_{g=1}^{G} D_{mg} I_g \right) e^{im\mu}. \tag{4.47}$$

In principle, the sum over m should extend over the range $-\infty < m < \infty$. However, practical considerations require that the sum be truncated after a finite number of terms given by $m = \pm M$.

The coefficients c_m and D_{mg} are assumed known. Using Eq. (4.45), they can be calculated as follows:

$$c_m = \frac{im}{2\pi} \int_0^{2\pi} \mu_0 I_p \Psi_F \, e^{-im\mu} \, d\mu, \tag{4.48}$$

$$D_{mg} = \frac{im}{2\pi} \int_0^{2\pi} \mu_0 \Psi_g \, e^{-im\mu} \, d\mu. \tag{4.49}$$

The goal of the Fourier analysis is to solve for the coefficients a_m. This can be accomplished by substituting the expansions in Eqs. (4.46) and (4.47) into Eq. (4.30), multiplying by $e^{-im\mu}$, and integrating. A standard problem in matrix algebra results, namely

$$[\mathbf{I} + \mathbf{A}] \cdot \mathbf{a} = \mathbf{C} \cdot [\mathbf{c} + \mathbf{D} \cdot \mathbf{i}], \tag{4.50}$$

where $\mathbf{I}$ is the identity matrix and the elements of the matrices $\mathbf{A}$ and $\mathbf{C}$ are given by

$$A_{mm'} = \frac{1}{\pi} \int_0^{2\pi} \int_0^{2\pi} \left(R' \frac{\partial G}{\partial n'} \right) e^{im'\mu' - im\mu} \, d\mu \, d\mu', \tag{4.51}$$

$$C_{mm'} = -\frac{1}{\pi} \int_0^{2\pi} \int_0^{2\pi} G e^{im'\mu' - im\mu} \, d\mu \, d\mu'. \tag{4.52}$$

The ranges on m and m' are $-M \leq m \leq M$ and $-M \leq m' \leq M$ so $\mathbf{A}$ and $\mathbf{C}$ are of dimension $(2M+1) \times (2M+1)$.

Equation (4.50) can be solved numerically to yield

$$\mathbf{a} = \mathbf{d} + \mathbf{E} \cdot \mathbf{i}, \tag{4.53}$$

where

$$\mathbf{d} = [\mathbf{I} + \mathbf{A}]^{-1} \cdot \mathbf{C} \cdot \mathbf{c}, \tag{4.54}$$

$$\mathbf{E} = [\mathbf{I} + \mathbf{A}]^{-1} \cdot \mathbf{C} \cdot \mathbf{D}. \tag{4.55}$$

Equation (4.53) can, in turn, be used in Eq. (4.40) to write the tangential component of the vacuum field in the desired form

$$\hat{B}_p(\mu) = b^{(F)}(\mu) + \mathbf{b}^{(G)}(\mu) \cdot \mathbf{i}, \tag{4.56}$$

where $b^{(F)}(\mu)$ represents the contribution due to the conductors with fixed currents and $\mathbf{b}^{(G)}(\mu)$ represents the contribution due to the grouped conductors. These functions are written

$$b^{(F)}(\mu) = \frac{1}{Q}\left(\sum_{m=-M}^{M}(imd_m e^{im\mu}) + \mu_0 I_p \frac{1}{R}\frac{\partial \Psi_F}{\partial n}\right), \tag{4.57}$$

$$b_g^{(G)}(\mu) = \frac{1}{Q}\left(\sum_{m=-M}^{M}(imE_{mg} e^{im\mu}) + \mu_0 \frac{1}{R}\frac{\partial \Psi_g}{\partial n}\right). \tag{4.58}$$

4.2.4 Analytic Removal of Logarithmic Singularities

An important numerical issue associated with the solution of Eq. (4.30) concerns the evaluation of the matrix elements of **A** and **C**. In particular, the integrands of Eqs. (4.51) and (4.52) possess integrable logarithmic singularities when $\mu' = \mu$. Despite being integrable, these singularities must be dealt with specially because they lead to problems with numerical accuracy in the calculation of **A** and **C**.

The singularities can be traced to the first complete elliptic integral in the reduced Green's function [Eq. (4.31)]. This is seen by writing $\delta\mu = \mu' - \mu \ll 1$ and expanding R' and Z' about R and Z respectively:

$$R' = R + R_\mu \delta\mu + R_{\mu\mu}\frac{(\delta\mu)^2}{2} + \cdots, \tag{4.59}$$

$$Z' = Z + Z_\mu \delta\mu + Z_{\mu\mu} \frac{(\delta\mu)^2}{2} + \cdots \tag{4.60}$$

Substituting these expressions into the first complete elliptic integral yields [63]:

$$K \approx \frac{1}{2} \ln \frac{Q^2}{16R^2} + \frac{1}{2} \ln \frac{(\delta\mu)^2}{4}, \tag{4.61}$$

where Q is defined in Eq. (4.5). The first term in Eq. (4.61) is continuous but the second term clearly diverges in the vicinity of $\mu' = \mu$.

A simple way of dealing with the singularities is to modify the Green's function in such a way that the part of the integrand that diverges can be integrated analytically. By noting the asymptotic behavior of K illustrated in Eq. (4.61), we see that this can be accomplished by writing

$$G(\mu, \mu') = \tilde{G} + \frac{1}{4\pi R} \ln \sin^2 \left(\frac{\mu' - \mu}{2} \right), \tag{4.62}$$

$$R' \frac{\partial G}{\partial n'}(\mu, \mu') = R' \frac{\partial \tilde{G}}{\partial n'} - \frac{Z_\mu}{8\pi R} \ln \sin^2 \left(\frac{\mu' - \mu}{2} \right), \tag{4.63}$$

where

$$\tilde{G}(\mu, \mu') = G - \frac{1}{4\pi R} \ln \sin^2 \left(\frac{\mu' - \mu}{2} \right), \tag{4.64}$$

$$R' \frac{\partial \tilde{G}}{\partial n'}(\mu, \mu') = R' \frac{\partial G}{\partial n'} + \frac{Z_\mu}{8\pi R} \ln \sin^2 \left(\frac{\mu' - \mu}{2} \right). \tag{4.65}$$

Now, when $\mu' = \mu$, the logarithmic singularities cancel and each modified Green's function remains finite

$$\tilde{G}(\mu,\mu) = \frac{1}{4\pi R}\ln\frac{Q^2}{16R^2}, \tag{4.66}$$

$$R'\frac{\partial\tilde{G}}{\partial n'}(\mu,\mu) = \frac{1}{4\pi}\left[\frac{R_\mu Z_{\mu\mu} - Z_\mu Z_{\mu\mu}}{Q^2} - \frac{Z_\mu}{2R}\left(2+\ln\frac{Q^2}{16R^2}\right)\right]. \tag{4.67}$$

Using these relations, the elements of **A** and **C** can be written

$$\begin{aligned} A_{mm'} &= \frac{1}{\pi}\int_0^{2\pi}\int_0^{2\pi}\left(R'\frac{\partial\tilde{G}}{\partial n'}\right)e^{im'\mu'-im\mu}\,d\mu\,d\mu' - \\ &\quad \frac{F_{m'}}{2\pi}\int_0^{2\pi}\frac{Z_\mu}{R}e^{i(m'-m)\mu}d\mu, \end{aligned} \tag{4.68}$$

$$\begin{aligned} C_{mm'} &= \frac{1}{\pi}\int_0^{2\pi}\int_0^{2\pi}\tilde{G}e^{im'\mu'-im\mu}\,d\mu\,d\mu' - \\ &\quad \frac{F_{m'}}{\pi}\int_0^{2\pi}\frac{1}{R}e^{i(m'-m)\mu}d\mu, \end{aligned} \tag{4.69}$$

where

$$F_{m'} = \frac{1}{4\pi}\int_0^{2\pi}\ln\sin^2\left(\frac{\mu'-\mu}{2}\right)e^{im'(\mu'-\mu)}d\mu' \tag{4.70}$$

can be integrated analytically to yield

$$F_{m'} = \begin{cases} -\ln 2 & m'=0, \\ -\frac{1}{2|m'|} & m'\neq 0. \end{cases} \tag{4.71}$$

In the above form **A** and **C** can be computed straightforwardly since the integrands remain finite for all values of μ and μ'.

4.3 Solution for Group Currents

The end result of the rather involved calculation of the previous section is given by Eq. (4.56). Here, $\hat{B}_p$ is written in terms of the purely geometrical quantities $b^{(F)}(\mu)$ and $\mathbf{b}^{(G)}(\mu)$ and the conductor currents. When this expression is substituted into Eq. (4.24), we obtain

$$\epsilon_I(\mathbf{i}) = \mathbf{i} \cdot \mathbf{M} \cdot \mathbf{i} - 2\mathbf{n} \cdot \mathbf{i} + p, \tag{4.72}$$

where $\mathbf{M}$ is a $(G \times G)$ symmetric matrix, $\mathbf{n}$ is a column vector of length G, and p is a scalar. These quantities are defined

$$M_{gg'} = \frac{\int_0^{2\pi} RQ b_g^{(G)} b_{g'}^{(G)}\, d\mu}{\int_0^{2\pi} RQ B_p^2\, d\mu}, \tag{4.73}$$

$$n_g = \frac{\int_0^{2\pi} RQ b_g^{(G)} (B_p - b^{(F)})\, d\mu}{\int_0^{2\pi} RQ B_p^2\, d\mu}, \tag{4.74}$$

$$p = \frac{\int_0^{2\pi} RQ (B_p - b^{(F)})^2\, d\mu}{\int_0^{2\pi} RQ B_p^2\, d\mu}. \tag{4.75}$$

We can minimize the field jump with respect to the group currents by formally taking derivatives and setting them to zero

$$\frac{\partial \epsilon_I}{\partial I_g} = 0, \qquad g = 1, \ldots, G. \tag{4.76}$$

Since Eq. (4.72) represents a quadratic form, the relations in Eq. (4.76) reduce to a simple linear system

$$\mathbf{M} \cdot \mathbf{i} = \mathbf{n} \tag{4.77}$$

that can be solved for the group currents using standard matrix techniques [64]. Since $G \approx 4 - 10$ for typical tokamak configurations, Eq. (4.77) represents a trivial numerical task for modern day computers. Finally, it should be noted that the entire calculation can be accomplished without any iteration or searching. These factors suggest that a numerical implementation of this procedure will be extremely fast and robust.

One additional desirable feature of Eq. (4.72) is that various constraints on the group currents can be introduced quite naturally. These constraints can result from a number of different factors. For instance, if a tokamak possesses an iron core transformer, the high permittivity of iron requires that the sum of the conductor currents and the plasma current equal zero. As another example, it is sometimes the case that power supply limitations require that some conductor group currents be proportional to others. Finally, there are often volt-second requirements that set the flux that a certain group of currents must produce at a given point. All of these constraints can be written in the form

$$\mathbf{U} \cdot \mathbf{i} = \mathbf{y}. \tag{4.78}$$

Since Eq. (4.72) represents a quadratic form, standard numerical methods [65,66] can be used to minimize ϵ_I subject to Eq. (4.78) without the need for iteration.

Once the optimal set of group currents $\mathbf{i}_{opt}$ is found, they can be be used to compute a number of important quantities. Two of the most important of these are the the average tangential field error b_e and the total PF dissipated power P_{PF} which are defined

$$b_e = \sqrt{\epsilon_I(\mathbf{i}_{opt})}, \tag{4.79}$$

$$P_{PF} = \sum_{j=1}^{J} r_j I_{j,opt}^2, \tag{4.80}$$

where r_j is the resistance of the j–th conductor defined

$$\frac{1}{r_j} = \frac{h_j \sigma_j}{2\pi} \ln\left(\frac{R_j + \frac{1}{2}w_j}{R_j - \frac{1}{2}w_j}\right) \tag{4.81}$$

and σ_j is the resistivity of the material making up the j–th conductor.

4.4 Solution Procedure Summary

The calculations described in this chapter are fairly involved. However, they can be summarized relatively simply. The solution procedure assumes that the following information is known:

- Equilibrium Information:
  1. The plasma shape,
  2. The total plasma current,
  3. The tangential component of the magnetic field on the plasma surface B_p.
- Conductor Information:
  1. The locations of J conductors surrounding the plasma,
  2. Possibly, the currents in F of the J conductors (i.e., the conductors with fixed currents),
  3. Possibly, the symmetry or electrical characteristics of some of the conductors (i.e., the grouped conductors) that would cause them to carry the same current.

These are the only inputs required by the solution procedure. The output of the procedure consists solely of G estimates for the group conductor currents. The group currents are calculated as follows. The plasma shape information is used to compute the matrices $\mathbf{A}$ and $\mathbf{C}$ using Eqs. (4.68) and (4.69). The plasma shape information and conductor locations are used to compute $\mathbf{c}$ and $\mathbf{D}$ using Eqs. (4.48) and (4.49). These matrices can, in turn, be used to compute $\hat{B}_p$. This along with B_p can be substituted into Eqs. (4.73)–(4.75) to compute $\mathbf{M}$ and $\mathbf{n}$. The group currents are then found by solving the small set of linear equations given Eq. (4.77).

4.5 Computer Implementation

The ideas of the previous sections have been implemented in a computer program called "cPFC." This code, written in the C programming language, currently can find an estimate for the PF currents for a typical up-down symmetric tokamak configuration ($J \approx 20$) in 0.5–1.0 sec of Cray CPU time. In this section, we will discuss three numerical issues relating to this code: the use of fast Fourier transform (FFT) techniques to improve performance, the verification of the code's correctness, and the interpretation of the field error b_e.

4.5.1 FFT Techniques

To a large extent, the relatively fast execution time is owed to the fact that the integrals needed to find the matrix elements of $\mathbf{A}$, $\mathbf{C}$, $\mathbf{c}$ and $\mathbf{D}$ can be expressed in terms of discrete Fourier transforms. To see this, consider the numerical calculation of the elements of $\mathbf{c}$. When the interval $0 \leq \mu < 2\pi$ is discretized into N equally spaced subintervals, the trapezoidal rule can be used to rewrite Eq. (4.48) in the form

$$c_m = \frac{im}{N} \sum_{n=0}^{N-1} \mu_0 I_p \, \Psi_F(2\pi n/N) \, e^{-2\pi i m n/N} \tag{4.82}$$

which is seen to be proportional to the discrete inverse Fourier transform of Ψ_F. The matrix elements for $\mathbf{A}$ and $\mathbf{C}$ can be similarly expressed. The only difference is that the transforms in those cases are two-dimensional. For this application, the trapezoidal rule gives very accurate estimates of the integrals because the integrands are continuous and periodic. Recall that for for many of the integrals, the continuity of the integrands was ensured by analytically removing various logarithmic singularities.

Discrete Fourier transforms can be numerically computed extremely efficiently using FFT techniques [67]. These techniques make use of the periodicity of the circular functions to reduce the number of operations required to calculate a set of Fourier coefficients from $O(N^2)$ to $O(N \log_2 N)$. In this calculation, we take $N = 32$ so, especially for the two-dimensional transforms, the savings are enormous. Note that our choice for N requires us to truncate the Fourier series [Eqs. (4.46) and (4.47)] at $M = 16$ to be consistent with the Nyquist sampling theorem [67]. However, experience has shown that this number of harmonics is sufficient to represent the fields of interest.

4.5.2 Code Verification

Of obvious importance in any numerical calculation, especially one as involved as this one, is the verification of the correctness of the computer models employed. In general, this is extremely difficult, if not impossible, to prove rigorously. However, here, we will present two pieces of evidence that seem to compellingly indicate that cPFC is functioning properly.

As the first test of the code, we consider the symmetry properties of the matrix factor

$$\mathbf{S} \equiv [\mathbf{I} + \mathbf{A}]^{-1} \cdot \mathbf{C} \tag{4.83}$$

that appears in Eqs. (4.54) and (4.55). In general, both **A** and **C** are non-symmetric matrices. Despite this, it has been proven [59] that **S** is a *symmetric* matrix in the limit $M \longrightarrow \infty$! In practice, **S** is not expected to be exactly symmetric because the Fourier sums are truncated at finite M. Nevertheless, this remarkable fact, which comes about because **S** is related to the magnetic energy of the system, can be used as a guide as to whether the matrix elements of **A** and **C** are being calculated correctly because those elements must be computed correctly in order for **S** to end up nearly symmetric. For a typical cPFC run, the asymmetry of **S** (given by $\max|S_{ij} - S_{ji}|/|\max(S_{ij})|$) is in the range 10^{-6}–10^{-4}. Experience has shown that computer coding errors associated with the calculation of **A** and **C** result in a matrix asymmetry for **S** on the order of 10^{-1}. Therefore, it appears that the matrix elements are indeed being computed correctly.

Clearly, the correct calculation of **A** and **C** is necessary in order to obtain correct conductor currents. However, this does not demonstrate that cPFC does, in fact, compute correct conductor currents. This fundamental issue will be addressed using the example problem depicted in Fig. 4.2. The figure shows a number of conducting filaments located at various places in a vacuum region. These filaments carry the specified currents given in Table 4.1. The filaments with the "Plasma" label collectively represent the current distribution of a 3.0 MA plasma. Similarly, the other filaments represent PF and OH coils respectively. When the fluxes due to all of these filaments are summed, they produce a number of closed surfaces, one of which is shown in Fig. 4.2. By summing the fields from all the conductors, it is clearly possible to calculate the purely tangential field on this flux surface.

With this background in mind we can now state the example problem as follows:

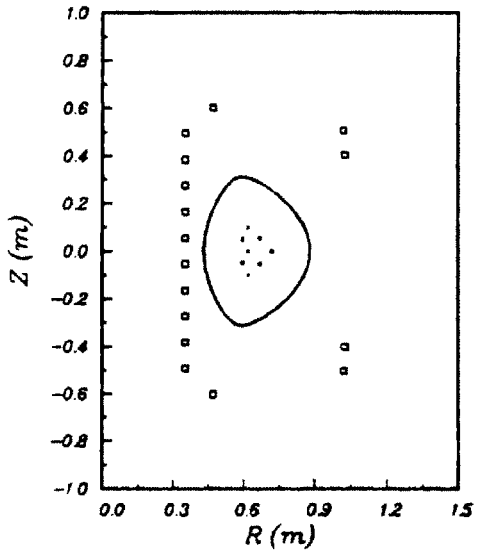

Figure 4.2: *Sample problem geometry for cPFC code verification.*

Table 4.1: *Input Filament Currents in cPFC Sample Problem*

Label	R (m)	Z (m)	Current (MA)
Plasma1	0.619	0.000	−1.0
Plasma2	0.719	0.000	−0.1
Plasma3	0.595	±0.050	−0.1
Plasma4	0.668	±0.055	−0.7
Plasma5	0.619	±0.101	−0.1
PF1	0.469	±0.604	−0.587
PF2	1.020	±0.506	+0.934
PF3	1.025	±0.403	+0.934
OH1	0.350	±0.055	+0.990
OH2	0.350	±0.165	+0.990
OH3	0.350	±0.274	+0.990
OH4	0.350	±0.384	+0.990
OH5	0.350	±0.494	+0.990

> Using only the known flux surface shape, the total enclosed current, and the tangential field on the surface, can the methods of this chapter — as implemented in the code cPFC — accurately reproduce the currents in the PF and OH coils that were originally used to generate the shape?

This would seem to represent a very good test of the code for a number of reasons. First, the problem geometry is realistic. The filament arrangement in Fig. 4.2 was devised to closely model a tokamak configuration, specifically that of Alcator C-Mod. Furthermore, the shape was deliberately chosen to be quite triangular in order to model the effect of a nearby separatrix. Second, the problem is basically quite simple. No complex calculations, which themselves might be prone to error, are required; only fields and fluxes due to filaments need be computed and summed. This also eliminates the common uncomfortable problem of comparing the results from one code with those of another, perhaps unfamiliar, code. Finally, largely due to its simplicity and generality, the sample problem provides conclusive proof as to the basic correctness of the code.

Three solutions to the sample problem, obtained from cPFC runs, are shown in Table 4.2. The first column of currents was found by using the original set of plasma filaments (Plasma1–5 in Table 4.1) and their currents to compute the the field $\mathbf{B}_i$ in Eq. (4.13). Since this corresponds to having exact knowledge of the plasma current distribution, it would be expected that the PF and OH coil currents would be reproduced extremely well. Table 4.2 shows that this is indeed the case.

The second column of currents in Table 4.2 corresponds to the more usual case when the plasma current distribution is assumed to be not well known. Then, as was previously stated, we represent this unknown distribution with a single filament, carrying the total plasma current, located near the magnetic axis. The geometry of this situation is shown in Fig. 4.3a. As Table 4.2 shows,

Table 4.2: *Output Filament Currents in cPFC Sample Problem*

Label	Exact Case	0.64 m Case	0.70 m Case
PF1 (MA)	−0.593	−0.618	−0.537
PF2 (MA)	+0.935	+0.933	+0.940
PF3 (MA)	+0.931	+0.928	+0.934
OH1 (MA)	+0.988	+0.975	+0.939
OH2 (MA)	+0.988	+0.975	+1.017
OH3 (MA)	+0.988	+0.975	+1.017
OH4 (MA)	+0.988	+0.975	+1.017
OH5 (MA)	+0.988	+0.975	+1.017

the currents are again reproduced well with the largest error being 5 % on the conductor (PF1) carrying the least amount of current. The currents in the outer filaments, particularly PF2 and PF3, are computed much more accurately. The fact that the error is smallest on the conductors located on the outboard side of the plasma is predictable since they provide the largest amount of shaping field. Finally, for this case, $b_e = 0.0032$ so it is expected that the the tangential field on the plasma surface is being matched very well. This contention is confirmed by Fig. 4.4, which compares the known and computed fields.

The third column of currents in Table 4.2 correspond to the extreme case where the filament representing the plasma current distribution is displaced outward to an R-coordinate of 0.70 m. This geometry is shown in Fig. 4.3b. Since the current weighted centroid of the plasma filament current arrangement is at $R = 0.64$ m, this case tests the performance of the code when the exact plasma current distribution is poorly modeled. Again, Table 4.2 shows that the currents are reproduced quite well.

On the basis of these results presented here, we conclude that the basic correctness of cPFC has been verified.

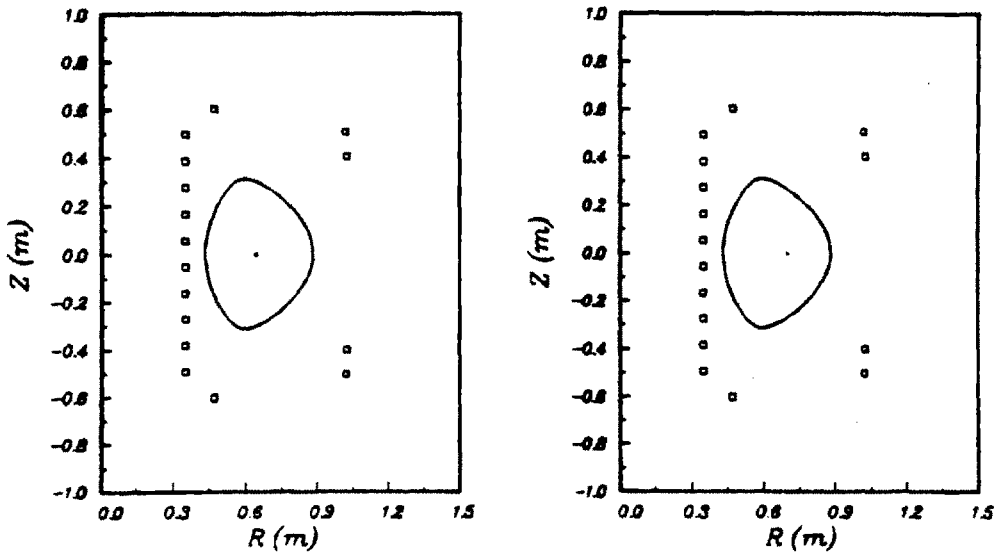

Figure 4.3: *Plasma filament geometries used in cPFC sample problem: (a) single filament at* $R = 0.64\,\mathrm{m}$*, (b) single filament at* $R = 0.70\,\mathrm{m}$*.*

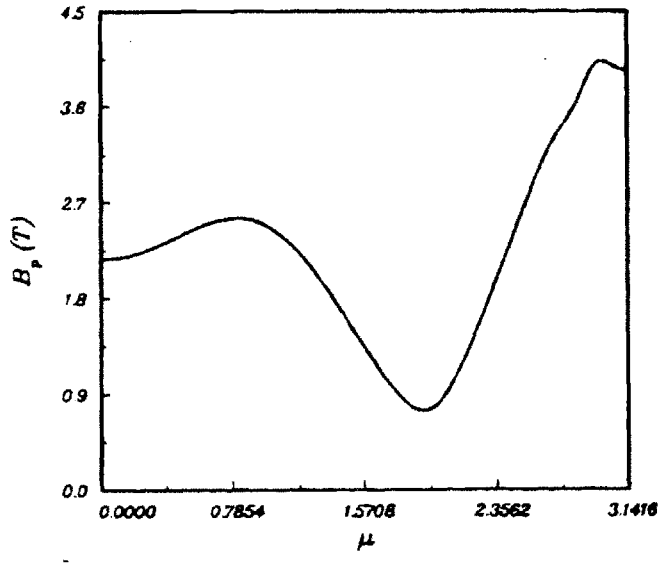

Figure 4.4: *Plot of tangential field from known filament currents (solid line) and tangential field computed with cPFC using a single plasma filament at* $R = 0.64\,\mathrm{m}$ *(almost indistinguishable dotted line) vs.* μ*.*

4.5.3 Field Error Limits

One final point about this procedure should be noted. Namely, for a given plasma shape and conductor configuration, the methods of this chapter are quite robust and always find the "best" estimate of the conductor currents needed to hold the plasma in equilibrium. However, this does not guarantee that these currents will produce the desired plasma in a real experiment. For example, this procedure could, in principle, be applied to a problem where a dee or bean shaped plasma is to be supported by a single PF coil current. The procedure would yield an estimate for the current in this coil; but, it is obviously extremely unlikely that this would yield a viable plasma.

In the example with the plasma supported by a single coil, it is fairly obvious that the cPFC solution does not correspond to a real equilibrium solution. However, one can easily imagine cases where it is not so obvious that a particular set of conductors cannot, in reality, support a given plasma shape. Therefore, it is necessary to state a condition that can be used as a guide for determining when a cPFC solution corresponds to a viable equilibrium.

Obviously, one would expect that the field error b_e would be extremely large for the case of a plasma supported by a single wire. Similarly, one might expect that, in general, there might be a threshold in b_e such that if the field error is larger than the threshold value, the specified conductor configuration cannot support the desired shape.

The determination of the critical b_e has been addressed in a limited fashion in this thesis. In particular, we examine the issue using the following procedure. We first calculate a plasma equilibrium supported by 32 coils using the exact equilibrium code NEQ. We then take the equilibrium information and use it as input for a series of cPFC runs. Specifically, we calculate the optimal coil currents predicted by cPFC to support the specified shape using first 32 coils, then 16 coils, then 12 coils, and finally 8 coils. Then, for each case, we take the cPFC coil current estimates and use them as inputs to

NEQ. When fixed coil currents are used as input to NEQ, the code performs a free boundary calculation and returns the exact plasma shape obtainable using the specified currents. We can conclude that the cPFC currents represent a reasonable approximation to the free boundary calculation if the shape NEQ returns is close to the desired shape.

The above procedure is depicted graphically in Fig. 4.5. The desired equilibrium corresponds to the resistive-magnet tokamak reactor plasma discussed in Chapters 2 and 3. In Fig. 4.5a, 32 conductors are used to support the equilibrium. Due to the large number of coils, the cPFC field error b_ϵ is quite low and the shape that results when the cPFC currents are used as inputs to NEQ (dotted surface) match the desired shape (solid surface) very closely. In Fig. 4.5b, the number of conductors has been reduced to 16. As expected, the agreement between the cPFC shape and the desired shape is somewhat worse and the field error b_ϵ is larger. This trend continues in Fig. 4.5c where the number of conductors has been reduced to 12. However, in Fig. 4.5d, we see that the cPFC free boundary shape does not correspond well at all to the desired shape. This is an indication that the value of b_ϵ for that case ($b_\epsilon = 0.10$) is too large to yield a viable free boundary equilibrium.

On the basis of the above test, we recommend that only coil current estimates characterized by $b_\epsilon < 0.05$ be accepted as valid approximations for true free boundary calculations. In any event, special attention should be given to reducing b_ϵ to the smallest feasible value in order to increase the robustness of the resulting equilibrium. Based on the work of Helton, *et al.* [68,69], this can be accomplished by locating the PF coil set relatively close to the plasma (usually within a plasma minor radius) and employing a sufficiently large number of PF coils. Finally, it should be emphasized that if the exact numerical values of the PF coil currents are critical, the estimates from this procedure should be verified with a full free boundary calculation. Even in this case, the coil current estimates could be useful for preliminary design work and/or initial parameter scans.

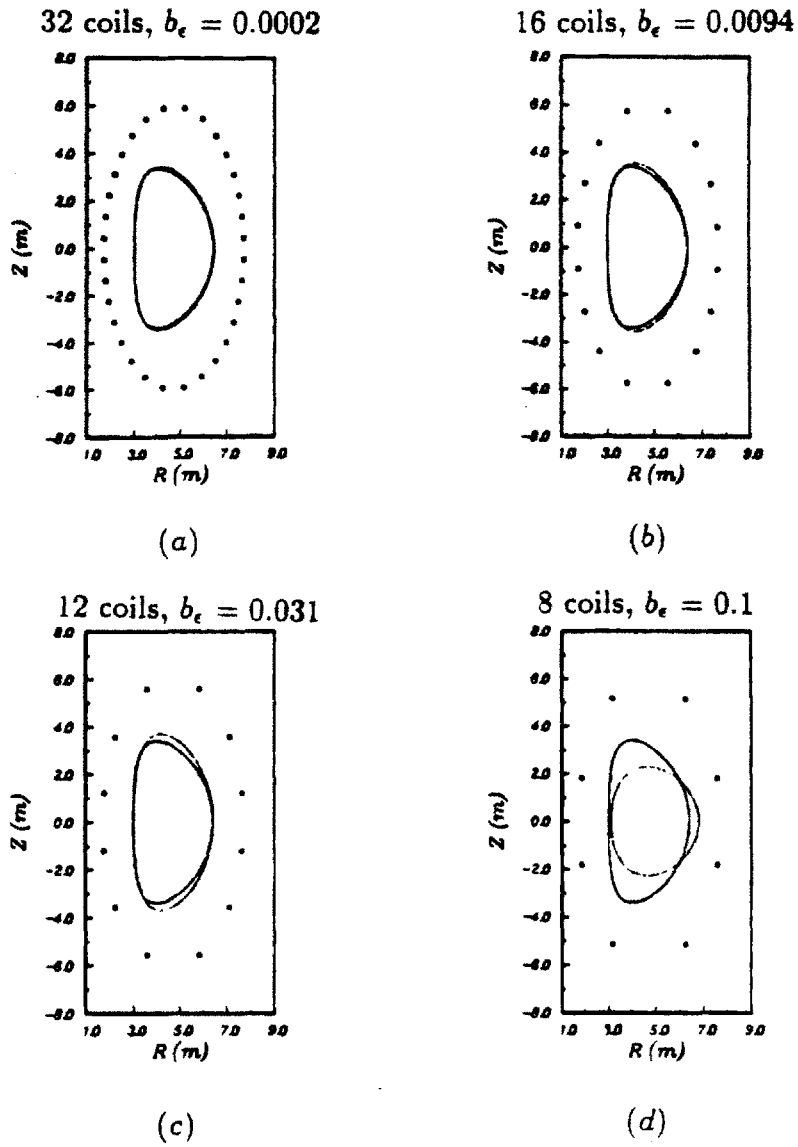

Figure 4.5: *cPFC field error analysis: comparison between desired shape (solid lines) and shape actually obtained by substituting cPFC current estimates into NEQ (dotted lines). The number of coils used to support the equilibrium varies from plot to plot.*

4.6 Effect of Approximate Equilibrium Information

Since the procedure presented in this chapter requires only fixed boundary equilibrium information, it would be extremely desirable to be able to employ the fast variational techniques described in the previous chapter to generate this information. However, in view of the approximate nature of these techniques, a legitimate concern is whether the equilibrium information is accurate enough to yield reasonable estimates of the conductor currents. This question will be addressed with the aid of the two sample equilibria presented in the previous chapter.

4.6.1 Conventional Circular Tokamak

We first consider the conventional circular tokamak whose equilibrium parameters are summarized in Tables 3.2 and 3.3. For purposes of illustration, we will assume that this plasma is surrounded by the relatively simple conductor configuration depicted in Fig. 4.6. To examine the effect of the approximate nature of the equilibrium on the PF coil current calculation, cPFC will be used to compute two sets of current estimates. The first set will be calculated using B_p as found by ePFC as an input and the second set will be calculated using the exact field produced by NEQ as an input.

The results from the two cPFC runs are shown in Table 4.3. It is seen that the currents in the outer shaping coils match very well whereas the agreement of the currents for the coil on the inboard side is less good. This is due to two effects. First, as mentioned previously, the largest discrepancy between the ePFC and NEQ fields is localized at the top and inboard side of the plasma. This discrepancy would naturally be expected to affect the current estimates in the nearby inboard conductor the most. Second, conductors on the inboard side of the plasma generally produce a smaller contribution to

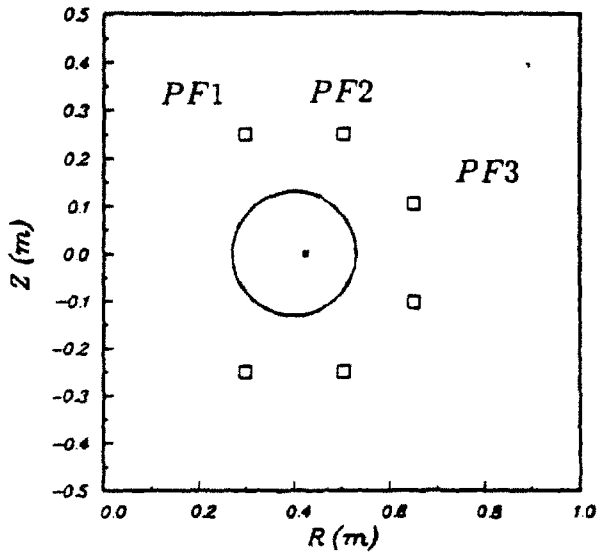

Figure 4.6: *Plasma-conductor geometry for conventional tokamak case.*

the total field at the plasma surface than the outboard conductors. Hence, $\epsilon_I(\mathrm{i})$ is less sensitive to errors in the currents in those conductors than to errors in the conductors on the outboard side of the plasma. On the basis of these considerations, it is not surprising that the currents in the outboard conductors match most closely.

Also listed in Table 4.3 are various other quantities characterizing the conductor current estimates. These are b_e, P_{PF} (computed assuming all of the conductors have square cross-sections of area $6.25 \times 10^{-4}\,\mathrm{m}^2$), $\sum I_j$, and $\sum I_j^2$. All of the values resulting from the ePFC data agree relatively well with those resulting from the NEQ data.

As a final point, Fig. 4.7 shows a comparison of the input tangential magnetic field at the plasma surface (as computed by NEQ) with the output field resulting from the calculated conductor currents. Despite the lack of smoothness in the input field (probably resulting from the finite differencing scheme that NEQ employs), the output field matches quite well.

Table 4.3: *Output Current Data for Conventional Tokamak Case*

Quantity	ePFC Input	NEQ Input
PF1 Current (KA)	1.420	1.640
PF2 Current (KA)	1.980	1.994
PF3 Current (KA)	1.712	1.720
b_e	0.0075	0.0194
P_{PF} (KW)	1.672	1.761
$\sum I_j$ (KA)	10.23	10.70
$\sum I_j^2$ (KA^2)	17.74	19.24

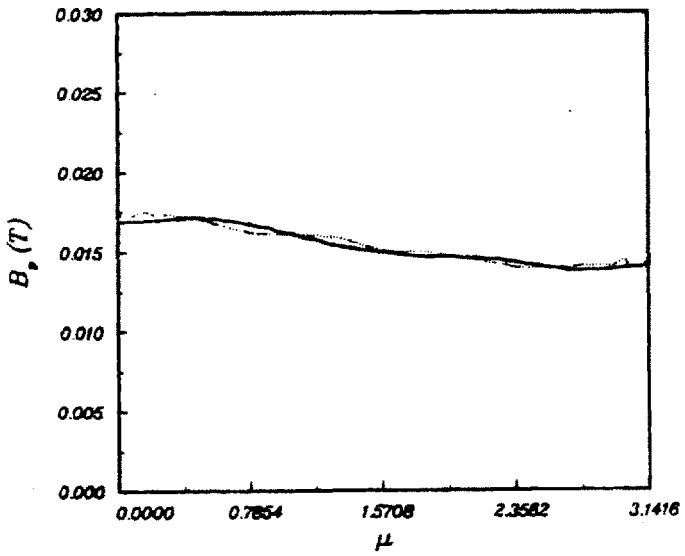

Figure 4.7: *Plot of input tangential field from NEQ (solid line) and output tangential field computed with cPFC (dotted line) vs. μ for conventional tokamak case.*

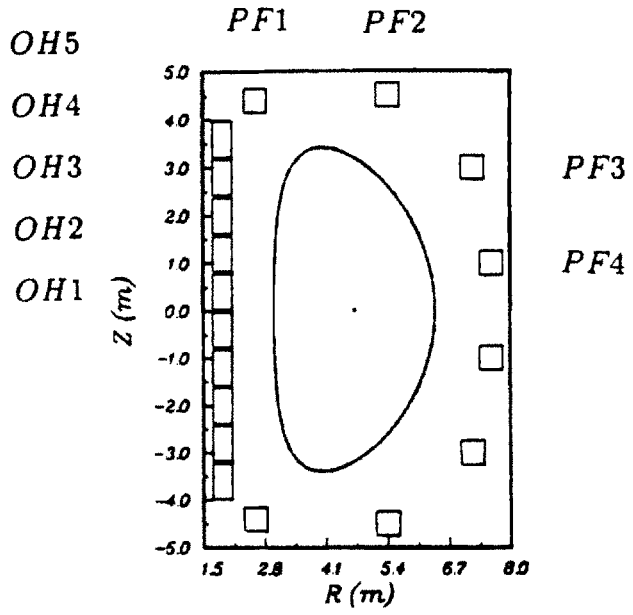

Figure 4.8: *Plasma-conductor geometry for strongly shaped tokamak case.*

4.6.2 Strongly Shaped Tokamak

We now consider the strongly shaped tokamak case (corresponding to the resistive-magnet tokamak reactor base design from Chapter 2) whose equilibrium parameters are summarized in Tables 3.4 and 3.5. Due to this strong shaping, the conductor configuration surrounding the plasma is necessarily more complicated than that for the conventional circular tokamak. This configuration is depicted in Fig. 4.8.

Again, we will compare the conductor currents found using ePFC equilibrium data with those found using NEQ equilibrium data. This comparison is shown in Table 4.4. The agreement between the two cases is not as close as that for the conventional tokamak, but it is still quite good considering the discrepancy in the input fields. (See Fig. 3.12). In any event, Fig. 4.9 shows that, despite the strong plasma shaping, the field produced by the calculated conductor currents matches the input field quite well.

Table 4.4: *Output Current Data for Conventional Tokamak Case*

Quantity	ePFC Input	NEQ Input
PF1 Current (MA)	3.255	3.839
PF2 Current (MA)	2.254	1.679
PF3 Current (MA)	3.617	3.703
PF4 Current (MA)	2.282	2.684
OH1 Current (MA)	5.676	6.552
OH2 Current (MA)	5.676	6.552
OH3 Current (MA)	5.676	6.552
OH4 Current (MA)	4.183	3.954
OH5 Current (MA)	4.183	3.954
b_e	0.0186	0.0224
P_{PF} (MW)	358	416
$\sum I_j$ (MA)	73.61	78.94
$\sum I_j^2$ (MA^2)	331	397

These examples of relatively good agreement would seem to confirm the contention, made in the previous chapter, that the PF current calculation is fairly insensitive to errors in the fields near the separatrix. Hence, the use of approximate equilibrium data does not appear to introduce unacceptable errors in the PF coil current calculation.

As a final point, it should be noted that the conductor configuration in Fig. 4.8 has not been optimized in an engineering sense. In particular, the large values of P_{PF} are a concern since the resistive magnet tokamak reactor base design (Table 2.1) assumes $P_{PF} = 125\,\mathrm{MW}$. This issue has been investigated and a number of conductor configurations consistent with the base design value for P_{PF} have been found. However, these configurations also suggest that the assumed intermediate thickness $b = 1\,\mathrm{m}$ may be too optimistic with regard to fitting both the blanket and the PF/OH coils in the available space. The issue of the required intermediate region thickness

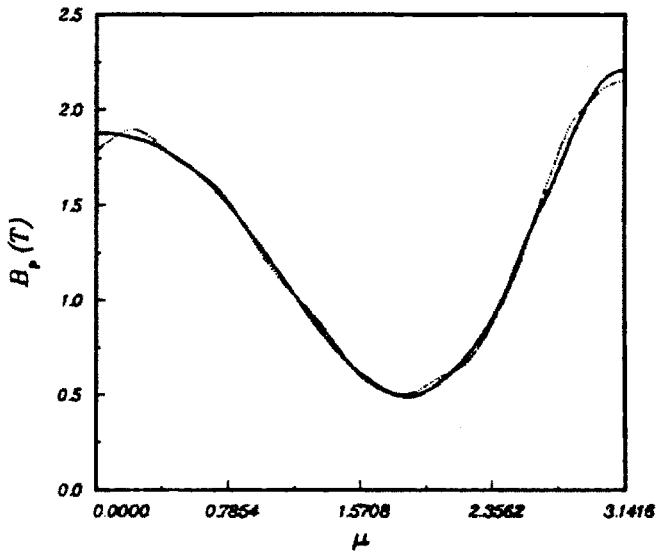

Figure 4.9: *Plot of input tangential field from NEQ (solid line) and output tangential field computed with cPFC (dotted line) vs. μ for strongly shaped tokamak case.*

will not be addressed in this thesis; but, using the techniques introduced in the this and the previous chapter, it is expected that the answer could be gained relatively quickly and easily.

Chapter 5

Stability in the Presence of a Resistive Wall

It is a well known from ideal MHD theory that external kink modes can be completely stabilized if a perfectly conducting wall is located sufficiently close to the plasma [17–21]. Furthermore, several authors have shown that when the perfectly conducting wall is replaced by one possessing finite resistivity, modes that were initially stable begin to grow on a timescale comparable to the resistive diffusion time associated with the wall τ_D [71,72].

The vacuum chambers of many modern fusion devices are constructed of materials, such as stainless steel, which possess large resistivities (and correspondingly small resistive diffusion times) in order to allow quick penetration of the fields produced by external shaping and ohmic heating coils. Hence, improvements in confinement have led to situations where experimental lifetimes are potentially much greater than τ_D. This means that the estimation of growth rates for unstable modes in the presence of a resistive wall takes on great practical importance.

In this chapter, we will describe a procedure, again based on variational techniques, for estimating the growth rate of an arbitrary three-dimensional

external mode for an arbitrarily shaped plasma in the presence of an arbitrarily shaped thin resistive wall. This procedure will be derived in five parts. First, the ideal case where no wall is present will be examined with the aid of the Extended Energy Principle. In general, it will be found that $\delta W < 0$ indicating instability on the ideal MHD timescale. Second, the case where a perfectly conducting wall is present will be considered. Here, it will be found that if the wall is sufficiently close to the plasma, δW can be made positive indicating ideal wall stabilization. Third, the effect of placing a resistive wall in place of the perfectly conducting wall will be derived. This will be seen to take the form of jump conditions for the tangential electric and magnetic fields across the wall. Fourth, the information gained in the previous three steps will be compiled to yield a variational principle describing the dynamics of the plasma in the presence of a resistive wall. Finally, trial functions for the fields in the vacuum regions inside and outside the the resistive wall will be substituted into the variational principle to yield an estimate for the growth rate. The chapter will conclude with a discussion of non-ideal effects on resistive wall instabilities and an application of the theory to the important special case of axisymmetric ($n = 0$) stability of tokamaks.

5.1 The Ideal Case

As a point of reference, consider the stability of an arbitrary three dimensional plasma configuration with and without a perfectly conducting wall. The stability of such a system can be tested by means of the Extended Energy Principle [70].

5.1.1 The Wall at Infinity

When the conducting wall is moved infinitely far away the Energy Principle has the form

$$\delta W = \delta W_F + \delta W_V, \tag{5.1}$$

where

$$\delta W_F = \frac{1}{2}\int_{V_P}\left[\frac{|\delta\mathbf{B}|^2}{\mu_0} - \xi\cdot(\mathbf{J}\times\delta\mathbf{B}) + \Gamma p|\nabla\cdot\xi|^2 + (\xi\cdot\nabla p)\nabla\cdot\xi\right] dV, \tag{5.2}$$

$$\delta W_V = \frac{1}{2}\int_V \frac{|\delta\hat{\mathbf{B}}|^2}{\mu_0}\, dV. \tag{5.3}$$

Here, δW_F is the fluid energy integrated over the plasma volume and δW_V is the vacuum energy integrated over the vacuum region exterior to the plasma. Also, it has been assumed that no surface currents flow on the plasma boundary so that the surface energy $\delta W_S = 0$.

Wall stabilization, with either ideal or resistive walls, involves the study of external plasma instabilities (e.g. external kinks, axisymmetric modes, etc). For such modes, one specifies the normal component of plasma displacement, evaluated on the plasma surface S_p:

$$\xi(S_p) \equiv \mathbf{e}_n\cdot\xi\,|_{S_p}\,. \tag{5.4}$$

Once $\xi(S_p)$ is specified, δW_F and δW_V can, in principle, be independently minimized. Stability is determined by examining the sign of the combined δW after carrying out a final minimization with respect to $\xi(S_p)$ itself.

For present purposes, it is useful to assume that δW_F has been minimized with respect to the given $\xi(S_p)$ and to then focus attention on δW_V. The vacuum energy is found by writing

$$\delta\hat{\mathbf{B}} = \nabla \times \delta\hat{\mathbf{A}} \tag{5.5}$$

with $\delta\hat{\mathbf{A}}$ satisfying

$$\nabla \times \nabla \times \delta\hat{\mathbf{A}} = 0. \tag{5.6}$$

The boundary conditions (with the wall at infinity) are given by

$$\delta\hat{\mathbf{A}} \mid_{\infty} \;=\; 0, \tag{5.7}$$

$$\mathbf{e}_n \times \delta\hat{\mathbf{A}} \mid_{S_p} \;=\; -(\mathbf{e}_n \cdot \xi)\mathbf{B} \mid_{S_p} . \tag{5.8}$$

Equation (5.8) is the linearized form of the jump condition $[\![\mathbf{e}_n \times \mathbf{E}]\!]_{S_p} = 0$.

The linearized pressure balance jump condition $[\![p + B^2/2\mu_0]\!]_{S_p} = 0$ has the form

$$\mathbf{B} \cdot \nabla \times \delta\hat{\mathbf{A}} \mid_{S_p} = \mathbf{B} \cdot \nabla \times (\xi \times \mathbf{B}) \mid_{S_p} . \tag{5.9}$$

As is well known, Eq. (5.9) appears as a natural boundary condition in the minimization of δW. Thus, for the true minimizing solution, Eq. (5.9) is automatically satisfied. Conversely, for any other trial function, Eq. (5.9) will not be exactly satisfied. However, since the energy principle is a variational principle, the minimization of δW (with respect to the variational parameters in the trial function) will "do as good a job as possible" in satisfying Eq. (5.9).

Whether the exact solution, or a trial function, is used for ξ, we shall assume that the vacuum energy is minimized exactly with respect to ξ by solving Eqs. (5.5)–(5.8). Under this assumption, the potential energy corresponding to the wall at infinity can be written as

$$\delta W_{\infty} = \delta W_F + \delta W_V^{(\infty)}, \tag{5.10}$$

where

$$\delta W_V^{(\infty)} = \frac{1}{2\mu_0} \int_{S_p} (\mathbf{e}_n \times \delta\hat{\mathbf{A}}_{\infty}) \cdot \mathbf{e}_n \times (\mathbf{e}_n \times \nabla \times \delta\hat{\mathbf{A}}_{\infty})\, dS \tag{5.11}$$

and the notation has been changed so that $\delta\hat{\mathbf{A}}$ is replaced by $\delta\hat{\mathbf{A}}_\infty$ (indicating that Eq. (5.6) has been satisfied).

Wall stabilization plays an important role in systems which are unstable with the wall at infinity. Consequently, we shall hereafter consider

$$\delta W_\infty < 0. \tag{5.12}$$

5.1.2 The Wall a Finite Distance from the Plasma

Consider now the situation where a closed, perfectly conducting wall of arbitrary shape is located a finite distance from the plasma. The surface of the wall is denoted by S_b. In addition, assume that the plasma surface perturbation $\xi(S_p)$ is identical to that used in the evaluation of δW_∞.

Under these circumstances, the potential energy can be expressed as

$$\delta W_b = \delta W_F + \delta W_V^{(b)}, \tag{5.13}$$

where δW_F has the same value as in Eq. (5.10) and

$$\delta W_V^{(b)} = \frac{1}{2\mu_0}\int_{S_p} (\mathbf{e}_n \times \delta\hat{\mathbf{A}}_b)\cdot \mathbf{e}_n \times (\mathbf{e}_n \times \nabla \times \delta\hat{\mathbf{A}}_b)\, dS. \tag{5.14}$$

The vector potential $\delta\hat{\mathbf{A}}_b$ satisfies

$$\nabla \times \nabla \times \delta\hat{\mathbf{A}}_b = 0 \tag{5.15}$$

subject to the boundary conditions

$$\mathbf{e}_n \times \delta\hat{\mathbf{A}}_b \mid_{S_b} \;=\; 0, \tag{5.16}$$

$$\mathbf{e}_n \times \delta\hat{\mathbf{A}}_b \mid_{S_p} \;=\; -(\mathbf{e}_n \cdot \xi)\mathbf{B} \mid_{S_p}. \tag{5.17}$$

As might be expected, the only difference in the calculation of $\delta\hat{\mathbf{A}}_b$ compared to $\delta\hat{\mathbf{A}}_\infty$ is that the boundary condition given by Eq. (5.7) is replaced by Eq. (5.16), indicating the presence of a perfectly conducting wall.

The situations of interest for resistive wall problems are characterized by values of δW_b which are wall stabilized by a perfectly conducting wall. Hence, hereafter we shall assume that

$$\delta W_b > 0. \tag{5.18}$$

5.1.3 Summary of Ideal Stability

In summary, a resistive wall is expected to play a major role in the stability of external MHD modes when the system is unstable with the wall at infinity but stable with a perfectly conducting wall a finite distance from the plasma:

$$\delta W_\infty = \delta W_F + \delta W_V^{(\infty)} < 0, \tag{5.19}$$

$$\delta W_b = \delta W_F + \delta W_V^{(b)} > 0. \tag{5.20}$$

The values of δW_F inEqs. (5.19) and (5.20) are identical since the same $\xi(S_p)$ has been assumed for each case.

The evaluation of the vacuum energies $\delta W_V^{(\infty)}$ and $\delta W_V^{(b)}$ is nearly identical. Both corresponding vector potentials $\delta \hat{\mathbf{A}}_\infty$, $\delta \hat{\mathbf{A}}_b$ satisfy the same equation and the same boundary condition on the surface S_p. They differ only in the outer boundary condition.

$$\delta \hat{\mathbf{A}}_\infty \,|_\infty \;=\; 0, \tag{5.21}$$

$$\mathbf{e}_n \times \delta \hat{\mathbf{A}}_b \,|_{S_b} \;=\; 0. \tag{5.22}$$

Ultimately, the growth rate of unstable modes in the presence of a resistive wall will be expressed explicitly in terms of δW_∞ and δW_b.

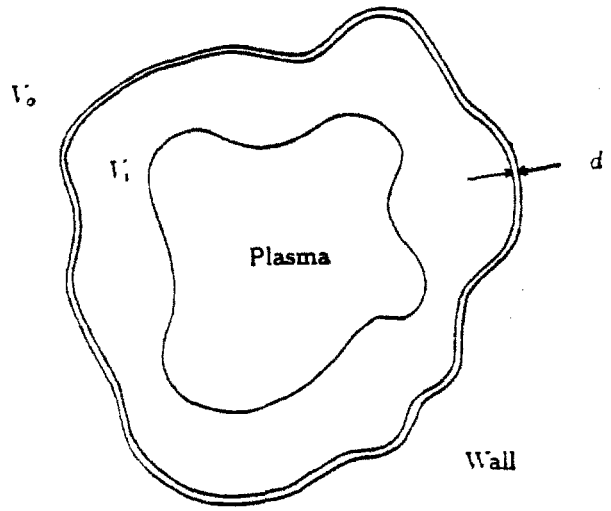

Figure 5.1: *Plasma-resistive wall geometry.*

5.2 The Resistive Wall Case

In this section, we replace the perfectly conducting wall at S_b with a thin resistive wall characterized by a conductivity σ and thickness d. See Fig. 5.1. By exploiting the thin wall assumption, we will then derive a relatively simple variational principle describing the stability of external modes in the presence of a resistive wall.

5.2.1 Time and Length Scale Orderings

The critical insight in the analysis of resistive wall MHD problems is the recognition that instabilities, if they exist, will be slowly growing modes with growth rates γ comparable to the resistive diffusion time of the wall τ_D:

$$\gamma \sim \frac{1}{\tau_D}. \tag{5.23}$$

Here, $\tau_D = \mu_0 \sigma \bar{b} d$ and $\bar{b}$ is a measure of the average radius of the vacuum chamber. Due to the scaling in Eq. (5.23)

$$\gamma \ll \gamma_{MHD}, \tag{5.24}$$

where $\gamma_{MHD}^2 = -\delta W_\infty / K$ is the characteristic ideal MHD growth rate with the wall at infinity. For the Alcator C-Mod tokamak $\bar{b} \sim 0.4\,\mathrm{m}$, $d \sim 0.025\,\mathrm{m}$, and $1/\sigma \sim 69.5 \times 10^{-8}\,\Omega \cdot \mathrm{m}$ so $\gamma \sim 55\,\mathrm{Hz}$. Typically $\gamma_{MHD} \sim 2 \times 10^6\,\mathrm{Hz}$ so Eq. (5.24) is usually well satisfied.

The thin wall model assumes

$$d \ll \bar{b} \tag{5.25}$$

but it is necessary to ensure that d is not so small that Eq. (5.24) is violated.

The orderings given by Eqs. (5.23)–(5.25) imply that plasma inertial effects are negligible on the time scale of interest. This leads to a substantial simplification in the analysis. In particular, the equation describing the linearized plasma behavior is just

$$\mathbf{F}(\xi) = 0, \tag{5.26}$$

where $\mathbf{F}$ is the well-known force operator of ideal MHD. *Consequently, the exact minimizing solution for the ideal MHD δW is also the exact eigenfunction for the resistive wall eigenvalue problem.* Similarly, the use of an approximate trial function to evaluate the ideal MHD δW represents an equally accurate approximation for the resistive wall eigenfunction.

5.2.2 Magnetic Field Solutions

As Fig. 5.1 shows, the volume surrounding the plasma is divided into three parts: an inner vacuum region, the resistive wall, and an outer vacuum region. Before solving for the plasma dynamics, it will be necessary to state the governing equations and boundary conditions for the fields in those three regions.

Vacuum Region Analysis

The vector potentials for the inner and outer vacuum regions $\delta\hat{\mathbf{A}}_i$ and $\delta\hat{\mathbf{A}}_o$ satisfy

$$\nabla \times \nabla \times \delta\hat{\mathbf{A}}_i = 0, \tag{5.27}$$

$$\nabla \times \nabla \times \delta\hat{\mathbf{A}}_o = 0. \tag{5.28}$$

Furthermore, at the plasma surface, the boundary condition on $\delta\hat{\mathbf{A}}_i$ is given by

$$\mathbf{e}_n \times \delta\hat{\mathbf{A}}_i \mid_{S_p} = -(\mathbf{e}_n \cdot \xi)\mathbf{B}, \tag{5.29}$$

while, far from the wall, the corresponding condition on $\delta\hat{\mathbf{A}}_o$ has the form

$$\delta\hat{\mathbf{A}}_o \mid_{\infty} = 0. \tag{5.30}$$

For a real wall, no surface currents exist on either face of the shell. Consequently the tangential components of both $\delta\mathbf{E}$ and $\delta\mathbf{B}$ must be continuous across both interfaces. In terms of $\delta\mathbf{A}$ these boundary conditions are given by

$$\begin{aligned} [\mathbf{e}_n \times \delta\mathbf{A}]_{S_i} &= 0 \qquad [\mathbf{e}_n \times \delta\mathbf{A}]_{S_o} = 0, \\ [\mathbf{e}_n \times \nabla \times \delta\mathbf{A}]_{S_i} &= 0 \quad [\mathbf{e}_n \times \nabla \times \delta\mathbf{A}]_{S_o} = 0. \end{aligned} \tag{5.31}$$

Here, S_i and S_o represent the interior and exterior faces of the conducting wall respectively.

Resistive Wall Analysis

The fields within the resistive wall are calculated as follows. First, the electric and magnetic fields are expressed as

$$\delta\mathbf{E}_w = -\frac{\partial \delta\mathbf{A}_w}{\partial t}, \tag{5.32}$$

$$\delta\mathbf{B}_w = \nabla \times \delta\mathbf{A}_w, \tag{5.33}$$

indicating that $\phi = 0$ has been chosen as the gauge condition. The wall itself is considered to be a thin metallic shell of uniform thickness d and uniform conductivity σ. Hence, in the wall $\delta\mathbf{J}_w = \sigma\delta\mathbf{E}_w$. Using the fact that all perturbed quantities vary as $\delta Q(\mathbf{r}, t) = \delta Q(\mathbf{r})\exp(\gamma t)$, it follows from Ampere's law that $\delta\mathbf{A}_w$ satisfies

$$\nabla \times \nabla \times \delta\mathbf{A}_w = -\mu_0\sigma\gamma\delta\mathbf{A}_w. \tag{5.34}$$

The solution for $\delta\mathbf{A}_w$ can be found analytically for an arbitrarily shaped wall by exploiting the thin wall assumption. Two steps are required, one which separates normal from tangential derivatives, and the other which results in the expansion of $\delta\mathbf{A}_w$ with respect to the perpendicular distance into the wall.

Consider the separation of normal and tangential derivatives. To do this in a convenient manner we will represent points within the wall using the parameterization

$$\mathbf{r} = \mathbf{r}_i + u d\mathbf{e}_n, \tag{5.35}$$

where $\mathbf{r}_i$ is a constant vector representing the inner surface of the conducting wall and, in this context, $\mathbf{e}_n$ is the unit vector normal to the inner surface of the wall. The normalized length u represents perpendicular distance measured outward from the inner surface of the wall. Thus, $u = 0$ and $u = 1$ correspond to S_i and S_e respectively.

Using the coordinate transformation in Eq. (5.35) and invoking the thin wall assumption [Eq. (5.25)] allows the gradient operator to be written

$$\nabla = \frac{\mathbf{e}_n}{d}\frac{\partial}{\partial u} + \nabla_S, \tag{5.36}$$

where ∇_S only involves derivatives tangent to the surface of the wall.

In the limit of a thin wall, it is assumed that $\delta\mathbf{A}_w$ varies much more rapidly normal to the wall than tangent to it. Therefore, we formally introduce a small parameter $\delta \sim d/\bar{b}$ and assume the following ordering for the derivatives

$$\frac{\partial}{\partial u} \sim 1, \tag{5.37}$$

$$\bar{b}\nabla_S \sim 1. \tag{5.38}$$

The above ordering can now be used to define an expansion for $\delta\mathbf{A}_w$ in a manner entirely analogous to the "constant-ψ" approximation of tearing mode theory [73]. The appropriate expansion is given by

$$\delta\mathbf{A}_w(u, S) = \delta\mathbf{A}_{w0}(S) + \delta\mathbf{A}_{w1}(u, S) + \cdots \tag{5.39}$$

where $\delta\mathbf{A}_{w1}/\delta\mathbf{A}_{w0} \sim \delta$ and $F(S)$ denotes a functional dependence only on tangential surface coordinates. The corresponding maximal ordering for γ requires

$$\mu_0\sigma\gamma\bar{b}d \sim 1 \tag{5.40}$$

which is seen to be compatible with Eq. (5.23).

After a short calculation, it can be shown that the leading order contribution to Eq. (5.34) reduces to

$$\frac{\partial^2}{\partial u^2}(\mathbf{e}_n \times \delta\mathbf{A}_{w1}) = \mu_0\sigma\gamma d^2(\mathbf{e}_n \times \delta\mathbf{A}_{w0}). \tag{5.41}$$

The solution of Eq. (5.41) is easily found to be

$$\mathbf{e}_n \times \delta\mathbf{A}_{w1} = \mathbf{a}_1(S) + \mathbf{c}_1(S)u + \mu_0\sigma\gamma d^2(\mathbf{e}_n \times \delta\mathbf{A}_{w0})(u^2/2), \tag{5.42}$$

where $\mathbf{a}_1$ and $\mathbf{c}_1$ are integration constants, each of order δ.

A set of jump conditions involving $\delta\hat{\mathbf{A}}_i$ and $\delta\hat{\mathbf{A}}_o$ can be found by applying the boundary conditions given by Eq. (5.31). The results can be written, correct to leading order, as follows

$$\mathbf{e}_n \times \delta\hat{\mathbf{A}}_i \mid_{S_i} = \mathbf{e}_n \times \delta\mathbf{A}_{w0}, \tag{5.43}$$

$$\mathbf{e}_n \times \delta\hat{\mathbf{A}}_o \mid_{S_o} = \mathbf{e}_n \times \delta\mathbf{A}_{w0}, \tag{5.44}$$

$$\mathbf{e}_n \times \nabla \times \delta\hat{\mathbf{A}}_i \mid_{S_i} = \frac{1}{d}\mathbf{e}_n \times \mathbf{c}_1, \tag{5.45}$$

$$\mathbf{e}_n \times \nabla \times \delta\hat{\mathbf{A}}_o \mid_{S_o} = \frac{1}{d}\mathbf{e}_n \times \mathbf{c}_1 + \mu_0\sigma\gamma d\mathbf{e}_n \times (\mathbf{e}_n \times \delta\mathbf{A}_{w0}). \tag{5.46}$$

By subtracting Eq. (5.43) from Eq. (5.44) and Eq. (5.45) from Eq. (5.46) we see that the effect of the resistive wall explicitly appears only as a contribution to the jump conditions on $\delta\hat{\mathbf{A}}_i$ and $\delta\hat{\mathbf{A}}_o$ across the wall. Specifically, we obtain

$$\mathbf{e}_n \times \delta\hat{\mathbf{A}}_i \mid_{S_b} = \mathbf{e}_n \times \delta\hat{\mathbf{A}}_o \mid_{S_b}, \tag{5.47}$$

$$\begin{aligned} \mathbf{e}_n \times (\mathbf{e}_n \times \nabla \times \delta\hat{\mathbf{A}}_i) \mid_{S_b} \;=\; & \mathbf{e}_n \times (\mathbf{e}_n \times \nabla \times \delta\hat{\mathbf{A}}_o) \mid_{S_b} + \\ & \mu_0\sigma\gamma d(\mathbf{e}_n \times \delta\hat{\mathbf{A}}) \mid_{S_b} . \end{aligned} \tag{5.48}$$

5.2.3 Resistive Wall Variational Principle

In analogy to the derivation of the Energy Principle, Eq. (5.26) can be used to define a Lagrangian representing the dynamics of a plasma in the presence of a resistive wall:

$$\mathcal{L} \equiv \int_{V_p} \xi \cdot \mathbf{F}(\xi)\, dV = 0. \tag{5.49}$$

This Lagrangian can be rewritten in the more familiar form

$$\mathcal{L} = \delta W_F + \frac{1}{2}\int_{S_p} (\mathbf{e}_n \cdot \xi)\left(\frac{\hat{\mathbf{B}} \cdot \delta\hat{\mathbf{B}}}{\mu_0}\right) dS. \tag{5.50}$$

For the purposes of this analysis, it is convenient to write $\mathcal{L}$ in still another way. This is accomplished by noting the following identities

$$\begin{aligned}
\delta W_V^{(i)} &= \frac{1}{2\mu_0}\int_{V_i} |\nabla \times \delta\hat{\mathbf{A}}_i|^2\, dV \\
&= \frac{1}{2}\int_{S_p} (\mathbf{e}_n \cdot \xi)\left(\frac{\hat{\mathbf{B}} \cdot \delta\hat{\mathbf{B}}}{\mu_0}\right) dS - \\
&\quad \frac{1}{2\mu_0}\int_{S_b} (\mathbf{e}_n \times \delta\hat{\mathbf{A}}_i) \cdot \mathbf{e}_n \times (\mathbf{e}_n \times \nabla \times \delta\hat{\mathbf{A}}_i)\, dS,
\end{aligned} \tag{5.51}$$

$$\begin{aligned}
\delta W_V^{(o)} &= \frac{1}{2\mu_0}\int_{V_o} |\nabla \times \delta\hat{\mathbf{A}}_i|^2\, dV \\
&= \frac{1}{2\mu_0}\int_{S_b} (\mathbf{e}_n \times \delta\hat{\mathbf{A}}_o) \cdot \mathbf{e}_n \times (\mathbf{e}_n \times \nabla \times \delta\hat{\mathbf{A}}_o)\, dS,
\end{aligned} \tag{5.52}$$

where V_i and V_o refer to the vacuum regions inside and outside the resistive wall respectively (See Fig. 5.1). In addition, the relevant governing equations and boundary conditions [Eqs. (5.27)–(5.30)] for $\delta\hat{\mathbf{A}}_i$ and $\delta\hat{\mathbf{A}}_o$ have been applied in the derivation of Eqs. (5.51) and (5.52).

Using the resistive wall jump conditions in Eqs. (5.47) and (5.48), the desired form of $\mathcal{L}$ can be obtained

$$\mathcal{L} = \delta W_F + \delta W_V^{(i)} + \delta W_V^{(o)} + \frac{\sigma\gamma d}{2}\int_{S_b} |\mathbf{e}_n \times \delta\hat{\mathbf{A}}|^2\, dS. \tag{5.53}$$

As usual, to verify the validity of the variational principle, we evaluate $\delta\mathcal{L}$ and set it to zero. A relatively lengthy calculation yields

$$\begin{aligned}
\delta\mathcal{L} \;=\; & \int_{V_p} \delta\xi \cdot \mathbf{F}(\xi)\, dV + \\
& \frac{1}{\mu_0}\int_{V_i} \delta(\delta\hat{\mathbf{A}}_i)\cdot \nabla\times\nabla\times\delta\hat{\mathbf{A}}_i\, dV + \\
& \frac{1}{\mu_0}\int_{V_o} \delta(\delta\hat{\mathbf{A}}_o)\cdot \nabla\times\nabla\times\delta\hat{\mathbf{A}}_o\, dV + \\
& \int_{S_p} (\mathbf{e}_n\cdot\delta\xi)\left(\frac{(\hat{\mathbf{B}}\cdot\delta\hat{\mathbf{B}} - \mathbf{B}\cdot\delta\mathbf{B})}{\mu_0}\right) dS + \\
& \frac{1}{\mu_0}\int_{S_b} (\mathbf{e}_n\times\delta(\delta\hat{\mathbf{A}}))\cdot\Big[\mathbf{e}_n\times(\mathbf{e}_n\times\nabla\times\delta\hat{\mathbf{A}}_o) + \\
& \mu_0\sigma\gamma d(\mathbf{e}_n\times\delta\hat{\mathbf{A}}) - \mathbf{e}_n\times(\mathbf{e}_n\times\nabla\times\delta\hat{\mathbf{A}}_i)\Big]\, dS.
\end{aligned} \tag{5.54}$$

From Eq. (5.54), it can be seen that for the volume contributions to vanish, Eqs. (5.26), (5.27), and (5.28) must be satisfied. In addition, the surface contributions give rise to the two natural boundary conditions

$$\hat{\mathbf{B}}\cdot\delta\hat{\mathbf{B}}\,|_{S_p} \;=\; \mathbf{B}\cdot\delta\mathbf{B}\,|_{S_p}, \tag{5.55}$$

$$\begin{aligned}
\mathbf{e}_n\times(\mathbf{e}_n\times\nabla\times\delta\hat{\mathbf{A}}_i)\,|_{S_b} \;=\; & \mathbf{e}_n\times(\mathbf{e}_n\times\nabla\times\delta\hat{\mathbf{A}}_o)\,|_{S_b} + \\
& \mu_0\sigma\gamma d(\mathbf{e}_n\delta\hat{\mathbf{A}}\,|_{S_b}\,.
\end{aligned} \tag{5.56}$$

Finally, Eq. (5.54) was derived assuming the boundary conditions

$$\mathbf{e}_n\times\delta\hat{\mathbf{A}}_i\,|_{S_p} = -(\mathbf{e}_n\cdot\xi)\mathbf{B}\,|_{S_p}, \tag{5.57}$$

$$\mathbf{e}_n \times \delta\hat{\mathbf{A}}_i \mid_{S_b} = \mathbf{e}_n \times \delta\hat{\mathbf{A}}_o \mid_{S_b}, \tag{5.58}$$

$$\delta\hat{\mathbf{A}}_o \mid_{\infty} = 0, \tag{5.59}$$

are exactly satisfied. Since the set of relations that causes $\mathcal{L}$ to be stationary corresponds to the previously described governing equations and boundary conditions, we conclude that Eq. (5.53) represents the desired variational principle.

5.3 Resistive Wall Marginal Stability and Growth Rates

The resistive wall variational principle can be used to resolve two important questions of physical interest: (a) the condition for marginal stability, and (b) the determination of an accurate estimate of the growth rate for unstable cases.

5.3.1 Marginal Stability Criterion

The marginal stability criterion is easily found by considering the limit

$$\gamma\tau_D \to 0. \tag{5.60}$$

Physically, this corresponds to a situation where the plasma beta, current, elongation, or other physical parameter happens to have a value such that $\delta W_F + \delta W_V^{(i)} + \delta W_V^{(o)} \to \delta W_\infty \to 0$; in other words, the system is nearly marginally stable with the wall at infinity.

In this limit δW_∞ is minimized by choosing

$$\delta\hat{\mathbf{A}}_i \to \delta\hat{\mathbf{A}}_\infty, \quad \delta\hat{\mathbf{A}}_o \to \delta\hat{\mathbf{A}}_\infty. \tag{5.61}$$

If $\delta\hat{\mathbf{A}}_i$ or $\delta\hat{\mathbf{A}}_o$ was significantly different than $\delta\hat{\mathbf{A}}_\infty$, then sum $\delta W(\delta\hat{\mathbf{A}}) \equiv \delta W_F + \delta W_V^{(i)} + \delta W_V^{(o)}$ would also differ significantly from zero. The sum $\delta W(\delta\hat{\mathbf{A}})$ corresponds to the ideal MHD Energy Principle. Since the Energy Principle is a minimizing principle it follows that

$$\delta W(\delta\hat{\mathbf{A}} \neq \delta\hat{\mathbf{A}}_\infty) > \delta W(\delta\hat{\mathbf{A}}_\infty) \rightarrow 0, \tag{5.62}$$

that is, $\delta W(\delta\hat{\mathbf{A}} \neq \delta\hat{\mathbf{A}}_\infty) > 0$ and the system would be stable.

Consequently, near marginal stability, Eq. (5.61) applies and the growth rate, obtained by setting $\mathcal{L} = 0$ in Eq. (5.53) is given by

$$\gamma\sigma d = \frac{2\delta W_\infty}{\int_{S_b} |\mathbf{e}_n \times \delta\hat{\mathbf{A}}_\infty|^2 \, dS}. \tag{5.63}$$

As expected, the threshold for marginal stability in the presence of a resistive wall coincides with that of ideal MHD with the wall at infinity.

5.3.2 Growth Rate Estimate

In situations where δW_∞ is not near zero, we can obtain an accurate estimate of the growth rate by the use of trial functions. A convenient choice for $\delta\hat{\mathbf{A}}_i$ and $\delta\hat{\mathbf{A}}_o$ that takes into account the nature of the boundary conditions can be written as

$$\delta\hat{\mathbf{A}}_i = c_1\delta\hat{\mathbf{A}}_\infty + c_2\delta\hat{\mathbf{A}}_b, \tag{5.64}$$

$$\delta\hat{\mathbf{A}}_o = c_3\delta\hat{\mathbf{A}}_\infty. \tag{5.65}$$

The coefficients c_1, c_2 and c_3 are initially arbitrary. However, two constraints are imposed on $\delta\hat{\mathbf{A}}_i$ and $\delta\hat{\mathbf{A}}_o$ by the conditions described by Eqs. (5.57)–(5.59). First, since $\delta\hat{\mathbf{A}}_\infty$ and $\delta\hat{\mathbf{A}}_b$ satisfy the same boundary condition on S_p as given by Eqs. (5.8) and (5.17), Eq. (5.57) implies that

$$c_1 + c_2 = 1. \tag{5.66}$$

Next, since $\mathbf{e}_n \times \delta\hat{\mathbf{A}}_b \mid_{S_b} = 0$ from Eq. (5.16), it follows that Eq. (5.58) requires

$$c_1 = c_3. \tag{5.67}$$

The last condition, corresponding to Eq. (5.59), is automatically satisfied since $\delta\hat{\mathbf{A}}_\infty \mid_\infty = 0$ as required by Eq. (5.7). Thus, of the three coefficients—c_1, c_2, and c_3—only one is independent.

Using the properties of the vacuum solutions, one can easily evaluate $\mathcal{L}$ as given by Eq. (5.53). A short calculation yields

$$\begin{aligned}
\mathcal{L} \;=\; & \delta W_F + c_1(c_1+c_2)\delta W_V^{(\infty)} + c_2(c_1+c_2)\delta W_V^{(b)} - \\
& \frac{(c_1^2 - c_3^2)}{2\mu_0} \int_{S_b} (\mathbf{e}_n \times \delta\hat{\mathbf{A}}_\infty) \cdot \mathbf{e}_n \times (\mathbf{e}_n \times \nabla \times \delta\hat{\mathbf{A}}_\infty)\, dS - \\
& \frac{c_1 c_2}{2\mu_0} \int_{S_b} (\mathbf{e}_n \times \delta\hat{\mathbf{A}}_\infty) \cdot \mathbf{e}_n \times (\mathbf{e}_n \times \nabla \times \delta\hat{\mathbf{A}}_b)\, dS + \\
& \frac{c_1 \gamma\sigma d}{2} \int_{S_b} |\mathbf{e}_n \times \delta\hat{\mathbf{A}}_\infty|^2\, dS.
\end{aligned} \tag{5.68}$$

This expression can be simplified by eliminating c_1 and c_3 in terms of c_2 by means of Eqs. (5.66) and (5.67) and making use of the identity

$$\nabla \cdot (\delta\hat{\mathbf{A}}_\infty \times \nabla \times \delta\hat{\mathbf{A}}_b + \delta\hat{\mathbf{A}}_b \times \nabla \times \delta\hat{\mathbf{A}}_\infty) = 0. \tag{5.69}$$

Upon integrating Eq. (5.69) over the V_i, one obtains

$$\begin{aligned}
& \int_{S_b} (\mathbf{e}_n \times \delta\hat{\mathbf{A}}_\infty) \cdot \mathbf{e}_n \times (\mathbf{e}_n \times \nabla \times \delta\hat{\mathbf{A}}_b)\, dS = \\
& \quad - \int_{S_b} (\mathbf{e}_n \times \delta\hat{\mathbf{A}}_b) \cdot \mathbf{e}_n \times (\mathbf{e}_n \times \nabla \times \delta\hat{\mathbf{A}}_\infty)\, dS.
\end{aligned} \tag{5.70}$$

Since $\mathbf{e}_n \times \delta\hat{\mathbf{A}}_\infty \mid_{S_b} = \delta\hat{\mathbf{A}}_b \mid_{S_b}$, it follows that

$$\int_{S_b} (\mathbf{e}_n \times \delta\hat{\mathbf{A}}_\infty) \cdot \mathbf{e}_n \times (\mathbf{e}_n \times \nabla \times \delta\hat{\mathbf{A}}_b)\, dS =$$

$$2\mu_0(\delta W_b - \delta W_\infty) > 0. \tag{5.71}$$

Substituting these results into Eq. (5.68) leads to

$$\mathcal{L} = \delta W_\infty + c_2^2(\delta W_b - \delta W_\infty) + \frac{\sigma\gamma d(1-c_2)}{2} \int_{S_b} |\mathbf{e}_n \times \delta\hat{\mathbf{A}}_\infty|^2\, dS. \tag{5.72}$$

Observe that $\mathcal{L}$ is a simple quadratic equation in terms of the variational parameter c_2. It is now straightforward to determine c_2 by setting $\frac{\partial \mathcal{L}}{\partial c_2} = 0$. The resulting value of c_2 is substituted back into $\mathcal{L}$ which is then set to zero. The equation $\mathcal{L} = 0$ can be solved for the growth rate γ yielding

$$\gamma\tau_D = -\frac{\delta W_\infty}{\delta W_b}, \tag{5.73}$$

where, as usual,

$$\tau_D = \mu_0 \sigma d \bar{b}, \tag{5.74}$$

and $\bar{b}$ is explicitly written

$$\bar{b} = \frac{\frac{1}{2\mu_0}\int_{S_b} |\mathbf{e}_n \times \delta\hat{\mathbf{A}}_\infty|^2\, dS}{(\delta W_b - \delta W_\infty)}, \tag{5.75}$$

$$= \frac{\int_{S_b} |\mathbf{e}_n \times \delta\hat{\mathbf{A}}_\infty|^2\, dS}{\int_{S_b} (\mathbf{e}_n \times \delta\hat{\mathbf{A}}_\infty) \cdot \mathbf{e}_n \times (\mathbf{e}_n \times \nabla \times \delta\hat{\mathbf{A}}_b)\, dS}. \tag{5.76}$$

The expression in Eq. (5.73) represents a generalization of the result originally derived by Freidberg for the circular RFP [74].

Equations (5.73)–(5.76) provide an accurate estimate of the resistive wall growth rate in terms of the properties of the ideal system with a perfectly

conducting wall. An important conclusion from Eq. (5.73) is that a system which is unstable with a wall at infinity $\delta W_\infty < 0$ but stable with a perfectly conducting wall near the plasma $\delta W_b > 0$ will always be unstable to a slow growing mode if the wall is resistive. The characteristic growth time is comparable to the resistive diffusion time through the wall.

A subtle point is the following. The trial functions that minimize δW with the wall at infinity and at S_b are not in general identical. However, the analysis assumes the same trial function for both cases. In practice the differences in $\xi(S_p)$ are not large. Still, to the extent possible, one should choose a trial function most closely related to δW_∞ when considering marginal stability. For growth rate problems it is desirable, in principle, to calculate γ by two methods—one with $\xi(S_p)$ corresponding to δW_∞ and the other with $\xi(S_p)$ corresponding to δW_b—and to then select the fastest growth rate.

5.4 Non-Ideal Effects on Resistive Wall Instabilities

The analysis just presented shows that a resistive wall leads to slowly growing modes with zero real frequency. It has been argued that the addition of non-ideal effects into the plasma model may cause the natural modes of the system to develop a real part in the frequency. In this situation, the resistive wall must respond to an AC signal. If the frequency is high enough so that the skin depth is smaller than the wall thickness, the resistive wall would behave as a perfect conductor; wall stabilization would persist even in the presence of a resistive wall. Finite Larmor radius (FLR) and plasma rotation are two such effects which produce a real frequency for unstable ideal MHD modes.

This appealing argument does not apply to resistive wall instabilities. To show, this consider the analysis of Pearlstein and Freidberg [75] who derived the following variational principle for MHD stability including FLR and plasma rotation in arbitrary near θ pinch geometry.

$$\mathcal{L} = \delta W - \frac{1}{2}\int_{V_p} \rho \xi_\perp \cdot \mathbf{D} \cdot \xi_\perp \, dV. \tag{5.77}$$

Here, $\xi_\perp$ must satisfy $\nabla \cdot \xi_\perp = 0$ and $\mathbf{D}$ is given by

$$\mathbf{D} = \begin{pmatrix} T & i(T-\omega^2)/m \\ -i(T-\omega^2)/m & T \end{pmatrix}, \tag{5.78}$$

where m is the dominant poloidal harmonic mode number and

$$T = (\omega - m\Omega)\left[\omega - m(\Omega + \Omega_{*i}) - \frac{\beta}{2} m\Omega_{*i}\right]. \tag{5.79}$$

$\Omega_{*i} = -(1/enrB)(dp_i/dr)$ is the ion diamagnetic drift velocity representing FLR effects and Ω represents the rotation velocity of the plasma. For ideal MHD $\Omega = \Omega_{*i} = 0$ and $T = \omega^2$

The critical point to recognize is that the new effects enter the calculation as modifications to the inertia term. Thus, if one again considers slowly growing modes, $|\omega| \sim 1/\tau_D \ll \gamma_{MHD}$ then FLR and rotational effects are unimportant if

$$\Omega_{*i}/\tau_D \ll \gamma^2_{MHD}, \tag{5.80}$$

$$\Omega/\tau_D \ll \gamma^2_{MHD}. \tag{5.81}$$

Specifically, when Eqs. (5.80) and (5.81) are satisfied, as they are in most practical applications, FLR and rotational effects modify T from its ideal value

$$T = \omega^2 \sim 1/\tau_D^2 \approx 0 \tag{5.82}$$

to

$$T \approx m^2\Omega[\Omega + (1+\beta/2)\Omega_{*i}], \tag{5.83}$$

that is, FLR and rotation produce small corrections to the potential energy δW but do not modify the frequency dependence of the eigenvalue problem.

The situation is summarized in Fig. 5.2 where we have illustrated typical spectral plots for the systems under discussion. Figure 5.2a shows the situation with the wall at infinity predicting instability ($\mathrm{Im}\,\omega > 0$). In Fig. 5.2b an ideal perfectly conducting wall is brought close to the plasma providing wall stabilization ($\mathrm{Im}\,\omega = 0$). Figure 5.2c shows the effect of substituting a resistive wall in place of the ideal wall. The ideal wall stabilized modes become slightly damped ($\mathrm{Im}\,\omega < 0$). This is the "AC wall stabilization" previously discussed. However, a new, purely growing unstable mode develops out of the origin ($\mathrm{Im}\,\omega > 0$), corresponding to the resistive wall instability.

The conclusion is that FLR effects and plasma rotation do not produce any significant modification to resistive wall instabilities. A similar conclusion applies to electron diamagnetic effects characterized by the parameter $\omega_{*e} = m\Omega_{*e}$, although for a different reason; that is, since unstable ideal MHD modes satisfy $E_{\|} = 0$, parallel electron dynamics do not play an important role. Hence, ω_{*e} does not effect ideal MHD instabilities. However, for resistive tearing modes, which depend sensitively on $E_{\|} = \eta J_{\|} \neq 0$, parallel electron dynamics play an important role, causing a real part to the frequency of order $\mathrm{Re}\,\omega \sim \omega_{*e}$. For these modes, AC wall stabilization should be an important stabilizing influence.

5.5 Axisymmetric Stability of the Straight Tokamak

As an application of the preceding analysis, we will consider the stability of tokamaks against axisymmetric ($n = 0$) MHD modes. First, ideal stability boundaries will derived by assuming the presence of a concentric perfectly conducting wall surrounding the plasma. These results are will be used in

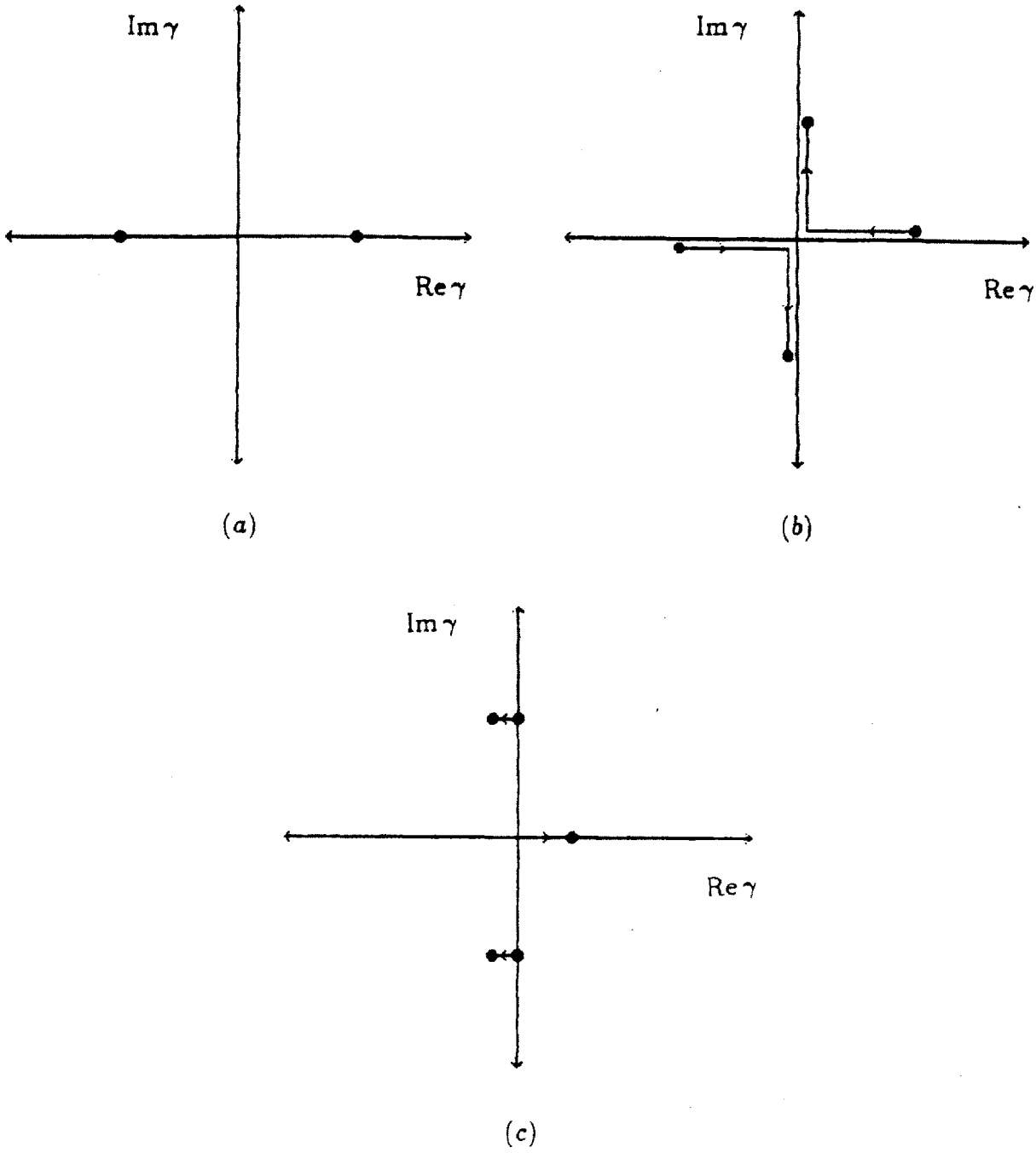

Figure 5.2: *Spectral behavior of Resistive Wall Instabilities: (a) wall at infinity, (b) perfectly conducting wall nearby, (c) resistive wall nearby.*

Eqs. (5.73)–(5.76) to calculate the growth rate of modes driven unstable by the presence of a resistive wall. The question of how much passive stabilization can be expected from resistive vacuum vessels is a particularly important problem since several current or proposed experimental devices are characterized by relatively large plasma elongations and discharge times. The size of the passive growth rate resulting from a given vessel configuration gives an estimate of the requirements for an active feedback system or additional passive stabilizers needed to keep the plasma position within acceptable bounds. The details of this more complicated problem will be addressed in the next chapter.

A number of assumptions will be made to simplify the analysis. First, to enable the analytic solution for the vacuum magnetic fields, we will consider stability only in the straight ($\epsilon \to 0$) limit. Second, to allow the neglect of the Shafranov shift of the flux surfaces, we will assume low beta ($p \to 0$) operation. Finally, to reduce the complexity of the energy integrals, we will take

$$\xi = \xi_Z \mathbf{e}_Z \tag{5.84}$$

(where ξ_Z is assumed constant) as our trial function for the plasma displacement.

The ideal vertical stability of the straight elliptical tokamak with a flat current density profile has been studied by several authors [17–21]. The additional effects of a specific peaked current density profile and finite beta were modeled by Laval and Pellat [76] and Haas [19] respectively. Wesson [71] included the effect of a resistive wall while retaining the assumption of a flat current density profile. Here, we extend these analyses to include the effects of arbitrary current density profiles and a resistive wall.

The ideal stability of triangular plasmas was originally studied by Rebhan [77]. Later, Ramos [78] examined the effects of combined elongation and

triangularity. Here, we extend these results to include the effect of a resistive wall.

5.5.1 Formulation

The analysis to be presented here is analogous to that required to apply the Extended Energy Principle. First, the equilibrium fields are used to compute the fluid energy δW_F. Second, the fields in the vacuum are solved for by choosing a convenient parameterization for the shape of the resistive wall. Third, the vacuum fields are used to evaluate $\delta W_V^{(b)}$ and $\delta W_V^{(\infty)}$. Finally, the minimum plasma-wall separation to ensure stability and an estimate for the resistive wall growth rate will be calculated.

Calculation of Fluid Energy

In the case of the rigid vertical shift, δW_F [Eq. (5.2)] takes on the particularly compact form

$$\delta W_F = \frac{\xi_Z^2}{2\mu_0} \int_{S_p} (\mathbf{e}_n \cdot \mathbf{e}_Z)(\mathbf{B} \cdot \nabla(\mathbf{e}_Z \cdot \mathbf{B}))\, dS. \tag{5.85}$$

For consistency with the variational equilibrium formulation, we will use Eqs. (3.34) and (3.35) to parameterize the plasma surface:

$$R(\mu) = R_0 + a(\cos\mu - \delta_a \sin^2\mu), \tag{5.86}$$

$$Z(\mu) = a\kappa_a \sin\mu, \tag{5.87}$$

where μ is the usual angular coordinate and $a \ll R_0$. Rewriting Eq. (5.85) in terms of this parameterization, taking the straight limit, and integrating by parts gives

$$\delta W_F = -\frac{\pi \xi_Z^2 R_0 W_F}{\mu_0}, \tag{5.88}$$

where the quantity W_F has the form

$$W_F \equiv \int_0^{2\pi} \left[\frac{R_\mu Z_{\mu\mu} - Z_\mu R_{\mu\mu}}{Q^2} \right] B_p^2 \, d\mu. \tag{5.89}$$

W_F is computed for specific choices of geometry later.

Calculation of Vacuum Energy: Perfectly Conducting Wall

Due to the rigid vertical shift assumption, the vacuum energy [Eq. (5.14)] takes on a simple form as well

$$\delta W_V^{(b)} = \frac{\xi_Z}{2\mu_0} \int_{S_p} (\mathbf{e}_n \cdot \mathbf{e}_Z)(\mathbf{e}_t \cdot \delta\hat{\mathbf{B}}) B_p \, dS. \tag{5.90}$$

To evaluate $\delta W_V^{(b)}$ it is necessary to solve for $\delta\hat{\mathbf{B}}$ in the vacuum region between the plasma and the wall (here assumed to be perfectly conducting). Even in the straight limit, this is generally a difficult task due to the complexity of Eq. (5.15). However, if attention is focused on a special class of wall shapes, Eq. (5.15) can be transformed into a very simple form and solved analytically.

This transformation is accomplished by introducing the following vacuum coordinate system [78]:

$$\begin{aligned} R(u,\mu) &= R_0 - \frac{\delta_a a}{2} + a' \Bigg(\sinh u \cos\mu + \\ &\qquad \frac{\delta_a}{2} \sinh u_a \cosh[2(u-u_a)] \cos 2\mu \Bigg), \end{aligned} \tag{5.91}$$

$$\begin{aligned} Z(u,\mu) &= a' \Bigg(\cosh u \sin\mu + \\ &\qquad \frac{\delta_a}{2} \sinh u_a \sinh[2(u-u_a)] \sin 2\mu \Bigg), \end{aligned} \tag{5.92}$$

where, by comparison with Eqs. (5.86) and (5.87), it is seen that $u = u_a$ parameterizes the plasma surface if

$$u_a = \coth^{-1} \kappa_a, \tag{5.93}$$

$$a' = a/\sinh u_a. \tag{5.94}$$

For the sake of convenience, it will be assumed that the wall surface also lies on a constant-u surface: specifically, $u = u_b$ where $u_b > u_a$. Examples of the wall shapes produced by this parameterization are shown in Fig. 5.3. In the figure, the plasma-wall separation is labeled using the quantity (originally suggested by Haas [19])

$$t \equiv e^{2(u_a - u_b)}. \tag{5.95}$$

Note that t is related to the ratio of the cross-sectional area of the plasma to the area enclosed by the wall. Hence, $t = 1$ corresponds to the wall lying on the plasma surface while $t = 0$ corresponds to the wall being located at infinity.

In the above coordinate system Eq. (5.15) simplifies to

$$\frac{\partial^2 \delta \hat{A}_{b\varphi}}{\partial u^2} + \frac{\partial^2 \delta \hat{A}_{b\varphi}}{\partial \mu^2} = 0 \tag{5.96}$$

and the boundary conditions [Eqs. (5.16) and (5.17)] become

$$\delta \hat{A}_{b\varphi} \mid_{u_a} = \frac{\xi_z R_\mu B_p}{Q}, \tag{5.97}$$

$$\delta \hat{A}_{b\varphi} \mid_{u_b} = 0. \tag{5.98}$$

Since, Eq. (5.96) is simply Laplace's equation in "rectangular" coordinates, it can be solved analytically using standard Fourier analysis techniques. These methods give

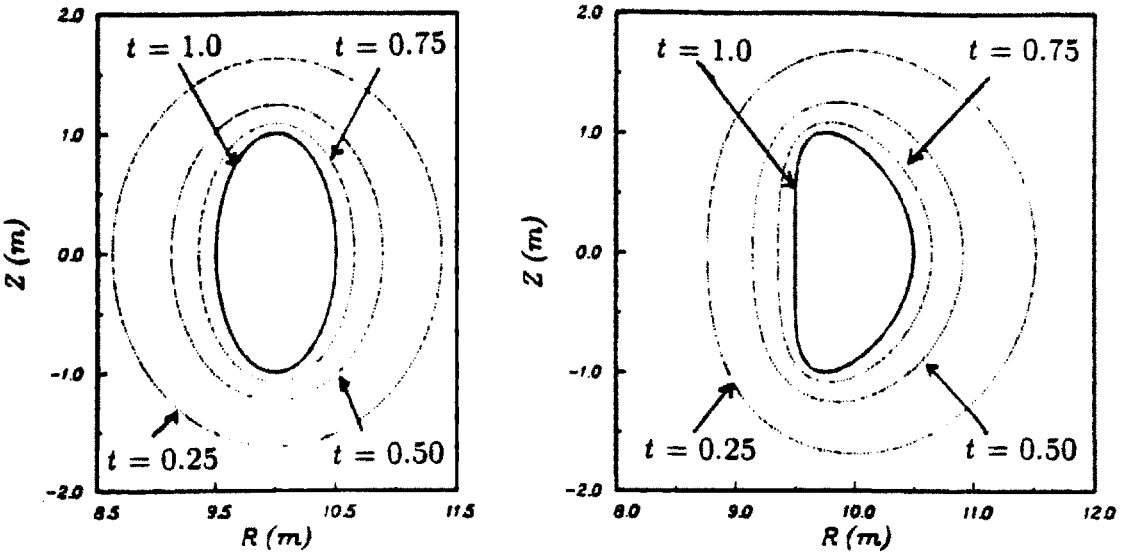

(a) (b)

Figure 5.3: *Wall geometry as function of Haas position parameter.*

$$\delta \hat{A}_{b\varphi} = \xi_Z \sum_{m=1}^{\infty} \frac{\sinh[m(u-u_b)]}{\sinh[m(u_a-u_b)]} W_{Vm} \sin m\mu, \tag{5.99}$$

where

$$W_{Vm} = \frac{1}{\pi} \int_0^{2\pi} R_\mu \frac{B_p}{Q} \sin m\mu \, d\mu. \tag{5.100}$$

Equation (5.99) can be substituted into Eq. (5.90) to finally obtain

$$\delta W_V^{(b)} = \frac{\pi^2 \xi_Z^2 R_0}{2\mu_0} \sum_{m=1}^{\infty} m W_{Vm}^2 \frac{1+t^m}{1-t^m}. \tag{5.101}$$

Calculation of Vacuum Energy: No Wall

By a very similar set of calculations, it is straightforward to analyze the case where no wall is present. We find

$$\delta \hat{A}_{\infty\varphi} \mid_{u_b} = \xi_Z \sum_{m=1}^{\infty} t^{m/2} W_{Vm} \sin m\mu, \tag{5.102}$$

$$\delta W_V^{(\infty)} = \frac{\pi^2 \xi_Z^2 R_0}{2\mu_0} \sum_{m=1}^{\infty} m W_{Vm}^2. \tag{5.103}$$

5.5.2 Stability of the Straight Ellipse

The straight elliptical tokamak has been extensively studied because its simple geometry allows many calculations to be performed analytically. That will prove to be the case here as well. Recall from Chapter 3 that five variational coefficients — κ_0 (central elongation), σ (shift), η (triangularity variation), ν (flux shape), and ψ_0 (flux normalization) — were defined. For the purposes of considering vertical stability of the straight ellipse only κ_0 enters into the calculations. This is because $\sigma \approx 0$ by virtue of the assumption of zero beta, $\eta = 0$ identically due to the elliptical plasma boundary, and ν and ψ_0 will be shown to scale out of the problem.

On the basis of the above observations, it is possible to write

$$B_p/Q \mid_{s_p} = \frac{1}{R_0(1 + 2\lambda \sin^2 \mu)} \frac{d\psi}{d\rho}(1) \tag{5.104}$$

to a very good approximation. In Eq. (5.104), the parameter λ is defined

$$\lambda \equiv \frac{\kappa_a - \kappa_0}{\kappa_a}. \tag{5.105}$$

By considering a number of ePFC equilibria run with the parameters shown in Table 5.1, it is possible to associate large values of λ with peaked current density profiles. This is seen in Fig. 5.4 which shows that λ is a monotonically decreasing function of the normalized current profile width

Table 5.1: *ePFC Input Parameters for Straight Ellipse*

Parameter	Value
b_p	0.001
$a\,(\mathrm{m})$	0.5
$R_0\,(\mathrm{m})$	10.0
$B_0\,(\mathrm{T})$	3.14
$I_p\,(\mathrm{MA})$	1.0

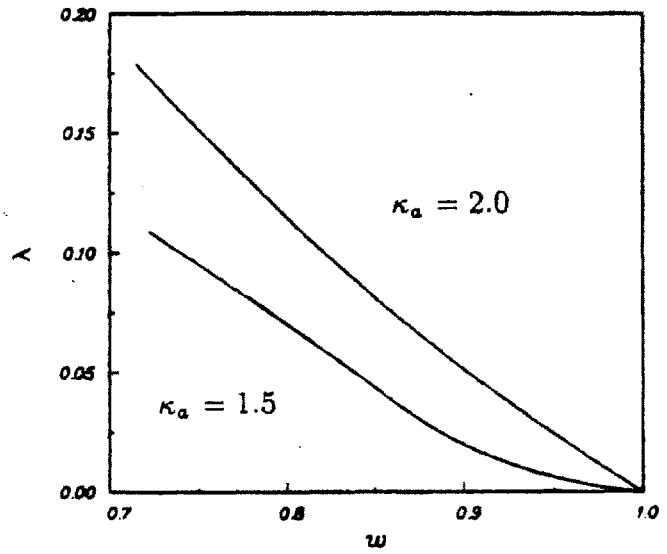

Figure 5.4: *Plot of λ vs. w for straight ellipse.*

$$w \equiv \left[\frac{I_p}{\pi a^2 \kappa_a J_\varphi(0)}\right]^{1/2}. \tag{5.106}$$

Using Eq. (5.104), it is possible to calculate δW_F, $\delta W_V^{(b)}$, $\delta W_V^{(\infty)}$, $\delta \hat{A}_{\infty\varphi}\,|_{u_b}$ in terms of λ

$$\delta W_F = -\frac{\pi^2 \xi_Z^2}{\mu_0 a^2 R_0 \kappa_a}\left[\frac{d\psi}{d\rho}(1)\right]^2\left[\frac{1+\lambda}{(1+2\lambda)^{3/2}}\right], \tag{5.107}$$

$$\delta W_V^{(b)} = \frac{4\pi^2 \xi_Z^2}{\mu_0 a^2 R_0 \kappa_a^2 (1+2\lambda+\sqrt{1+2\lambda})^2}\left[\frac{d\psi}{d\rho}(1)\right]^2\left[\frac{1+t}{1-t}\right], \tag{5.108}$$

$$\delta W_V^{(\infty)} = \frac{4\pi^2 \xi_Z^2}{\mu_0 a^2 R_0 \kappa_a^2 (1+2\lambda+\sqrt{1+2\lambda})2}\left[\frac{d\psi}{d\rho}(1)\right]^2, \tag{5.109}$$

$$\delta \hat{A}_{\infty\varphi}\,|_{u_b} = \frac{2\xi_Z t^{1/2}\sin\mu}{a R_0 \kappa_a (1+2\lambda+\sqrt{1+2\lambda})}\left[\frac{d\psi}{d\rho}(1)\right]. \tag{5.110}$$

Note that in Eqs. (5.108) and (5.109) only the $m = 1$ term of the sum in Eq. (5.101) was kept due to the fast convergence of that series.

Marginal Position for Perfectly Conducting Wall

We will now derive a condition giving the maximum distance a perfectly conducting wall can be placed while still ensuring at least marginal stability. This is found by setting $\delta W_b = 0$ and solving for t. The result is

$$t > \frac{\kappa_a G(\lambda) - 1}{\kappa_a G(\lambda) + 1}, \tag{5.111}$$

where $G(\lambda)$ is a monotonically increasing function of λ defined

$$G(\lambda) = \frac{1+\lambda}{4(1+2\lambda)^{3/2}}\left(1+2\lambda+\sqrt{1+2\lambda}\right)^2. \tag{5.112}$$

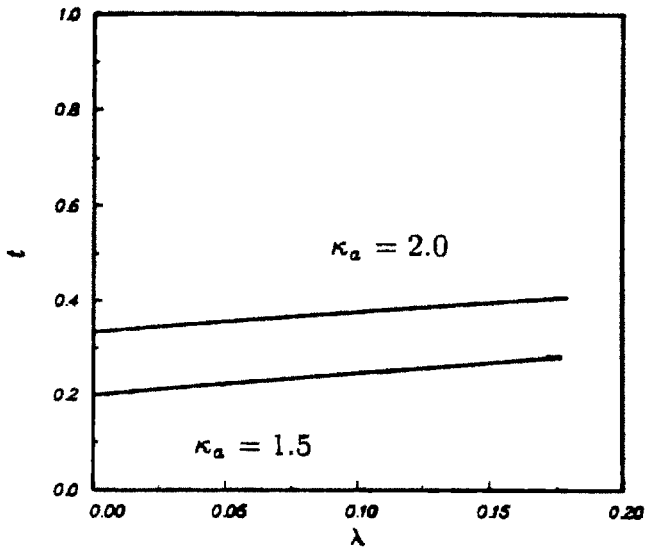

Figure 5.5: *Plot of marginal Haas position vs. λ for straight ellipse.*

As previously mentioned, the marginal wall position in Eq. (5.111) does not depend explicitly on the shape of the flux function. Instead, the axisymmetric stability of the straight ellipse is only a function of the topology of the flux surfaces as specified by κ_a and λ

Equations (5.111)–(5.112) extend the results of Laval and Pellat [76] to arbitrary current density profile. In the limit $\lambda \to 0$ the flat profile result obtained by Haas [19] is recovered. For non-zero values of λ, corresponding to peaked current density profiles, $G(\lambda)$ represents an effective enhancement of the plasma elongation. Figure 5.5 shows that elongation represents a destabilizing factor for the straight ellipse since the marginal wall position moves closer to the plasma as elongation increases. Hence, the peaking of current profiles represents a destabilizing effect as well. This result is reasonable on physical grounds since the peaking of the current profile effectively moves the plasma current farther away from the stabilizing effects of the wall.

Growth Rate Estimate for Resistive Wall

If a configuration with a perfectly conducting wall satisfies the stability condition given in Eq. (5.111), the substitution of a resistive wall results in a mode growing at a rate given by Eq. (5.73). Using Eqs. (5.104)–(5.110) in Eqs. (5.73)–(5.75) leads to a simple analytic expression for the growth rate

$$\gamma\tau_D = -\frac{2}{\mu_0\sigma\hat{b}d}\frac{(\kappa_a G(\lambda)-1)}{(1-t)\kappa_a G(\lambda)-(1+t)}, \tag{5.113}$$

where

$$\hat{b} = \frac{b}{\pi}\int_0^{2\pi}\sin^2\mu\sqrt{\kappa_b^2\cos^2\mu+\sin^2\mu}, \tag{5.114}$$

and $b = a\sinh u_b/\sinh u_a$ is the minor radius of the wall and $\kappa_b = \coth u_b$ is the elongation of the wall.

Note from Eq. (5.113) that as t approaches its marginal position γ approaches infinity. This is a consequence of the neglect of plasma inertial effects in Eq. (5.26). Neglecting plasma inertia is formally accomplished by letting the plasma mass density ρ approach zero. In this limit, the Alfvén velocity $v_A \propto 1/\rho^{1/2} \rightarrow \infty$ hence the $\gamma_{MHD} \rightarrow \infty$.

Consider again the plasmas specified by Table 5.1. Assuming a 0.025 m thick stainless-steel wall located at $t = 0.45$, it is possible to use Eq. (5.113) to construct a plot of γ as a function of λ for various plasma elongations. This is shown in Fig. 5.6. Note that while peaking the current profile has a relatively small effect on the condition for marginal stability, it can substantially increase the growth rates of passively stabilized axisymmetric modes, especially at larger elongations.

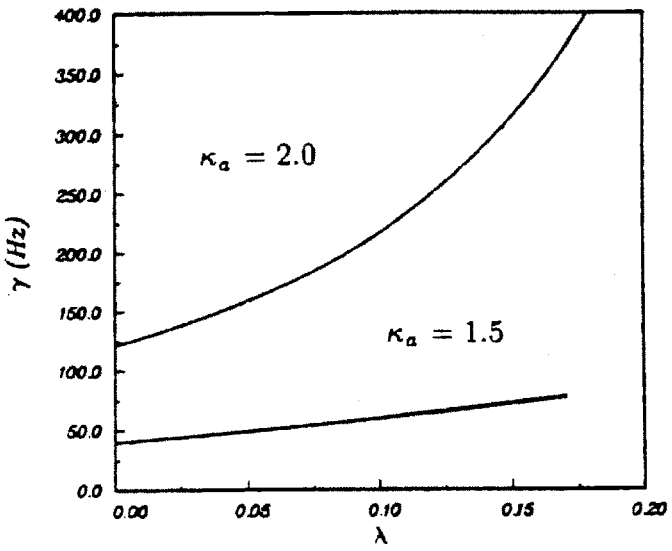

Figure 5.6: *Plot of γ vs. λ for straight ellipse.*

5.5.3 Stability of the Straight Dee

Unlike the straight ellipse, the geometry of the straight dee-shaped tokamak is sufficiently complicated so as to make analytic evaluation of δW_F, $\delta W_V^{(b)}$, $\delta W_V^{(\infty)}$, $\delta \hat{A}_{\infty\varphi}\,|_{u_b}$ unwieldy. However, these quantities can be numerically calculated in a straightforward manner for plasmas characterized by the parameters in Table 5.1 and substituted into Eqs. (5.73)–(5.76) to yield Fig. 5.7. This plot shows the variation in γ with δ_a for a $\kappa_a = 2$ plasma with a flat current density profile ($\alpha_J = -25.0$). The resistive wall is again assumed to be 0.025 m thick stainless-steel located at $t = 0.45$. It should be noticed that triangularity appears to have a strong stabilizing influence. This is consistent with the ideal results of Rebhan [77] and Ramos [78] who found that triangular plasmas possess larger marginal plasma-wall distances than elliptical plasmas.

Also shown on Fig. 5.7 is the curve obtained from Eqs. (5.73)–(5.76) in the case when the B_p used in Eqs. (5.85) and (5.90) is that from NEQ rather than

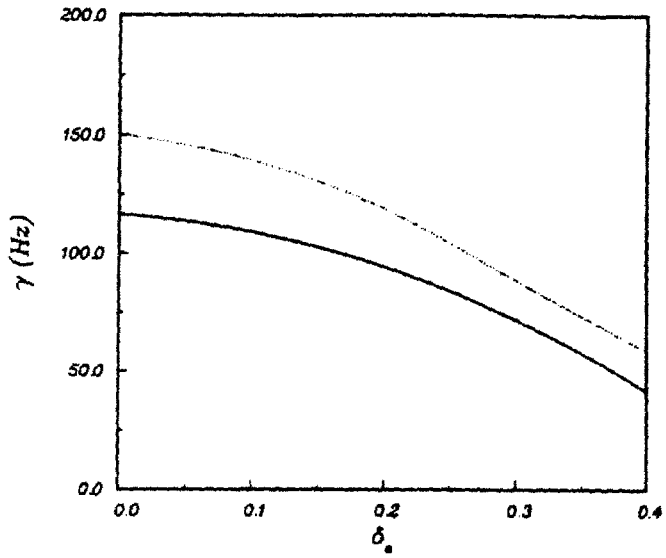

Figure 5.7: *Plot of γ vs. δ_a for straight dee.*

ePFC. Notice that the resulting growth rates agree relatively well. This is a consequence of the fact that $\delta W_{F,V} \propto B_p^2$. Hence, the regions of low field near the separatrix where the field error for the ePFC equilibrium is the greatest (see Fig. 3.12) contribute the least to the energy integrals. This supports the contention made in Chapter 3 that the calculation of axisymmetric stability is not greatly affected by inaccuracies in the equilibrium.

Chapter 6

Vertical Stability of Tokamaks in the Presence of Resistive Conductors and Feedback

Many currently operating and proposed tokamaks are characterized by relatively large plasma elongations. For instance, the JET tokamak at Culham Laboratory in the United Kingdom regularly operates at $\kappa_a = 1.6$ and the DIII-D tokamak at GA Technologies, Inc. has achieved elongations as high as $\kappa_a = 2.1$. Also, the proposed Alcator C-Mod ($\kappa_a = 1.8$), CIT ($\kappa_a = 2.0$), and ITER ($\kappa_a = 2.3$) designs all feature large plasma elongations.

As the analysis in Chapter 2 demonstrated, large plasma elongations are desirable to maximize performance in tokamak reactors by raising the β_t value allowed by the Troyon limit [Eq. (2.27)] and, hence, the amount of fusion power generated by a plasma of given dimensions. Since ITER is a design for an engineering test reactor, this reasoning provides motivation for the large elongation for that proposed device. For the case of CIT, an

experiment designed to demonstrate ignited tokamak operation, the large elongation also results from a desire to raise β_t. However, in this case, the goal is to minimize the τ_E required for ignition. This possibility was demonstrated in Chapter 1 by the scaling argument that led to Eq. (1.9).

Large values of κ_a do, however, have a major drawback. Namely, elongated plasmas are usually found to be unstable to axisymmetric MHD modes [16]. This point was illustrated in the previous chapter when it was shown that, lacking a close perfectly conducting wall, elliptical plasmas with $\kappa_a > 1$ are unstable on the ideal MHD timescale to rigid displacements. This is also the case for more realistic plasma geometries despite the stabilizing effects of increasing triangularity (see Fig. 5.7) and increasing inverse aspect ratio (see Ref. [77]). Furthermore, it was also shown in the previous chapter that the wall stabilization phenomenon, even in the presence of FLR effects and plasma rotation, is not sufficient to completely stabilize the axisymmetric modes when wall resistivity is taken into account. In particular, the modes were shown to be unstable with a growth rate $\gamma \sim \frac{1}{\tau_D} \ll \gamma_{MHD}$.

Despite the fact that axisymmetric modes grow on a timescale slow from the point of view of ideal MHD theory, this instability cannot be tolerated in either experiments or reactors since τ_D is almost always much shorter than the desired discharge lifetime. Hence, special techniques must be employed to control axisymmetric modes. For virtually all tokamaks, these techniques consist of the use of passive conductors [72] to slow down the modes and feedback [79] to stabilize them.

The idea of passive stabilization is easily explained. When the plasma moves due to an axisymmetric instability, toroidal currents can be induced in nearby conductors. If the conductors are judiciously located, the resulting induced field can provide a restoring force acting to retard the plasma's motion. The net restoring force due to several conductors can significantly reduce the growth rate of the instability. However, it is important to note that no matter how many passive stabilizers are employed, they will never

completely stabilize the mode. This is because the induced currents decay on a timescale related to the L/R time of the conductors where L is the conductor inductance and R is the conductor resistance. Since this time is also close to the timescale of the instability, the stabilizing currents eventually vanish and the mode continues to grow.

Feedback techniques consist of actively driving currents in one or more PF coils to provide restoring forces which retard the motion of the plasma. These currents are usually directly based on plasma position measurements and are programmed so as to exert the maximum favorable force on the plasma. Furthermore, since the currents are driven by an external power source they do not decay. Therefore, as one might expect, this method is quite effective in controlling axisymmetric instabilities. In fact, unlike passive techniques, feedback can be used to completely stabilize axisymmetric modes. This capability has been very successfully demonstrated in several studies [80–84].

Based on the success of feedback techniques for the purpose of controlling axisymmetric modes, one might be tempted to suggest that similar methods be used to control other MHD instabilities. This is quickly seen to be infeasible from a practical viewpoint. Specifically, the axisymmetric instability can be controlled so well because it represents a single mode with a very simple mode structure. As such, the controlling apparatus, consisting merely of a series of axisymmetric loops and sensors, is simple as well. This would not be the case with $n \neq 0$ modes. The plasma displacement would have to be sensed at several toroidal locations and the stabilizing coils would have to be formed into a helical shape reflecting the toroidal mode number. Even worse, one could not be guaranteed that only one n-number would be excited so feedback systems for each n would have to be constructed. This is clearly an undesirable task so, in general, we must assume that all MHD modes other than the axisymmetric mode are at least marginally stable with a wall at infinity.

Due to the widespread use of large plasma elongations to improve β_t, the problem of analyzing axisymmetric stability in the presence of active and passive stabilization is an important one. However, it is also relatively complicated since it is necessary to simultaneously model the effects of the plasma, the PF coils, the OH coils, the resistive vacuum chamber wall, and the feedback loops and sensors.

A number of approaches have been employed for studying the tokamak axisymmetric stability problem. One of the most common and physically appealing methods represents all elements of the system, including the plasma, as a series of wire loops [72,84,85,86]. As a result, the coupling between the plasma, the vacuum chamber wall, and the various coils can be easily modeled using a series of easily derivable circuit equations. In addition, the stability of the system can be considered by analyzing the normal mode version of the linearized force equations for the loops representing the plasma. The major advantage of this technique is its speed; relatively accurate estimates of growth rates and feedback system requirements for complicated wall and coil geometries can be computed very quickly and inexpensively. For this reason, this method has been used extensively in the design of the Alcator C-Mod experiment [86]. The major disadvantage of this approach is its relatively primitive plasma model. Representing the plasma with wire loops results in the neglect of such important effects as plasma beta and flux conservation. Also, the wire loop model is largely limited to modeling rigid vertical plasma displacements.

At the other end of the computational spectrum is a computer code named TSC developed by Jardin, *et al.* [87] at Princeton Plasma Physics Laboratory. This extremely elaborate code calculates the time evolution of a plasma in the presence of very complicated feedback systems and passive conductor geometries. It also self-consistently includes the effects of plasma resistivity and transport. The major advantage of this code is its generality; it can be used to accurately analyze the axisymmetric stability properties of virtually

any tokamak configuration. The major disadvantage of TSC is its complexity and cost. For example, typical TSC runs require *hours* of Cray CPU time to complete.

For many applications, it might be desirable to have a method for solving the tokamak axisymmetric stability problem that incorporates more physics than does the wire loop model but, at the same time, is faster and simpler to use than TSC. One possibility is to use a standard ideal MHD stability code such as GATO [88] or PEST [46,47] to compute values of δW_∞ and δW_b for use in Eq. (5.73). Since the exact eigenfunctions would be employed in the calculation, the resulting growth rate would be expected to be quite accurate. However, there are two drawbacks to this method. First, Eq. (5.73) along with GATO or PEST cannot model the effects of discrete coils or feedback. Second, GATO and PEST are quite general codes able to compute stability for $n \neq 0$ modes. This generality is not required for the axisymmetric stability calculation and, in particular, large increases in computational speed can be achieved by exploiting the axisymmetry of the mode.

In this chapter, we will describe a method for quickly and easily analyzing axisymmetric tokamak stability in the presence of active and passive stabilization. In this method, all of the PF/OH coils along with the vacuum chamber wall and any passive conductors will be modeled using resistive wire loops. However, unlike the wire loop model, the plasma will be treated as an ideal MHD fluid. As such, the linear stability of the system will be studied using a Lagrangian very similar to that proposed in the previous chapter. In addition to the realistic plasma model, this method also has the advantage that arbitrary axisymmetric perturbations can be studied. Furthermore, it will be shown that these desirable features can be implemented in a computer program that executes in times comparable to those for the wire loop model.

6.1 Problem Statement

As in previous chapters, we begin with a discussion of the problem to be solved and the quantities to be calculated. The geometry of the system to be considered is shown in Fig. 6.1a which depicts a tokamak plasma whose surface is parameterized by $R = R_p(\mu)$, $Z = Z_p(\mu)$ surrounded by a thin resistive wall of thickness d along with a number of PF coils, OH coils, and passive conductors. The inner surface of the resistive wall is parameterized by $R = R_w(\mu)$, $Z = Z_w(\mu)$.

Using a simple finite-differencing scheme (described in Appendix B) the coil/wall/conductor geometry in Fig. 6.1a can be accurately represented using J circular cross-section conductors, each of radius a_c, located at the points (R_j, Z_j). The resistivity r_j and external self-inductance ℓ_j of each conductor are chosen to reproduce the particular poloidal circuit element the conductor replaces. This configuration is shown in Fig. 6.1b.

We assume that the plasma is initially in equilibrium supported by the steady state (or at least slowly varying) conductor currents I_j. In general, we would expect that the only conductors carrying non-zero currents are those representing PF or OH coils. However, during start-up, it is possible for the vacuum chamber wall to carry substantial eddy currents. These currents could be included in the analysis if desired.

We further assume that the plasma eventually undergoes a displacement $\xi(\mathbf{r}, t)$. This, in turn, causes perturbed currents to flow in the J conductors. For most of the conductors these perturbed currents are produced by inductive effects associated with the motion of the plasma. However, for some, part of the perturbed current is driven by an externally applied feedback voltage δv_j.

The overall goal of the analysis is to calculate the linear growth rate of the displacement γ and the set of perturbed conductor currents δI_j. This

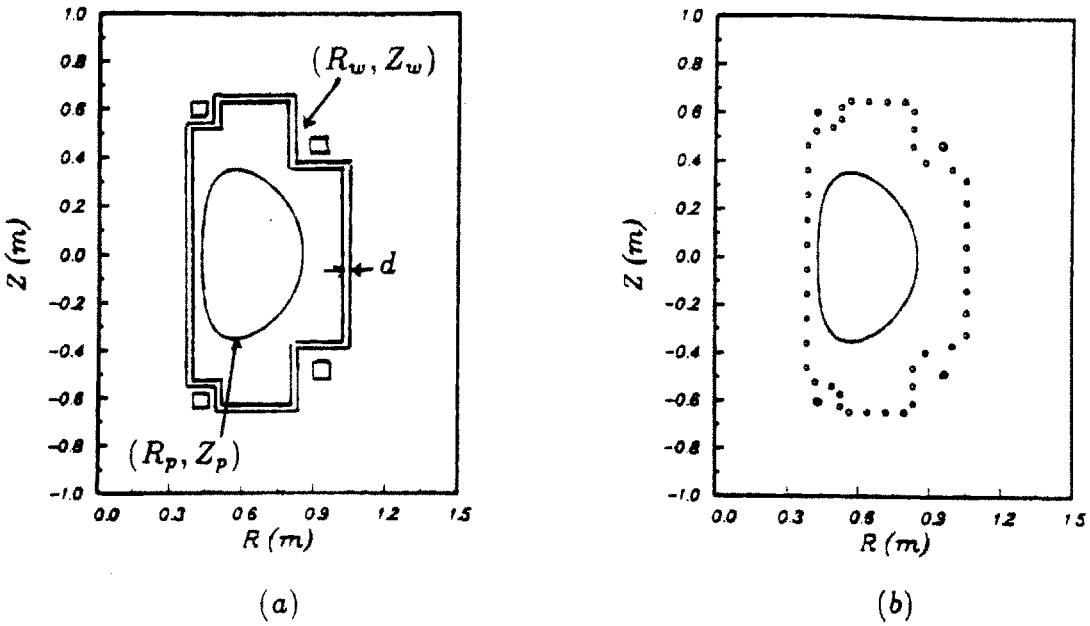

Figure 6.1: *Geometry for axisymmetric stability calculation: (a) original system consisting of plasma, PF/OH coils, passive conductors, and resistive wall and (b) transformed system consisting of plasma and J circular conductors.*

will be accomplished in three parts. First, a Lagrangian describing the dynamics of the plasma will be defined and evaluated in terms of ξ and the δI_j. Second, a series of equations describing the coupling between the plasma and the external conductors will be derived. Finally, all of the relations will be combined to yield a generalized matrix eigenvalue problem which can be solved for γ and the δI_j.

6.2 Lagrangian

In the previous chapter, there was a single timescale — the resistive wall diffusion time τ_D — that characterized the instability. However, in the present problem the situation is much more complicated since each conductor can have a different resistance and inductance and, hence, a different characteristic time. Nevertheless, it is still reasonable to assume that

$$\gamma \ll \gamma_{MHD}. \tag{6.1}$$

If this were not the case, the plasma would be uncontrollable using any realistic feedback system.

Given that the instability is slowly growing, it is again possible to neglect plasma inertial effects. As a result, the linearized equation describing the motion of the plasma is

$$\mathbf{F}(\xi) = 0. \tag{6.2}$$

Hence, in direct analogy with the calculation in the previous chapter, we define the Lagrangian

$$\mathcal{L} \equiv \int_{V_p} \xi \cdot \mathbf{F}(\xi)\, dV = 0, \tag{6.3}$$

and rewrite it in the more familiar form

$$\mathcal{L} = \delta W_F + \delta W_V, \tag{6.4}$$

where

$$\begin{aligned} \delta W_F &= \frac{1}{2}\int_{V_p} \left[\frac{|\delta \mathbf{B}|^2}{\mu_0} - \xi \cdot (\mathbf{J} \times \delta \mathbf{B}) + \Gamma p |\nabla \cdot \xi|^2 + \right. \\ &\qquad \left. (\xi \cdot \nabla p) \nabla \cdot \xi \right] dV, \end{aligned} \tag{6.5}$$

$$\delta W_V = \frac{1}{2}\int_{S_p} (\mathbf{e}_n \cdot \xi) \left(\frac{\hat{\mathbf{B}} \cdot \delta \hat{\mathbf{B}}}{\mu_0} \right) dS. \tag{6.6}$$

6.2.1 Symmetric Form of Lagrangian

Since δW_F and δW_V are energy integrals they must possess certain symmetry properties [59]. However, from Eqs. (6.5) and (6.6) these properties are by no means obvious. Therefore, these relations will be transformed into yet another form to demonstrate this theoretically interesting point. At the same time, it will be seen that the new form has two desirable features. First, it will allow us to readily demonstrate the validity of $\mathcal{L}$ as a variational principle. Second, it will illustrate the conservation of energy in the system.

Symmetric Form of Fluid Energy

The symmetric nature of the fluid energy will be demonstrated using a special form for the displacement. Specifically, we will write

$$\xi(\mathbf{r}, t) = \xi(R)e^{\gamma t}\mathbf{e}_Z, \tag{6.7}$$

where

$$\xi(R) = \sum_{n=1}^{N} a_n f_n(R). \tag{6.8}$$

Note that this particular form was chosen for its applicability to succeeding calculations in this chapter. The properties to be demonstrated are valid for arbitrary ξ.

Since $\nabla \cdot (\xi(R)\mathbf{e}_Z) = 0$ by construction, Eq. (6.5) can be simplified to

$$\delta W_F = \frac{1}{2\mu_0}\int_{V_P} \delta\mathbf{B} \cdot [\delta\mathbf{B} + \mu_0 \xi \times \mathbf{J}]\, dV. \tag{6.9}$$

Furthermore, using Eq. (6.8) along with the expressions

$$\delta\mathbf{B} = \nabla \times (\xi \times \mathbf{B}), \tag{6.10}$$

$$= (\mathbf{B} \cdot \nabla)\xi - (\xi \cdot \nabla)\mathbf{B}, \tag{6.11}$$

$$\nabla(\xi \cdot \mathbf{B}) = \mu_0 \xi \times \mathbf{J} + \mathbf{B} \times (\nabla \times \xi) + (\mathbf{B} \cdot \nabla)\xi + (\xi \cdot \nabla)\mathbf{B}, \tag{6.12}$$

in Eq. (6.9) gives

$$\delta W_F = \mathbf{a} \cdot (\mathbf{V} + \mathbf{S}) \cdot \mathbf{a}, \tag{6.13}$$

where $\mathbf{a}$ is a column vector of length N consisting of the weight coefficients a_n and $\mathbf{V}$ and $\mathbf{S}$ are $(N \times N)$ matrices whose elements are given by

$$V_{mn} = \frac{1}{2\mu_0} \int_{V_P} \left[\left(\frac{df_m}{dR} \right) \left(\frac{df_n}{dR} \right) B_R^2 \right] dV, \tag{6.14}$$

$$\begin{aligned} S_{mn} = & -\frac{\pi}{2\mu_0} \int_0^{2\pi} \frac{RR_\mu Z_{\mu\mu} - Z_\mu (RR_{\mu\mu} + R_\mu^2)}{Q^2} f_m f_n B_p^2 \, d\mu - \\ & \frac{\pi}{\mu_0} \int_0^{\pi} f_m f_n \frac{\partial}{\partial \mu} (RB_R B_Z) \, d\mu. \end{aligned} \tag{6.15}$$

Note that in Eq. (6.15) all quantities are evaluated at the plasma surface. In addition, see from Eqs. (6.14) and (6.15) that $\mathbf{V}$ and $\mathbf{S}$ are symmetric matrices. This is the desired property.

Symmetric Form of Vacuum Energy

To accomplish the transformation of δW_V we note that in the vacuum region surrounding the plasma and the various conductors the perturbed vector potential satisfies the equation

$$\nabla \times \nabla \times \delta \mathbf{A} = 0, \tag{6.16}$$

and that inside each of the conductors it satisfies

$$\nabla \times \nabla \times \delta \mathbf{A} = -\mu_0 \sigma \left(\gamma \delta \mathbf{A} - \frac{\delta v}{2\pi R} \mathbf{e}_\varphi \right). \tag{6.17}$$

Equation (6.17) has been modified from the usual form to include an additional term that accounts for the possibility that a feedback voltage δv may be applied to some of the conductors. For the purposes of this thesis, we will write

$$\delta v\, \mathbf{e}_\varphi = \mathbf{G}(\delta \mathbf{A}). \tag{6.18}$$

In Eq. (6.18), $\mathbf{G}$ is a linear operator that specifies the feedback control law for a conductor in terms of the perturbed vector potential. We will soon see that $\mathbf{G}$ must have self-adjoint property

$$\int_{V_j} \delta \mathbf{A}_1 \cdot \mathbf{G}(\delta \mathbf{A}_2)\, dV = \int_{V_j} \delta \mathbf{A}_2 \cdot \mathbf{G}(\delta \mathbf{A}_1)\, dV \tag{6.19}$$

in order to ensure that $\mathcal{L}$ represents a variational principle. Later in the chapter the exact specification of $\mathbf{G}$ will be discussed.

The boundary conditions corresponding to Eqs. (6.16) and (6.17) are simply

$$\mathbf{e}_n \times \delta \mathbf{A} \mid_{S_p} = -(\mathbf{e}_n \cdot \xi)\mathbf{B} \mid_{S_p}, \tag{6.20}$$

$$\delta \mathbf{A} \mid_{\infty} = 0, \tag{6.21}$$

$$[\mathbf{e}_n \times \delta \mathbf{A}]_{S_j} = 0, \quad j = 1, \ldots, J, \tag{6.22}$$

$$[\mathbf{e}_n \times \nabla \times \delta \mathbf{A}]_{S_j} = 0, \quad j = 1, \ldots, J, \tag{6.23}$$

where S_j stands for the surface of the j-th conductor.

Using Eqs. (6.20)–(6.23), it is straightforward to derive the following identities

$$\begin{aligned}
\delta W_V^{(E)} &= \frac{1}{2\mu_0}\int_V |\nabla \times \delta\mathbf{A}|^2\, dV \\
&= \frac{1}{2}\int_{S_p} (\mathbf{e}_n \cdot \xi)\left(\frac{\hat{\mathbf{B}}\cdot\delta\hat{\mathbf{B}}}{\mu_0}\right) dS - \\
&\quad \sum_{j=1}^{J}\frac{1}{2\mu_0}\int_{S_j} (\mathbf{e}_n \times \delta\mathbf{A})\cdot \mathbf{e}_n \times (\mathbf{e}_n \times \nabla \times \delta\mathbf{A})\, dS, \qquad (6.24)
\end{aligned}$$

$$\begin{aligned}
\delta W_V^{(I)} &= \sum_{j=1}^{J}\frac{1}{2\mu_0}\int_{V_j} |\nabla \times \delta\mathbf{A}|^2\, dV \\
&= \sum_{j=1}^{J}\frac{1}{2\mu_0}\int_{S_j} (\mathbf{e}_n \times \delta\mathbf{A})\cdot \mathbf{e}_n \times (\mathbf{e}_n \times \nabla \times \delta\mathbf{A})\, dS + \\
&\quad \sum_{j=1}^{J}\frac{1}{2\mu_0}\int_{V_j} \delta\mathbf{A}\cdot \nabla \times \nabla \times \delta\mathbf{A}\, dV, \qquad (6.25)
\end{aligned}$$

$$\delta W_V^{(D)} = \sum_{j=1}^{J}\frac{\sigma_j\gamma}{2}\int_{V_j} |\delta\mathbf{A}|^2\, dV, \qquad (6.26)$$

$$\delta W_V^{(F)} = -\sum_{j=1}^{J}\frac{\sigma_j}{4\pi R_j}\int_{V_j} \delta\mathbf{A}\cdot\mathbf{G}_j(\delta\mathbf{A})\, dV, \qquad (6.27)$$

where V represents the volume of the vacuum region (not including the conductors) and V_j represents the volume of the j-th conductor.

Combining the above relations and invoking Eq. (6.17) allows us to finally write

$$\delta W_V = \delta W_V^{(E)} + \delta W_V^{(I)} + \delta W_V^{(D)} + \delta W_V^{(F)}, \qquad (6.28)$$

which, by virtue of Eqs. (6.24)–(6.27), is seen to have the desired symmetric form.

6.2.2 Verification of Variational Principle

Formally taking the variation of $\mathcal{L}$ gives

$$\begin{aligned}
\delta\mathcal{L} \;=\; & \int_{V_p} \delta\xi \cdot \mathbf{F}(\xi)\, dV + \\
& \frac{1}{\mu_0}\int_V \delta(\delta\mathbf{A}) \cdot \nabla \times \nabla \times \delta\mathbf{A}\; dV + \\
& \sum_{j=1}^{J} \frac{1}{\mu_0}\int_{V_j} \delta(\delta\mathbf{A}) \cdot \Big[\nabla \times \nabla \times \delta\mathbf{A} + \mu_0\sigma_j \Big(\gamma\delta\mathbf{A} - \\
& \frac{\delta v_j}{2\pi R_j}\,\mathbf{e}_\varphi\Big)\Big]\; dV + \\
& \int_{S_p} (\mathbf{e}_n \cdot \delta\xi)\left(\frac{(\hat{\mathbf{B}} \cdot \delta\hat{\mathbf{B}} - \mathbf{B} \cdot \delta\mathbf{B})}{\mu_0}\right) dS + \\
& \sum_{j=1}^{J} \frac{1}{\mu_0}\int_{S_j} (\mathbf{e}_n \times \delta(\delta\mathbf{A})) \cdot [\mathbf{e}_n \times (\mathbf{e}_n \times \nabla \times \delta\mathbf{A}) - \\
& \mathbf{e}_n \times (\mathbf{e}_n \times \nabla \times \delta\mathbf{A})]\; dS. \qquad (6.29)
\end{aligned}$$

Equation (6.29) shows that setting $\delta\mathcal{L} = 0$ does, in fact, recover the correct set of equations and boundary conditions. In particular, the volume contributions require Eqs. (6.2), (6.16), and (6.17) as the governing equations; the surface contributions give Eqs. (6.20) and (6.23) as natural boundary conditions; and the analysis assumes that Eqs. (6.19), (6.21), and (6.22) are exactly satisfied. Hence, Eq. (6.3) represents a proper variational principle for the problem at hand.

6.2.3 Conservation of Energy

An examination of Eqs. (6.24)–(6.27) reveals that the terms in Eq. (6.28) can be associated with various forms of energy. In particular, $\delta W_V^{(E)}$ represents

the change in inductive energy in the vacuum region surrounding the plasma and the conductors due to the motion of the plasma and the time variation in the perturbed currents. In other words, $\delta W_V^{(E)}$ can be written schematically as

$$\delta W_V^{(E)} = \delta \left(\frac{1}{2} \sum_{j=1}^{J} M_{jp} I_j I_p + \frac{1}{2} \sum_{j=1}^{J} \sum_{k=1}^{J} M_{jk} I_j I_k \right), \tag{6.30}$$

where M_{jp} and M_{jk} are the mutual inductances linking the plasma to the conductors and the conductors to themselves respectively.

The next term, $\delta W_V^{(I)}$ represents the change in internal magnetic energy of the conductors. It can be written

$$\delta W_V^{(I)} = \delta \left(\frac{1}{2} \sum_{j=1}^{J} L_j I_j^2 \right), \tag{6.31}$$

where L_j is the internal inductance of the j-th conductor.

Using a few straightforward manipulations $\delta W_V^{(D)}$ can be written as

$$\delta W_V^{(D)} = \delta \left(\frac{1}{2\gamma} \sum_{j=1}^{J} r_j I_j^2 \right). \tag{6.32}$$

Hence, this term is seen to represent the energy dissipated in the conductors during the instability.

The final term represents the energy input into the system from the feedback voltages. It can be written in the form

$$\delta W_V^{(F)} = \delta \left(\frac{1}{2\gamma} \sum_{j=1}^{J} v_j I_j \right), \tag{6.33}$$

where v_j is the voltage applied to the j-th conductor.

With the above associations in mind, $\mathcal{L}$ is seen to take the form

$$\mathcal{L} = \left(\begin{array}{c} \text{Change in} \\ \text{Fluid Energy} \end{array} \right) + \left(\begin{array}{c} \text{Change in Ext.} \\ \text{Magnetic Energy} \end{array} \right) + \left(\begin{array}{c} \text{Change in Int.} \\ \text{Magnetic Energy} \end{array} \right) + \left(\begin{array}{c} \text{Dissipated} \\ \text{Energy} \end{array} \right) - \left(\begin{array}{c} \text{Source} \\ \text{Energy} \end{array} \right) \quad (6.34)$$

Hence, $\mathcal{L} = 0$ is seen to be a statement of conservation of energy.

6.3 Plasma Model

6.3.1 Displacement Trial Function

In its most general form, the plasma displacement is a function of both $\mathbf{r}$ and t. As such, $\xi(\mathbf{r}, t)$ can, in principle, be solved for using an initial value approach. Here, the plasma is given an initial velocity which causes the plasma to move from its equilibrium position. However, the time evolution of the system could not be followed very far because the expansions used to derive the linearized force operator $\mathbf{F}$ would be violated relatively quickly. In addition, our neglect of plasma inertia is really only valid in an asymptotic theory since kinetic energy accounts for most of the system's total energy near the start of the instability. Therefore, we will limit our attention to exponential stability:

$$\xi(\mathbf{r}, t) = \xi(\mathbf{r})e^{\gamma t}. \quad (6.35)$$

Even with the neglect of the full time dependence of the displacement, the study of completely arbitrary spatial variation for ξ is a difficult task. Luckily, several simplifications can be made on the basis of straightforward physical considerations.

The first simplification results from observations that the most unstable modes tend to be mainly vertical. This has been confirmed by analyses ranging from simple arguments based on current loops to detailed numerical calculations using sophisticated computer methods. We illustrate this point in Fig. 6.2 which shows the exact eigenfunction (as computed by the GATO ideal MHD stability code) for a finite aspect ratio dee-shaped plasma. Hence, on the basis of this consideration, only displacements of the form

$$\xi(\mathbf{r}) = \xi(\mathbf{r})\mathbf{e}_Z \tag{6.36}$$

will be analyzed in this thesis.

A second simplification is due to the fact that the most damaging modes also tend to be incompressible (i.e. $\nabla \cdot \xi = 0$). This can be proven rigorously for $n \neq 0$ modes but is not necessarily true for $n = 0$ modes. Nevertheless, a number of GATO runs have suggested that compressibility normally plays a negligible role in axisymmetric stability. There are, however, at least two cases where compressibility can be important. First, if horizontal displacements are considered, plasma compressibility does in fact play a major role. Second, even in the case of vertical displacements, there are extreme cases where plasma compressibility is important. For instance, Hoffmann, Turnbull,and Marcus [89] demonstrated that the existence of a close fitting wall near the top and the bottom of the plasma could lead to complicated "convective cell" instabilities with a highly compressible nature. For the purposes of this thesis, only vertical incompressible displacements will be considered. With this assumption, the most general form of ξ is given by

$$\xi(\mathbf{r}) = \xi(R)\mathbf{e}_Z. \tag{6.37}$$

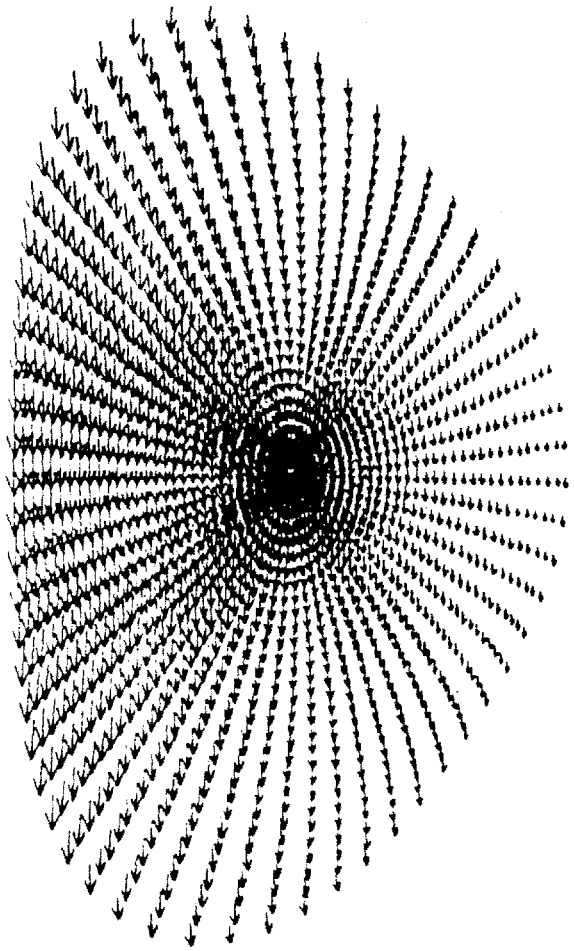

Figure 6.2: *Exact GATO eigenfunction for finite aspect ratio dee-shaped plasma. The arrows give the local direction and magnitude of ξ.*

In many calculations, including those presented in the previous chapter, it has been further assumed that $\xi(R) = const.$ This rigid vertical shift assumption has the very desirable feature that it leads to great simplifications in the analysis. In addition, it has been rigorously demonstrated that the exact eigenfunction for the straight elliptical tokamak with a flat current profile is, in fact, the rigid vertical shift [17]. However, for more realistic cross-sections, such as the finite aspect ratio dee, it turns out the displacement is far from uniform. This point is illustrated by Fig. 6.2 which shows that $\xi(R)$ is largest on the inboard side of the plasma. Based upon this observation we will focus on displacements of the form

$$\xi(R) = \xi_Z \left(\frac{R_m}{R}\right)^{\nu}, \tag{6.38}$$

where ξ_Z is a constant, R_m is the radial location of the magnetic axis, and ν is a parameter controlling the non-uniformity in the displacement. Equation (6.38) has several desirable features. First, it closely models the radial variation shown in Fig. 6.2. Second, it includes the rigid shift as a special case obtainable by setting $\nu = 0$. Finally, it is simple enough to allow efficient numerical calculations. A major goal of this chapter will be to assess the effect of non-uniform displacements on tokamak vertical stability in the presence of a resistive wall and feedback. Rebhan and Salat [90] investigated similar displacements in the context of the study of ideal stability using the sharp boundary model [59].

6.3.2 Evaluation of Fluid Energy

By comparing Eq. (6.8) with Eq. (6.38), we can immediately write

$$\delta W_F = \xi_Z W_F \xi_Z, \tag{6.39}$$

where $W_F = V + S$ and

$$V = \frac{1}{2\mu_0}\int_{V_P}\left[\frac{\nu}{R_m}\left(\frac{R_m}{R}\right)^{\nu+1} B_R\right]^2 dV, \tag{6.40}$$

$$S = -\frac{\pi}{2\mu_0}\int_0^{2\pi}\frac{RR_\mu Z_{\mu\mu} - Z_\mu(RR_{\mu\mu}+R_\mu^2)}{Q^2}\left(\frac{R_m}{R}\right)^{2\nu} B_p^2\, d\mu - \frac{\pi}{\mu_0}\int_0^{\pi}\left(\frac{R_m}{R}\right)^{2\nu}\frac{\partial}{\partial\mu}(RB_RB_Z)\, d\mu. \tag{6.41}$$

6.3.3 Evaluation of Vacuum Energy

Despite the appealing physical interpretation of Eq. (6.28), it is actually more convenient from the point of view of computation to use Eq. (6.6) to evaluate δW_V. Using Eq. (6.38), this can be written

$$\delta W_V = \frac{\pi\xi_Z}{\mu_0}\int_0^{2\pi}\delta\psi_p(Q\delta\hat{B}_p)\, d\mu, \tag{6.42}$$

where

$$\delta\psi_p = -\frac{RR_\mu B_p}{Q}\left(\frac{R_m}{R}\right)^{\nu}, \tag{6.43}$$

and $\delta\hat{B}_p = \mathbf{e}_t\cdot\delta\hat{\mathbf{B}}$ is the tangential component of the perturbed vacuum field.

Notice that the φ-component of perturbed vacuum field does not appear in Eq. (6.42). This is because $\delta\hat{B}_\varphi|_{S_p} = 0$ identically for vertical incompressible displacements. To see this, we can use Eq. (6.11) to explicitly calculate δB_φ

$$\delta B_\varphi = -\xi(R)\left[\frac{\partial B_\varphi}{\partial Z}\right] = -\xi(R)\left[\frac{1}{R}\frac{dF}{d\psi}\frac{\partial\psi}{\partial Z}\right]. \tag{6.44}$$

In Eq. (6.44), F is the current free function introduced in Chapter 3. Recall further from that chapter that, in order to ensure that the toroidal current density vanishes at the plasma boundary, $dF/d\psi \mid_{S_p} = 0$. Hence, $\delta B_\varphi \mid_{S_p} = 0$ which, in turn, implies that $\delta \hat{B}_\varphi \mid_{S_p} = 0$ to ensure pressure balance. It should be emphasized that this would not be the case for radial displacements. Here, $\delta \hat{B}_\varphi$ would be expected to make a major contribution to δW_V.

In order to evaluate δW_V it is necessary to compute $\delta \hat{B}_p$ as a function of μ on the plasma surface. In principle, this can be accomplished by solving Eqs. (6.16) and (6.17) subject to the boundary conditions given in Eqs. (6.20)–(6.23). However, this is a very difficult task given conductors of finite extent. Therefore, we will assume $a_c \rightarrow 0$. In this limit, we can write to high accuracy

$$\delta \hat{\mathbf{B}} = \nabla \delta\phi + \sum_{j=1}^{J} \mu_0 \, \delta I_j \frac{\nabla \Psi_j \times \mathbf{e}_\varphi}{R}, \tag{6.45}$$

where $\delta\phi$ is a scalar magnetic potential satisfying Laplace's equation and Ψ_j is the flux due a thin conductor given by Eq. (4.19).

The perturbed field $\delta \hat{\mathbf{B}}$ must satisfy Eq. (6.20) on the plasma surface and must also vanish at infinity. Using Eq. (6.45), the relation at the plasma surface can be written as follows

$$R \frac{\partial \delta\phi}{\partial n} = \frac{\partial}{\partial \mu} \left(\xi_Z \delta\psi_p + \sum_{j=1}^{J} \mu_0 \, \delta I_j \Psi_j \right). \tag{6.46}$$

Because we are restricting attention to axisymmetric modes, we are able to use the fast and efficient Green's function techniques described in Chapter 4 to compute $\delta\phi$. As in that chapter we expand the scalar magnetic potential and its normal derivative in Fourier series

$$\delta\phi = \sum_{m=-M}^{M} a_m \, e^{im\mu}, \tag{6.47}$$

$$R\frac{\partial \delta\phi}{\partial n} = \sum_{m=-M}^{M} \left(\xi_Z \, c_m + \sum_{j=1}^{J} D_{mj} \delta I_j \right) e^{im\mu}, \tag{6.48}$$

where $\mathbf{c}$ is a column vector of length $(2M+1)$ whose (known) elements are given by

$$c_m = \frac{im}{2\pi} \int_0^{2\pi} \delta\psi_p e^{-im\mu} d\mu, \tag{6.49}$$

and $\mathbf{D}$ is a $(2M+1) \times J$ matrix whose elements are written

$$D_{mj} = \frac{im}{2\pi} \int_0^{2\pi} \mu_0 \Psi_j e^{-im\mu} d\mu. \tag{6.50}$$

We further recall from Chapter 4 that the application of the scalar version of Green's theorem [Eq. (4.30)] yields a simple matrix equation which can be inverted for the Fourier coefficients of the scalar magnetic potentials

$$\mathbf{a} = \xi_Z \mathbf{d} + \mathbf{E} \cdot \delta\mathbf{i}, \tag{6.51}$$

where

$$\mathbf{d} = [\mathbf{I} + \mathbf{A}]^{-1} \cdot \mathbf{C} \cdot \mathbf{c}, \tag{6.52}$$

$$\mathbf{E} = [\mathbf{I} + \mathbf{A}]^{-1} \cdot \mathbf{C} \cdot \mathbf{D}, \tag{6.53}$$

and $\mathbf{A}$ and $\mathbf{C}$ were originally defined in Eqs. (4.51) and (4.52).

On the basis of Eqs. (6.52) and (6.53), we therefore see that we may write $\delta\hat{B}_p$ in the form

$$\delta\hat{B}_p(\mu) = \xi_Z b^{(\xi)}(\mu) + \mathbf{b}^{(I)}(\mu) \cdot \delta\mathbf{i}, \tag{6.54}$$

where $b^{(\xi)}(\mu)$ represents the contribution to the perturbed field from the movement of the plasma and $\mathbf{b}^{(I)}(\mu)$ represents the contribution from the currents induced in the conductors. The functions are explicitly written

$$b^{(\xi)}(\mu) = \frac{1}{Q} \sum_{m=-M}^{M} im d_m e^{im\mu}, \tag{6.55}$$

$$b_j^{(I)}(\mu) = \hat{b}_j^{(I)}(\mu) + \frac{\mu_0}{Q} \frac{1}{R} \frac{\partial \Psi_j}{\partial n}, \tag{6.56}$$

where

$$\hat{b}_j^{(I)}(\mu) = \frac{1}{Q} \sum_{m=-M}^{M} im E_{mj} e^{im\mu}. \tag{6.57}$$

We can finally substitute Eqs. (6.55) and (6.56) into Eq. (6.42) to obtain

$$\delta W_V = \xi_Z \, W_V^{(\xi)} \, \xi_Z + \xi_Z \, \mathbf{W}_V^{(I)} \cdot \delta \mathbf{i}, \tag{6.58}$$

where

$$W_V^{(\xi)} = \frac{\pi}{\mu_0} \int_0^{2\pi} \delta\psi_p(Q b^{(\xi)}) \, d\mu, \tag{6.59}$$

$$W_{Vj}^{(I)} = \frac{\pi}{\mu_0} \int_0^{2\pi} \delta\psi_p(Q b_j^{(I)}) \, d\mu. \tag{6.60}$$

6.3.4 Plasma Equation of Motion

Combining Eqs. (6.39) and (6.58) gives the Lagrangian in the form

$$\mathcal{L} = \xi_Z \, (W_F + W_V^{(\xi)}) \, \xi_Z + \xi_Z \, \mathbf{W}_V^{(I)} \cdot \delta \mathbf{i} = 0. \tag{6.61}$$

Equation (6.61) describes the energetics of the plasma motion. However, stability cannot yet be assessed since the perturbed currents are unknown. This problem will be addressed in the next section.

6.4 Plasma-Conductor Coupling

The derivation of Eq. (6.61) yielded no constraints with regard to choosing the perturbed conductor currents. However, on physical grounds, one would expect that the conductor currents cannot be chosen arbitrarily since they must be strongly coupled to the displacement of the plasma through inductive effects. In fact, this coupling was ignored when Eq. (6.45) was written since no mention was made of the governing equation inside the conductors [Eq. (6.17)] or the boundary conditions at the surfaces of the conductors [Eqs. (6.22) and (6.23)]. When these relations are considered, a series of equations relating the perturbed conductor currents to the plasma displacement are obtained. The derivation of these equations is the subject of this section.

6.4.1 Derivation of Circuit Equations

In order to derive the plasma-conductor coupling equations, it is convenient to consider the time-dependent form of Eq. (6.17)

$$\nabla \times \nabla \times \mathbf{A} = -\mu_0 \sigma \left(\frac{\partial \mathbf{A}}{\partial t} - \frac{v}{2\pi R} \mathbf{e}_\varphi \right). \tag{6.62}$$

Rather than self-consistently solving Eq. (6.62), we will make the simplifying assumption that the current density in the j-th conductor can be written

$$\mathbf{J}_j = J_j \mathbf{e}_\varphi, \tag{6.63}$$

where $J_j = const.$ Due to the fact that the conductors are thin and the problem is entirely axisymmetric, it is expected that this represents a very accurate approximation. Scalar multiplying Eq. (6.62) by $\mathbf{J}_j$, integrating

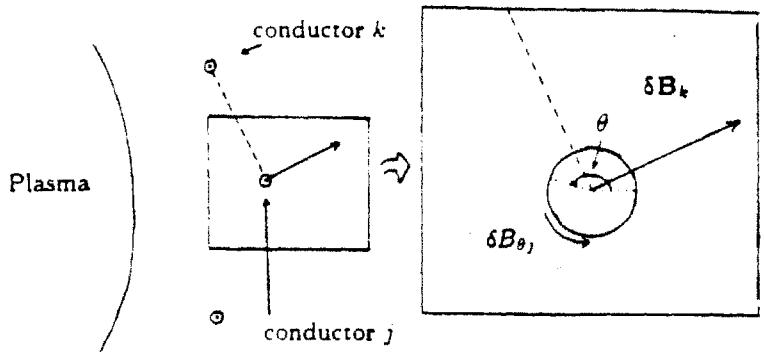

Figure 6.3: *Conductor coordinate system and fields.*

over the volume of the conductor, and performing a series of straightforward algebraic manipulations gives

$$\int_{V_j} \frac{v_j}{2\pi R_j} J_j \, dV = \frac{1}{\sigma_j} \int_{V_j} J_j^2 \, dV + \frac{1}{\mu_0} \int_{V_j} B_\theta \frac{\partial B_\theta}{\partial t} \, dV + \frac{1}{\mu_0} \int_{S_j} B_\theta \frac{\partial A_\varphi}{\partial t} \, dS, \tag{6.64}$$

where θ is the polar angle coordinate defined in Fig. 6.3.

We can now linearize Eq. (6.64) by writing all quantities as

$$Q(\mathbf{r}, t) = Q(\mathbf{r}) + \delta Q(\mathbf{r}) \, e^{\gamma t}. \tag{6.65}$$

A simple calculation yields

$$\delta v_j I_j = r_j \delta I_j I_j + \frac{\gamma}{\mu_0} \int_{V_j} B_\theta \, \delta B_\theta \, dV + \frac{\gamma}{\mu_0} \int_{S_j} B_\theta \, \delta A_\varphi \, dS. \tag{6.66}$$

Note that the fields making up the integrands in Eq. (6.66) result from contributions from the plasma along with all of the conductors. However, in the limit $a_c \rightarrow 0$, many of these contributions vanish upon integration. This leaves

$$\delta v_j I_j = r_j \delta I_j I_j + \frac{\gamma}{\mu_0} \int_{V_j} B_{\theta j}\, \delta B_{\theta j}\, dV + \frac{\gamma}{\mu_0} \int_{S_j} B_{\theta j} \delta A_\varphi\, dS. \tag{6.67}$$

As Eq. (6.67) shows, the only B-field contribution comes from the j-th conductor. This is explained by considering Fig. 6.3. In that figure, the B-field produced by the plasma and other conductors is seen to approximately have a constant magnitude and direction over the entire cross-section of conductor j. Hence, the θ-component of those fields oscillates along surfaces of constant radius in such a way to cause all of integrals involving them to vanish. This is not the case for the field produced by j-th conductor. That field almost entirely points in the θ-direction with a magnitude well approximated by the relation for a straight wire

$$B_{\theta j} = \frac{\mu_0 I_j r}{2\pi a_c^2}. \tag{6.68}$$

Since the magnitude of $B_{\theta j}$ does not oscillate, finite contributions to the integrals are made.

In the case of the vector potential present in the last term in Eq. (6.67), the contributions from the plasma and the other conductors do not vanish. This is because the δA_φ from those sources is approximately constant on S_j in the limit $a_c \rightarrow 0$. Furthermore, this constant magnitude is not expected to be ignorable in comparison to $\delta A_{\varphi j}$ since the vector potential varies logarithmically with distance.

Substituting Eq. (6.68) into Eq. (6.67) and canceling out the equilibrium currents gives finally

$$\delta v_j = r_j \delta I_j + \gamma \left(\frac{\mu_0 R_j}{4} \delta I_j + 2\pi \, \delta\psi \mid_{S_j} \right), \tag{6.69}$$

where we have again introduced the flux function $\delta\psi = R\,\delta A_\varphi$. Versions of Eq. (6.69) clearly can be written for all of the external conductors. These J equations along with Eq. (6.61) completely describe the dynamics of the system. However, to make practical use of Eq. (6.69), it is first necessary to provide a specification for the feedback voltage δv_j and to derive an expression for the perturbed flux at the surfaces of the conductors $\delta\psi \mid_{S_j}$.

6.4.2 Feedback Control Laws

So far we have treated the form of the feedback voltage in purely mathematical terms. Recall from Eq. (6.18) that the voltage was written in terms of an operator $\mathbf{G}$ required to possess the self-adjoint property depicted in Eq. (6.19). In a practical sense, this requirement places virtually no limitation on the usable types of feedback laws. To see this, consider the following fairly realistic form for δv_j

$$\delta v_j = \sum_{n=1}^{N} G_n \frac{1 + t_{Cn}\gamma}{1 + t_{Dn}\gamma} \, \delta A_\varphi(\mathbf{r}_n). \tag{6.70}$$

In Eq. (6.70), the points $\mathbf{r}_n$ are simply a series of places at which to sample the vector potential. In a real experiment or reactor, these points would correspond to the locations of flux measuring loops. As long as the sampling points are not inside any of the conductors, it is easy to show that Eq. (6.19) is satisfied.

Equation (6.70) illustrates three important features of feedback control laws: gain, delay, and compensation. These are represented in Eq. (6.70) by the parameters G_n, t_{Dn}, and t_{Cn} respectively. The gain is simply the degree to which a measurement of plasma motion is amplified and fed back to reduce the growth rate. Delays are time lags that effectively result in a plasma

movement at time t not being responded to until a later time $t = t + t_D$. Compensation represents an attempt to anticipate the motion of the system by feeding back on the rate at which the measurements change in order to offset some of the performance loss brought on by delays.

Delays reduce the speed at which a control system for a tokamak can respond to an axisymmetric instability These delays can result from a number of factors. First, realistic measurement devices require a finite amount of time to sense a movement of the plasma, process the measurement, and send a demand to a power supply to respond. Furthermore, realistic power supplies generally require some time to respond to a demand for power. In realistic experimental configurations, power supply delays are on the order of 0.1 msec while measurement delays are much smaller [91].

In addition to the external delays just described, there are also a series of inherent delays present in the system. For instance, the current in a conductor cannot change instantaneously. Instead, this occurs on the L/R timescale. Also, since feedback coils are usually located outside of the vacuum chamber, the fields produced by those coils diffuse through the wall on resistive diffusion τ_D timescale. These effects are actually included in the circuit equations given by Eq. (6.69) so they need not be modeled by adding terms to the feedback control law.

To design a robust axisymmetric stability system, careful attention must be paid to the accurate estimation of delays and the optimization of feedback laws and sensor locations to provide compensation. Luckily, very powerful mathematical techniques exist for dealing with these issues and other authors have, in fact, applied these techniques to tokamaks [92].

Since this thesis is not concerned with the detailed design of vertical stability systems, we will assume a fairly un-realistic, but simple, feedback control law of the form

$$\delta v_j = G_j(1 + t_{Cj}\gamma)\xi_Z. \tag{6.71}$$

This corresponds to ignoring all external delays and choosing $G_n(\mathbf{r})$ to sample the vector potential at the plasma surface (where $\delta A_\varphi \propto \xi$).

As a final point, it should be emphasized the analysis does not require a control law of the form given in Eq. (6.71) or even in Eq. (6.70). Different laws based on measurements of magnetic field or induced conductor currents with different dependences on γ can, in fact, be easily constructed so as to be consistent with Eq. (6.19).

6.4.3 Calculation of Perturbed Flux

As was the case for the perturbed scalar potential, it will be convenient to consider the perturbed flux to be made up of two contributions: one due to the motion of the plasma and one due to the induced conductor currents.

$$\delta\psi = \delta\hat{\psi}^{(\xi)} + \delta\psi^{(I)}. \tag{6.72}$$

Consistency with the governing equation in the vacuum region [Eq. (6.16)] and the boundary condition at the plasma surface [Eq. (6.20)] demands that

$$\Delta^* \delta\hat{\psi}^{(\xi)} = 0, \tag{6.73}$$

$$\delta\hat{\psi}^{(\xi)} \mid_{S_p} = -\xi_Z \, \delta\psi_p, \tag{6.74}$$

and

$$\Delta^* \delta\hat{\psi}^{(I)} = 0, \tag{6.75}$$

$$\delta\hat{\psi}^{(I)} \mid_{S_p} = -\sum_{k=1}^{J} \mu_0 \, \Psi_k \, \delta I_k \mid_{S_p}, \tag{6.76}$$

where $\delta\hat{\psi}^{(I)}$ is defined via

$$\delta\psi^{(I)} = \delta\hat{\psi}^{(I)} + \sum_{k=1}^{J} \mu_0 \, \Psi_k \, \delta I_k. \tag{6.77}$$

Vector Green's Theorem

Since $\delta\hat{\psi}^{(\xi)}$ and $\delta\hat{\psi}^{(I)}$ are only required on the plasma surface, we are again led to consider Green's theorem techniques as the method of solution. However, since we are computing fluxes rather than scalar magnetic potentials, we must employ the vector version of Green's theorem [22] which is written in greatest generality as

$$\begin{aligned}\sigma\delta\hat{\mathbf{A}}(\mathbf{r}) \;+\; \int_{S_p} \Big[&(\mathbf{e}'_n \cdot \delta\hat{\mathbf{A}}(\mathbf{r}'))\nabla'\hat{G}(\mathbf{r},\mathbf{r}') + \\ &(\mathbf{e}'_n \times \delta\hat{\mathbf{A}}(\mathbf{r}')) \times \nabla'\hat{G}(\mathbf{r},\mathbf{r}') + \\ &\hat{G}(\mathbf{r},\mathbf{r}')(\mathbf{e}'_n \times \nabla' \times \delta\hat{\mathbf{A}}(\mathbf{r}'))\Big]\; dS' = 0, \end{aligned} \tag{6.78}$$

where the various quantities are the same as those originally defined in Chapter 4 for the scalar version of Green's theorem. In particular, $\hat{G}$ is the infinite space Green's function [Eq. (4.27)], $\mathbf{r}$ denotes the observation point, $\mathbf{r}'$ denotes the integration variables, and σ is the weight function depending on the location of the observation point with respect to the plasma surface [Eq. (4.29)].

Equation (6.78) can be greatly simplified by making use of the assumption of toroidal axisymmetry and the fact that only the φ-component of the $\delta\hat{\mathbf{A}}$ is non-zero. A straightforward calculation gives

$$\begin{aligned}\sigma\delta\hat{\psi}(\mathbf{r}) \;+\; \int_{S_p} \frac{1}{(R')^2}\Big[&\delta\hat{\psi}(\mathbf{r}')(\mathbf{e}'_n \cdot \nabla'\hat{H}(\mathbf{r},\mathbf{r}')) - \\ &\hat{H}(\mathbf{r},\mathbf{r}')(\mathbf{e}'_n \cdot \nabla'\delta\hat{\psi}(\mathbf{r}'))\Big]\; dS' = 0, \end{aligned} \tag{6.79}$$

where

$$\hat{H}(\mathbf{r},\mathbf{r}') = \frac{R'R\cos(\varphi'-\varphi)}{4\pi}\frac{1}{|\mathbf{r}'-\mathbf{r}|}. \tag{6.80}$$

with $|\mathbf{r}' - \mathbf{r}|$ as given by Eq. (4.28).

As was the case for the scalar version of Green's theorem, it is possible to perform the φ'-integration in Eq. (6.79) analytically. This yields

$$\delta\hat{\psi} \mid_{S_j} + \int_0^{2\pi} \left(\frac{\delta\hat{\psi}'}{R'} \frac{\partial H_j}{\partial n'} - \frac{H_j}{R} \frac{\partial \delta\hat{\psi}'}{\partial n'} \right) d\mu' = 0, \tag{6.81}$$

where

$$H_j = -\frac{1}{4\pi} \int_0^{2\pi} \frac{R' R_j \cos(\varphi' - \varphi)}{|\mathbf{r}' - \mathbf{r}_j|} \, d\varphi. \tag{6.82}$$

Note that in Eqs. (6.81) and (6.82), the observation point has been chosen to be at the location of the *j-th* conductor (R_j, Z_j). Hence, σ has been taken to be unity. The integration points remain on the plasma surface.

Evaluating the integral in Eq. (6.82) gives the very simple result

$$H_j = -\Psi_j. \tag{6.83}$$

Therefore, using Eqs. (4.19) and (4.20) we find

$$\frac{1}{R'} \frac{\partial H_j}{\partial n'} = \frac{1}{2\pi} \left(\frac{R_j}{R'} \right)^{1/2} \left\{ \Gamma_j \left[\frac{(2 - k'^2_j)E - 2(1 - k'^2_j)K}{k'_j} \right] + \Lambda_j k'_j (E - K) \right\}, \tag{6.84}$$

with

$$k'^2_j = \frac{4R'R_j}{(R' + R_j)^2 + (Z' - Z_j)^2}, \tag{6.85}$$

$$\Lambda_j = \frac{Z'_\mu (R' - R_j) - R'_\mu (Z' - Z_j)}{(R' - R_j)^2 + (Z' - Z_j)^2}, \tag{6.86}$$

$$\Gamma_j = \frac{Z'_\mu}{2R'}. \tag{6.87}$$

Evaluation of Perturbed Flux due to Plasma Displacement

We can now use Eq. (6.81) along with Eqs. (6.55) and (6.74) to evaluate $\delta\hat{\psi}^{(\xi)}$. We obtain

$$\delta\hat{\psi}^{(\xi)}\,|_{S_j} = \xi_Z L_j^{(\xi)}, \tag{6.88}$$

where

$$L_j^{(\xi)} = \frac{1}{2\pi}\int_0^{2\pi}\left[\delta\psi_p'\left(\frac{1}{R'}\frac{\partial H_j}{\partial n'}\right) + H_j\,Q'\,b^{(\xi)}(\mu')\right]d\mu'. \tag{6.89}$$

Evaluation of Perturbed Flux due to Conductor Currents

Similarly, we can use Eq. (6.57) to write

$$\frac{\mu_0 R_j}{4}\delta I_j + 2\pi\delta\psi^{(I)}\,|_{S_j} = \sum_{k=1}^{J} L_{jk}^{(I)}\,\delta I_k, \tag{6.90}$$

where

$$L_{jk}^{(I)} = \frac{1}{2\pi}\int_0^{2\pi}\left[\mu_0\,\Psi_k'\left(\frac{1}{R'}\frac{\partial H_j}{\partial n'}\right) + H_j\,Q'\,\hat{b}_k^{(I)}(\mu')\right]d\mu', \tag{6.91}$$

when $j \neq k$ and

$$L_{jk}^{(I)} = \frac{\mu_0 R_j}{4} + \ell_j, \tag{6.92}$$

when $j = k$.

6.4.4 Plasma-Conductor Coupling Equations

Having defined all quantities, we can now write the equations that govern the coupling between the plasma and the conductors in the following form

$$G_j(1 + t_{Cj}\gamma)\,\xi_Z = r_j\delta I_j + \gamma\left[\xi_Z\,L_j^{(\xi)} + \sum_{k=1}^{J} L_{jk}^{(I)}\,\delta I_k\right]. \tag{6.93}$$

6.5 Solution for the Growth Rate and the Perturbed Currents

Using Eq. (6.61), it is possible to write ξ_Z in terms of δI_j

$$\xi_Z = -\frac{1}{W_F + W_V^{(\xi)}} \sum_{k=1}^{J} W_{Vk}^{(I)} \delta I_k. \tag{6.94}$$

This can, in turn, be substituted into Eq. (6.93) to yield a generalized matrix eigenvalue equation

$$\mathbf{R} \cdot \delta\mathbf{i} = \gamma \mathbf{M} \cdot \delta\mathbf{i}, \tag{6.95}$$

where γ is the eigenvalue and $\delta\mathbf{i}$ is the eigenvector. The elements of the matrices $\mathbf{R}$ and $\mathbf{M}$ are given by

$$R_{jk} = \frac{G_j W_{Vk}^{(I)}}{W_F + W_V^{(\xi)}} - \tau_j \delta_{jk}, \tag{6.96}$$

$$M_{jk} = \frac{(G_j t_{Cj} - L_j^{(\xi)}) W_{Vk}^{(I)}}{W_F + W_V^{(\xi)}} + L_{jk}^{(I)}. \tag{6.97}$$

In Eq. (6.96), δ_{jk} is the Kronecker delta function.

6.6 Solution Procedure Summary

The analysis needed to derive the various equations in this chapter is relatively complicated. However, the procedure for analyzing tokamak vertical stability is actually quite simple. Specifically, we assume that the following is known:

- Equilibrium information:

1. Plasma shape,
2. B_R and B_Z throughout plasma.

- Conductor information:
  1. Location and composition of resistive wall,
  2. Locations and compositions of resistive PF/OH coils and passive stabilizers,
  3. Possibly, feedback control laws for some of the coils.
- The displacement non-uniformity parameter ν.

These are the only inputs required by the solution procedure. The output of the procedure consists of the growth rate γ and the corresponding perturbed conductor currents δI_j. These quantities are calculated as follows. First, Eqs. (6.40) and (6.41) are used to evaluate W_F. Second, the methods of Appendix B are used to finite-difference the wall, the coils, and any passive stabilizers into J thin circular conductors. Third, the scalar version of Green's theorem is used to evaluate the tangential component of the perturbed vacuum field at the plasma surface. This is then substituted into Eqs. (6.59) and (6.60) to yield $W_V^{(\xi)}$ and W_V^I. Fourth, the vector version of Green's theorem is employed to evaluate $L_j^{(\xi)}$ and $L_{jk}^{(I)}$ using Eqs. (6.89) and (6.91). Fifth, all of these quantities can be substituted into Eqs. (6.96) and (6.97) to give the elements of the matrices $\mathbf{R}$ and $\mathbf{M}$ which make up the generalized matrix eigenvalue problem depicted in Eq. (6.95). Finally, this problem can be solved using standard numerical techniques for γ (the eigenvalue) and δI_j (the eigenvector).

6.7 Computer Implementation

The ideas of the previous sections have been implemented in a computer program called "vPFC." This code can analyze the vertical stability properties of a typical tokamak configuration ($J \approx 32$–64) in 3.0–6.0 sec of Cray CPU time. In this section, we will discuss a number of issues which illustrate various numerical properties of the vPFC code and also provide evidence as to the code's correctness.

6.7.1 Verification of Finite Difference Convergence

One of the major assumptions in the analysis is that the finite differencing scheme presented in Appendix B yields an acceptable representation for a continuous vacuum chamber wall. In particular, it is necessary to verify that the growth rate converges to a known value as the number of conductors making up the wall increases. This concern is addressed as follows. We consider a straight elliptical tokamak with zero beta and a flat current density profile surrounded by a thin resistive wall parameterized by Eqs. (5.91) and (5.92). We also assume a uniform shift displacement so $\nu = 0$. This case was analyzed in the previous chapter using the variational formula given in Eq. (5.73). The resulting growth rate is plotted in Fig. 6.4 along with the variation in the growth rate computed by vPFC with the number of conductors used to represent the wall. The graph shows that as the number of conductors increases the vPFC result does indeed quickly converge to the analytic result.

More complicated plasma and wall shapes have been investigated. For most configurations, it has been found that no more than 30–50 conductors representing the wall are required to achieve high accuracy in the growth rate. There is, however, one practical situation where this may not be true. Specifically, when flux loops and magnetic probes are placed along the inner

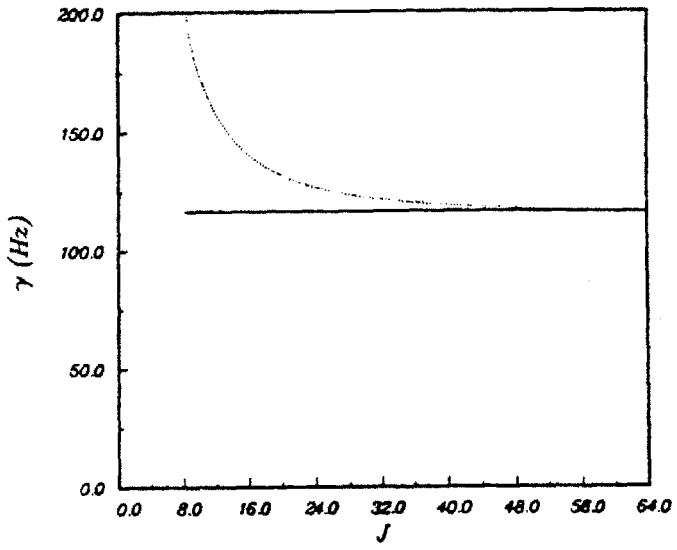

Figure 6.4: *Plot of γ vs. J to illustrate finite difference convergence. Plasma parameters:* $\kappa_a = 2$, $\alpha_f = -25.0$, $b_p = 0.001$. *Wall parameters:* $t = 0.45$, $d = 0.025$ m ***stainless steel.***

surface of the vacuum chamber, it is possible for the discreteness of the finite differenced wall to introduce large errors into field measurements. Therefore, special care must be taken to ensure that the number of conductors is sufficiently high to reduce these measurement errors to acceptable levels.

6.7.2 Comparison with Known Results

Figure 6.4 demonstrated that vPFC is capable of recovering a single known result assuming a sufficiently large number of conductors are used to represent the vacuum chamber wall. It is necessary to further show that this good agreement is achievable for a variety of plasma shapes and current profiles. To this end, we will reconsider the two configurations analyzed in the previous chapter for the case of the uniform shift: (a) the straight ellipse with a peaked current density profile and (b) the straight dee with a flat current density profile. Recall from Figs. 5.6 and 5.7 that it was found that

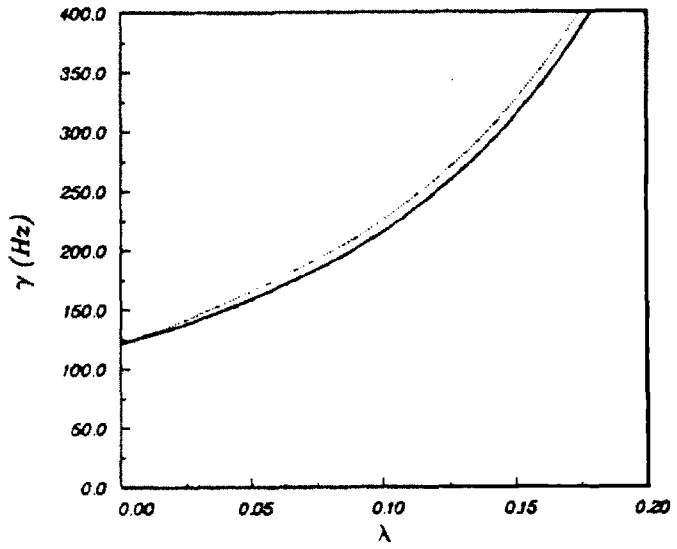

Figure 6.5: *Plot of γ vs. λ showing comparison between vPFC results (dotted line) and analytic results (solid line) for a straight elliptical tokamak with k_a =* 2.0. *A* 0.025 m *stainless steel wall is located at* $t = 0.45$.

peaking of the current density was destabilizing and that triangularity was stabilizing. These results are reproduced in Figs. 6.5 and 6.6 along with vPFC results obtained using exactly the same equilibrium information and wall configuration (modeled using 32 conductors). Note the extremely good agreement over the entire range of λ and δ_a respectively.

6.7.3 Normal Modes for the Passive Case

So far, we have shown that "the" growth rate computed by vPFC agrees well with results obtained previously in this thesis. This represents a desirable observation regarding the overall correctness of the code and the formulation. However, the reference to a single growth rate needs to be explained in more detail. This is because the solution to Eq. (6.95) actually consists of J growth frequencies and J corresponding perturbed current distributions representing the normal modes of the system.

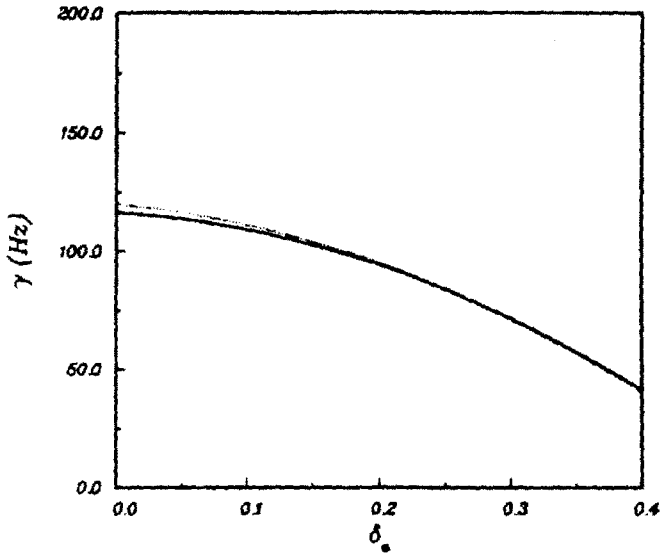

Figure 6.6: *Plot of γ vs. δ_a showing comparison between vPFC results (dotted line) and analytic results (solid line) for a straight dee-shaped tokamak with $k_a = 2.0$. A 0.025 m stainless steel wall is located at $t = 0.45$.*

For purposes of illustration, we will consider the straight elliptical tokamak configuration shown in Fig. 6.7. The plasma has an elongation $\kappa_a = 2$, a flat current profile, and zero beta. A stainless steel wall is located at $t = 0.45$. This wall is finite differenced into 32 conductors, labeled in the figure with an index k that increases in a counter-clockwise direction around the surface of the wall. The figure also shows two PF coils but, for now, we will assume that they are not functioning (even with regard to passive stabilization). Again, we take $\nu = 0$.

The arrangement of γ's found by solving Eq. (6.95) is shown in Fig. 6.8. Notice that all of the frequencies are purely real. This is because the matrices $\mathbf{R}$ and $\mathbf{M}$ are exactly symmetric in the absence of feedback. This symmetry, in turn, is a manifestation of the symmetric nature of the Lagrangian demonstrated earlier in this chapter.

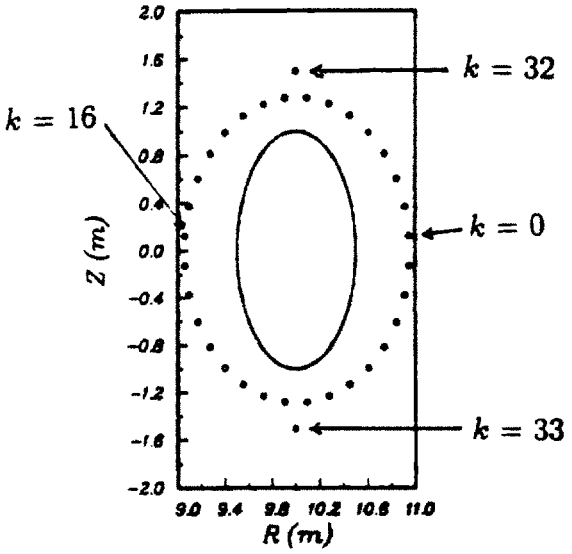

Figure 6.7: *Illustrative tokamak configuration for purposes of discussing normal mode behavior.*

Another feature of the frequency distribution in Fig. 6.8 is the fact that all of the γ's but one are negative, indicating damped solutions. The single positive γ is the growth rate that was used in the previous comparisons.

Also of interest are the perturbed currents induced in the wall. Recall that these are the eigenvectors of Eq. (6.95). Three of the J perturbed current distributions are shown in Fig. 6.9 as a function of the angular index k. Note that the maximum magnitude in each case is normalized to unity. This is necessary because eigenvectors are indeterminate within a constant multiplier.

The $\delta \mathbf{i}$ corresponding to the single growing γ is shown in Fig. 6.9a. Note that the angular distribution takes the form of a sine wave. This is an an expected result on the basis of the analysis in Chapter 5. Specifically, Eq. (5.32) implies that the perturbed current density in the thin wall will be proportional to the perturbed vector potential at the wall. Furthermore,

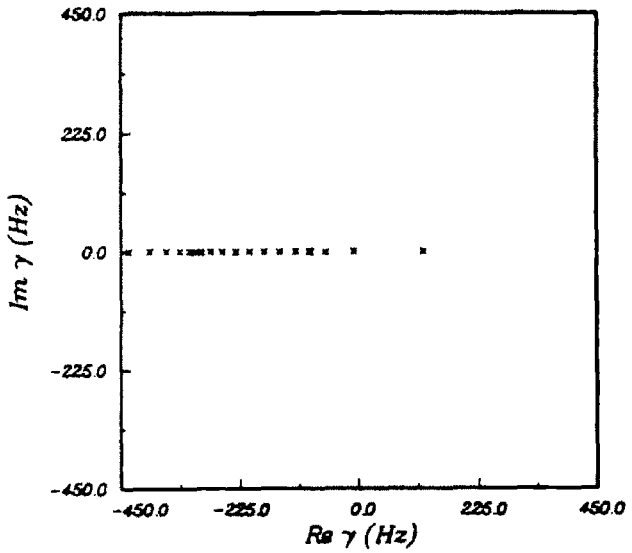

Figure 6.8: *Eigenvalue (γ) distribution for straight elliptical tokamak case.*

Eq. (5.110) shows that the perturbed vector potential at the wall is written as a fourier sine series with $m = 1$ as the dominant contribution.

If each of the J sets of perturbed currents is substituted into Eq. (6.94), it is found that the largest relative value of ξ_Z is associated with the single growing mode whose perturbed current distribution is shown in Fig. 6.9a. The perturbed current distribution corresponding to the (damped) mode giving the next largest relative displacement is shown in Fig. 6.9b. This distribution is seen to be approximately proportional to $\sin 3\mu$. Again, reference to Eq. (5.110) shows that this is the expected result. Similarly, the $m = 5$ and $m = 7$ poloidal mode numbers yield the two next largest values of ξ_Z. In general, the $m = 1$ mode always dominates; however, the relative sizes of the $m > 1$ modes increase as the current distribution becomes more peaked.

Figure 6.9c shows the δi that corresponds to the smallest relative value of the displacement ($\xi_Z < 10^{-11}$). Notice that the parity of this perturbed current distribution is even. This is in contrast to the distributions in Fig. 6.9a

and 6.9b which have odd parity. On the basis of the even parity of the perturbed current distribution, it is not surprising that this eigenvector corresponds to essentially zero plasma displacement. Furthermore, due to the highly oscillatory nature of the mode, it is not surprising that the mode is highly damped ($\gamma < 200\,\mathrm{Hz}$).

It should be noted that the well-defined mode structure illustrated in Fig. 6.9 is largely a result of the simplicity of the plasma and wall shapes used in this example. For more complicated configurations, extensive coupling between the m-numbers is observed.

6.7.4 Normal Modes in the Presence of Feedback

To investigate the effect of feedback on the normal modes, a feedback voltage of the form given in Eq. (6.71) is applied to the upper PF coil ($k = 32$) shown in Fig. 6.7. No corresponding voltage is applied to the lower PF coil ($k = 33$). Both coils are assumed be made of copper and to have square cross sections with 0.05 m sides.

Figure 6.10 shows the effect of feedback on the distribution of normal mode frequencies. In the plots, the gain is increased from $G_{32} = 0$ to $G_{32} = 1800\,\mathrm{V/m}$ with the compensation held fixed at $\tau_{C32} = 0.05\,\mathrm{sec}$. Note that the plots only include those modes with $|\mathrm{Re}\,\gamma| < 150\,\mathrm{Hz}$ and $|\mathrm{Im}\,\gamma| < 150\,\mathrm{Hz}$ in order to better resolve the variation of the frequencies around $\mathrm{Re}\,\gamma = 0$ (the stability threshold). The modes not shown are all strongly damped.

With $G_{32} = 0$ (Fig. 6.10a) the PF coils both simply provide passive stabilization. This results in a slight reduction in the growth rate compared to the case when no coils are present. Increasing the gain to 200 V/m (Fig. 6.10b) leads to a further decrease in the positive growth rate. However, at the same time, the figure shows that a damped mode originally located at $\mathrm{Re}\,\gamma = -12\,\mathrm{Hz}$ has moved in the positive direction to $\mathrm{Re}\,\gamma = -7\,\mathrm{Hz}$. As

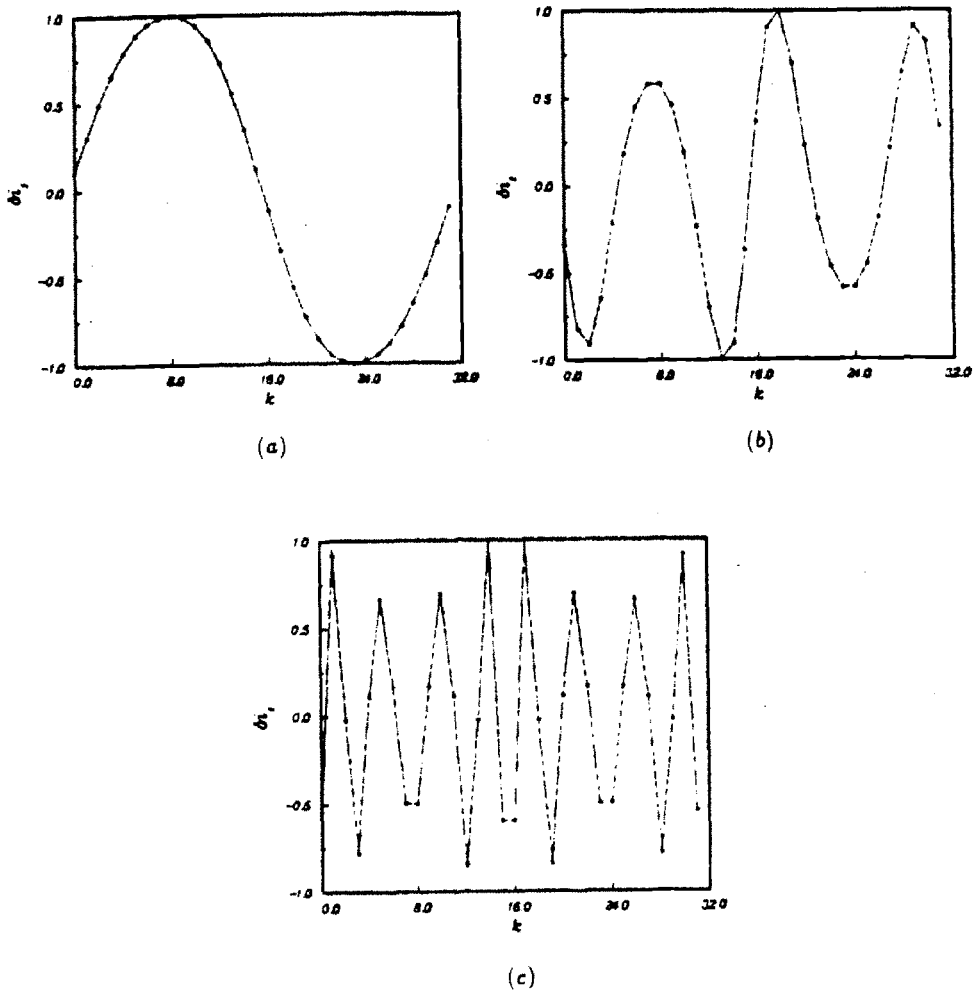

Figure 6.9: *Eigenvector plots for straight elliptical tokamak case: (a) dominant (growing) mode, (b) next largest (damped) mode, (c) smallest amplitude mode. In each case δI is plotted vs. the angular index k.*

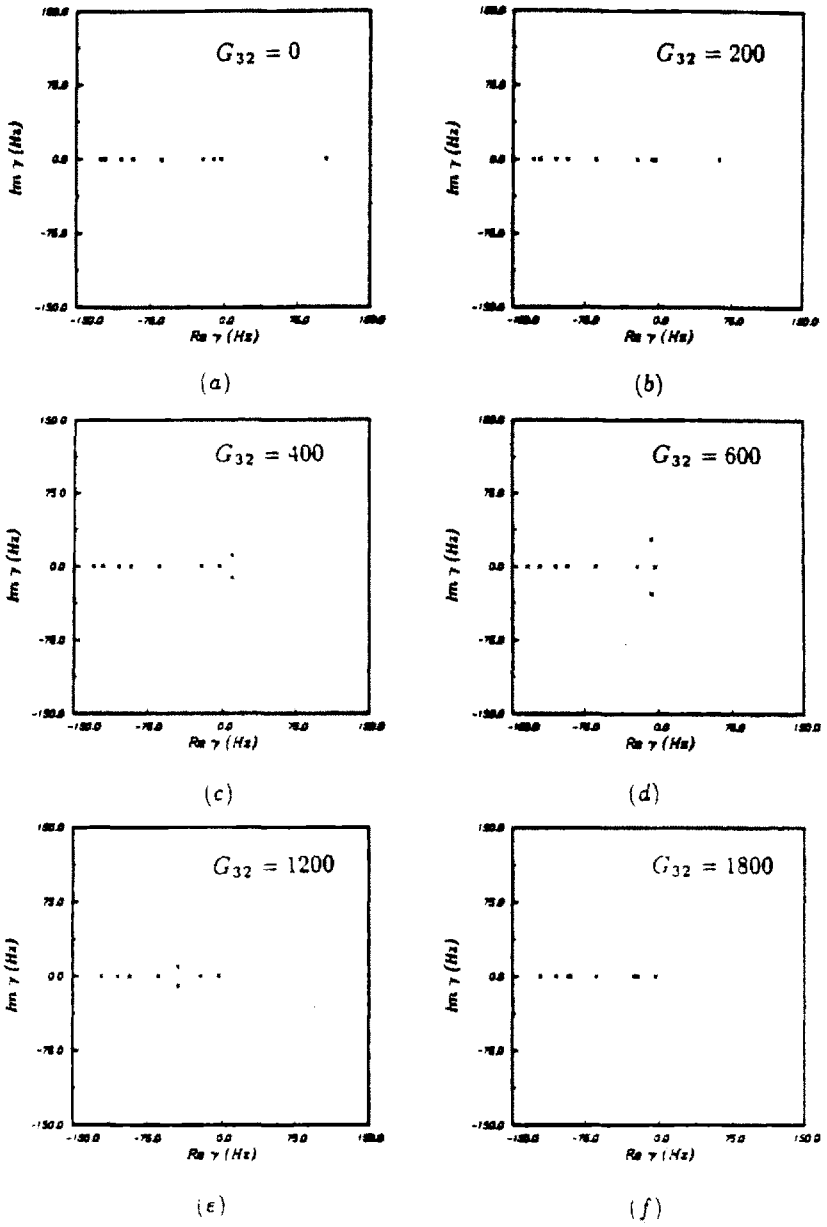

Figure 6.10: *Eigenvalue (γ) distributions for the straight elliptical tokamak case with feedback. Compensation held fixed at $\tau_{C32} = 0.05$ sec. Gain varies from plot to plot.*

the gain is further increased, this mode continues to move in the positive direction. In fact, when $G_{32} \approx 300\,\mathrm{V/m}$ the mode actually becomes unstable. For purposes of identification, these modes are called "feedback modes."

When $G_{32} \approx 370\,\mathrm{V/m}$, the originally growing mode and the formerly damped mode coalesce at $\gamma \approx 9\,\mathrm{Hz}$. As the gain is further increased, the modes move away from the $\mathrm{Re}\,\gamma$ axis as a complex conjugate pair. This is shown in Fig. 6.10c. Note as well that the real part of the growth frequency has continued to decrease.

Increasing the gain to $600\,\mathrm{V/m}$ (Fig. 6.10d) causes the real part of the frequencies to become negative. Hence, there are no more growing modes in the system. This shows that feedback can indeed give complete stability with respect to axisymmetric modes.

Further increases in the gain cause the imaginary parts of the modes to begin to decrease (Fig. 6.10e) until the modes eventually rejoin the $\mathrm{Re}\,\gamma$ axis at $\gamma = -41\,\mathrm{Hz}$ and begin to move in opposite directions along that axis (Fig. 6.10f). As the gain is increased to very high values, one mode moves to $\gamma = -20\,\mathrm{Hz} = -1/\tau_{C32}$ and the other moves to $\gamma = -2780\,\mathrm{Hz}$.

The initial spectral behavior of these feedback modes is consistent with results obtained in other studies. The behavior of the modes once they become damped is a complicated function of the various mutual inductances and resistances that characterize the system. For other types of systems, it is sometimes found that increasing the gain to extremely high values eventually causes the modes to become unstable. This behavior, which is illustrated in Fig. 6.11, occurs because the inductances of the system eventually cause the feedback voltage to become out of phase with the displacement. Hence, rather than providing a restoring force, the feedback voltage actually becomes a driving force for the instability. The details of the spectral behavior at high gains have not been investigated in this thesis. In particular, the circumstances that result in the behavior shown in Fig. 6.10 as opposed to that shown in Fig. 6.11 have not been identified. However, it is suspected

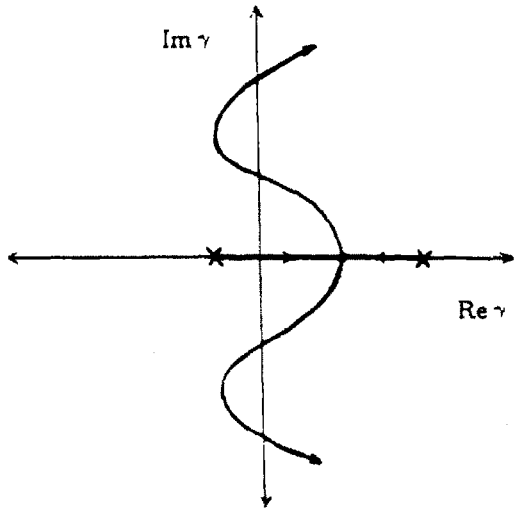

Figure 6.11: *Spectral behavior of feedback modes for a hypothetical system. The arrows give the direction the feedback modes move as gain is increased.*

that two factors that might be important are plasma inertia and vacuum chamber wall geometry.

As Fig. 6.10 showed, the γ's associated with the feedback modes display relatively complicated behavior as the gain is increased. However, many of the other modes move very little or not at all. The slowly moving modes were first identified by Humphreys and Hutchinson who named them 'quasi-constant' modes [93]. The exactly constant modes correspond to even-parity eigenvectors of the type shown in Fig. 6.9c. They are not affected by feedback since they correspond to normal modes of the vacuum chamber alone. Furthermore, the movement of the feedback modes in unaffected by the exactly constant modes since they represent orthogonal or unobservable modes of the system.

In addition to affecting the frequencies of the feedback modes, increasing the gain also has a large effect on the perturbed current distribution in the vacuum chamber wall. This is shown in Fig. 6.12 which displays the

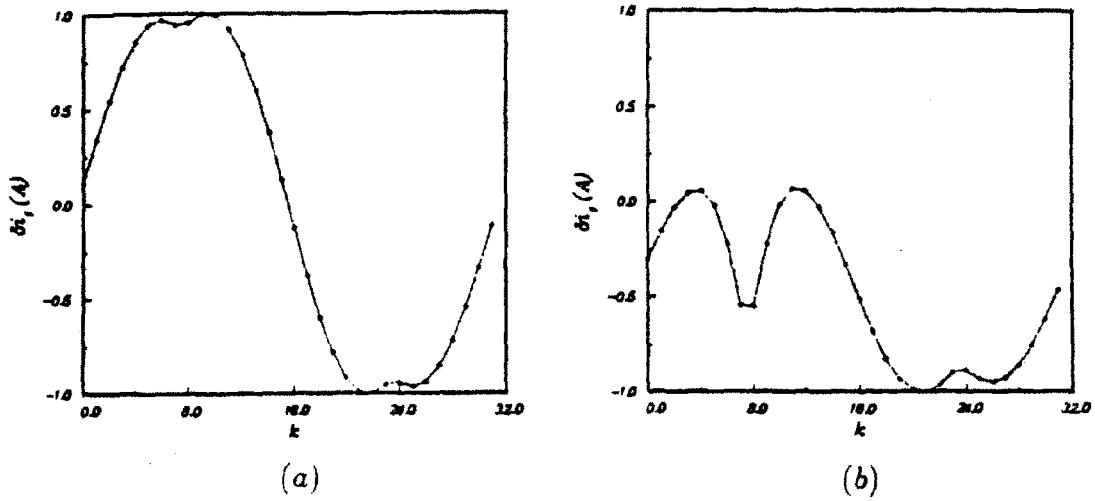

Figure 6.12: *Eigenvector plots for straight elliptical tokamak case with feedback: (a) no gain, (b)* $G_{32} = 350\ \mathrm{V/m}$.

perturbed current distributions corresponding to the growing feedback mode when $G_{32} = 0$ (Fig. 6.12a) and when $G_{32} = 350\,\mathrm{V/m}$ (Fig. 6.12b). Notice that even with no gain the distribution is modified somewhat from that shown in Fig. 6.9a. This is due to the substantial passive effects associated with the PF coils. Figure 6.12b shows that even a modest gain dramatically affects the perturbed currents, especially in the top half of the wall.

6.8 Effect of Non-Uniform Plasma Displacement

Up to now, all of the calculations have assumed a uniform vertical shift ($\nu = 0$) for the plasma displacement. In this section, we will investigate the physics and the effects of non-uniform displacements.

The physics of the non-uniform displacement can be explained quite simply using Fig. 6.13. This plot shows the vacuum field contours for a typical dee-shaped tokamak. Also shown are three current filaments ('a', 'b', and 'c')

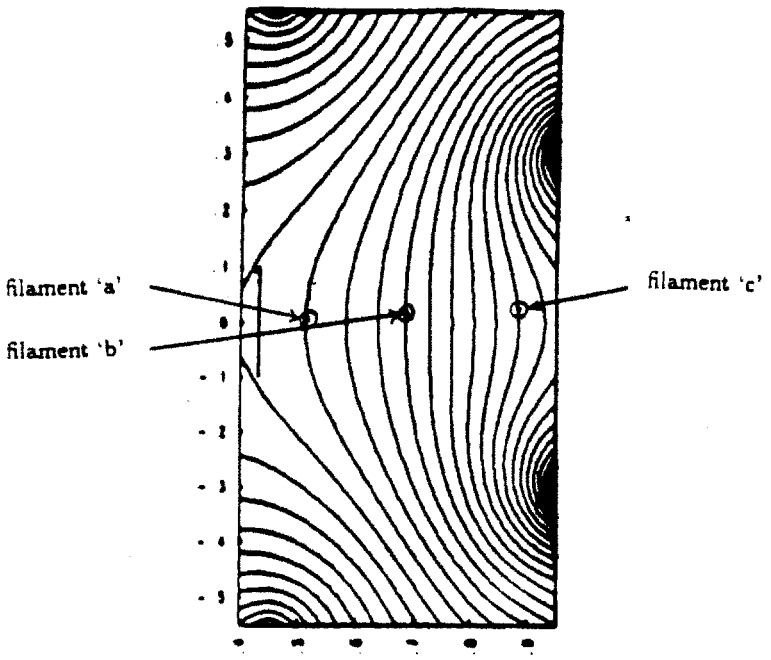

Figure 6.13: *Vacuum flux contours for a typical dee-shaped tokamak*

located on different field lines. The relative directions of the currents and the magnetic fields are set to ensure that the Lorentz ($\mathbf{J} \times \mathbf{B}$) force points radially inward. Assume now that filament 'a' is displaced by a small amount vertically upward. As the result of this displacement, the filament will be acted upon by a Lorentz force between the filament current and the R-component of the magnetic field. Since B_R points in the positive R-direction, the force acts upward, thus enhancing the instability. Therefore, the curvature of that field line is of a destabilizing nature. In contrast, the force acting on filament 'c' as a result of an upward vertical displacement points downward. Hence, the curvature of that field line is of a stabilizing nature. Similarly, the field line that filament 'b' lies on is seen to be neutrally stable.

The situation depicted in Fig. 6.13 is a common one; many tokamaks possess regions of good and bad field line curvature. The bad curvature is usually present on the inboard side of the torus and the good curvature is present on the outboard side. As the result of this observation, one might

Table 6.1: *Equilibrium Parameters for Investigation of Non-Uniform Displacements*

Parameter	Value
$a\,(\mathrm{m})$	0.21
$R_0\,(\mathrm{m})$	0.64
κ_a	2.0
δ_a	0.35
$B_0\,(\mathrm{T})$	9.0
α_p	-3.32
α_f	-2.0
$I_p\,(\mathrm{MA})$	2.7
b_p	0.001

expect that displacements peaked near the inboard side of the torus might be potentially more destabilizing than uniform shifts.

The expectation that non-uniform displacements are more destabilizing than uniform shifts is proven correct by Fig. 6.14. This plot shows the variation of γ with ν for a dee-shaped plasma (whose ePFC equilibrium parameters are given in Table 6.1) surrounded by a stainless steel wall with a shape parameterized by Eqs. (5.91) and (5.92). For this particular case, we take $t = 0.4$. Note that γ increases by almost a factor of three before reaching a maximum at $\nu = 1.9$. The effect of this displacement on the plasma shape can be seen by arbitrarily setting $\xi_Z = 0.2a$ and superimposing this perturbation on the points making up the plasma surface. The result is shown in Fig. 6.15.

Since the non-uniformity in the plasma displacement increases the passive growth rate, one might expect that the feedback gain required to stabilize the system would increase as well. This question is addressed using Fig. 6.16. Here, we assume the existence of two PF coils located at $R = 0.64\,\mathrm{m}$, $Z =$

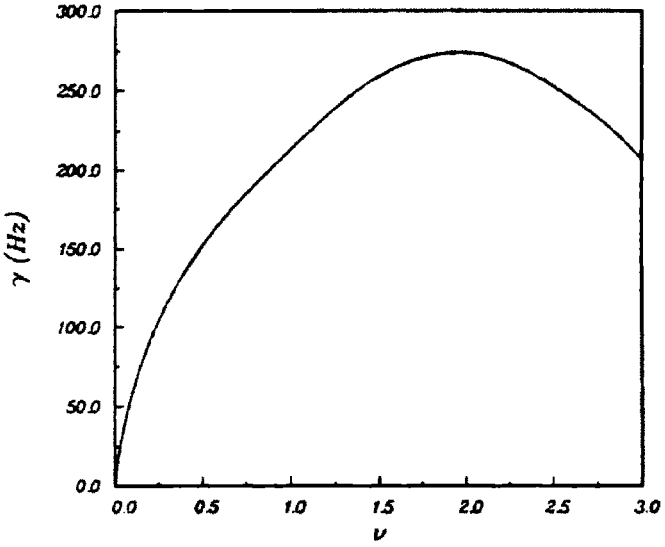

Figure 6.14: *Variation of γ with ν for dee-shaped tokamak.*

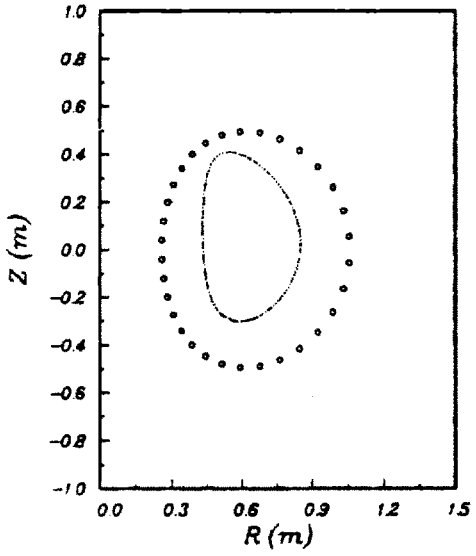

Figure 6.15: *Effect of non-uniform displacement on plasma surface shape.*

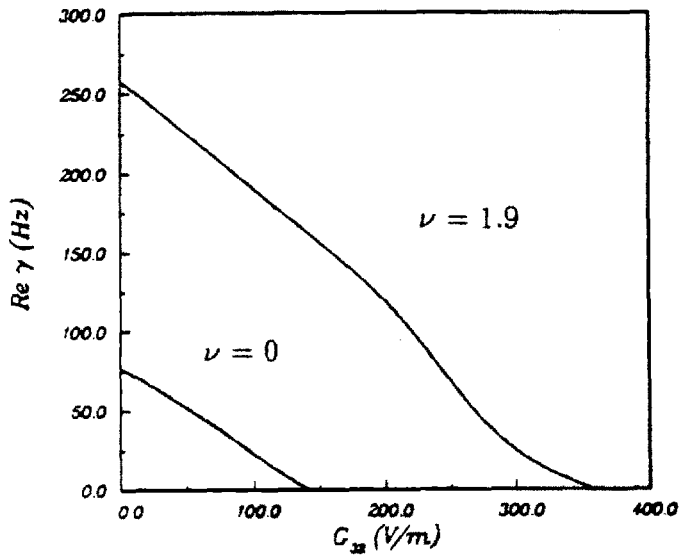

Figure 6.16: *Variation of Reγ with feedback gain G_{32} for dee-shaped plasma for $\nu = 0$ and $\nu = 1.9$.*

± 0.7 m. Each coil is made of copper and has a square cross-section with 0.05 m sides. A feedback voltage is applied only to the top coil ($k = 32$) and the compensation is fixed at $\tau_{C32} = 0.05$ sec. The figure shows the real part of γ plotted as a function of the feedback gain for two values of ν: $\nu = 0$ and $\nu = 1.9$. We see that the non-uniform shift requires a significantly larger gain to reduce γ to zero (i.e. stabilize the mode). This means that consideration of only uniform shifts could lead to a large underestimation of the feedback power supply requirements.

The amount of de-stabilization associated with ν is a complicated function of wall geometry and plasma shape. However, one parameter that seems to have a particularly strong effect is triangularity. To assess the impact of triangularity on vertical stability in the presence of a non-uniform displacement, we will consider a series of equilibria with parameters as given in Table 6.1 but with δ_a varying between 0.0 and 0.5. These plasmas are assumed to be surrounded by walls parameterized by Eqs. (5.91) and (5.92). In Fig. 6.17,

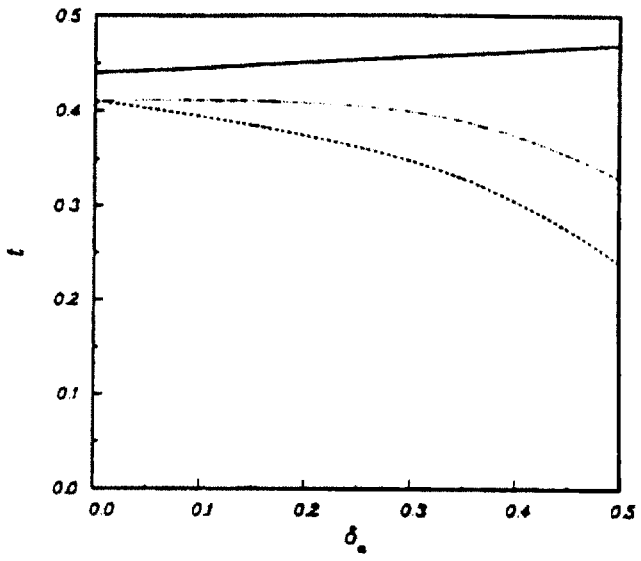

Figure 6.17: *Plot of marginal wall position (t) as a function of δ_a for dee-shaped tokamak. Three curves are shown: (a) ePFC equilibrium, vPFC stability, $\nu = 0$ (dashed line); (b) ePFC equilibrium, vPFC stability, ν chosen to maximize γ (dotted line); (c) NEQ equilibrium, GATO stability (solid line).*

we plot the minimum value of t necessary to ensure ideal stability — the marginal wall position — as a function of δ_a. Three curves are presented. The first curve was generated using ePFC to compute the equilibrium and vPFC to compute the stability with $\nu = 0$. The second curve was also generated using ePFC and vPFC; however, the value of ν used is that which maximizes γ. The third curve was generated using the exact equilibrium code NEQ to provide input to the ideal MHD code GATO. Hence, for this curve, the plasma displacement is in some sense "exact."

For the ePFC/vPFC curve with $\nu = 0$, the critical value of t decreases with δ_a indicating that the marginal wall position moves outward with increasing δ_a. Hence, this curve implies that triangularity has a stabilizing effect on stability. This is consistent with the results of Fig. 5.7 which shows that γ decreases with δ_a in the straight limit.

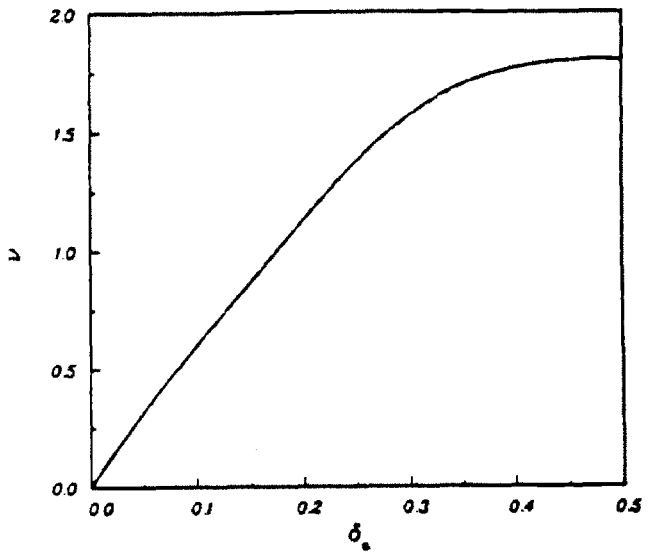

Figure 6.18: *Variation of ν leading to maximum γ with δ_a.*

The ePFC/vPFC curve with ν chosen to maximize γ again shows that triangularity is a stabilizing effect. However, in this case, the stabilizing influence is reduced, especially at high values of δ_a. This occurs because the plasma displacement becomes non uniform as δ_a increases. This is shown in Fig. 6.18 which displays the value of ν that maximized γ as a function of δ_a. Note that, as expected, the most unstable displacement is a uniform shift only for the case when $\delta_a = 0$. As δ_a is increased, ν also increases (though at a much smaller rate for $\delta_a > 0.35$). It should be emphasized that at high triangularities the effect of the non-uniformity in the displacement is substantial. In particular, for some range of wall positions, the uniform shift model predicts stability on the resistive wall time scale when, in fact, the plasma is unstable on the ideal MHD timescale to non-uniform displacements.

The ePFC/vPFC curve with $\nu \neq 0$ scales relatively closely to the NEQ/GATO curve for $\delta_a < 0.4$. On the other hand, the $\nu = 0$ curve deviates

dramatically as δ_a is increased. This is another example of the inaccuracies associated with the uniform shift model.

One of the most striking features of Fig. 6.17 is that, in contrast to the ePFC/vPFC curves, the NEQ/GATO curve shows that increasing triangularity is actually a mild destabilizing effect. This behavior is probably not due to artificial numerical errors since special care was taken to avoid such effects. Furthermore, this result is supported by the work of Bernard, *et al.*[20] who used the ERATO [94] MHD stability code to conclude that triangularity is detrimental to the stability of $n = 0$ modes. The discrepancy between the ePFC/vPFC and NEQ/GATO results is probably due to a combination of three factors.

The first possible cause for the discrepancy between the ePFC/vPFC and NEQ/GATO results is the approximate nature of the ePFC equilibrium. It is plausible to expect that the differences between the ePFC and NEQ equilibria could affect the stability results. However, Fig. 5.7 suggests that these errors are probably relatively small. The second possible cause for the discrepancy is the error associated with sensing the marginal wall position using vPFC. This error ultimately results from the neglect of plasma inertia in the vPFC formulation. As a result of this assumption, the marginal wall position is found by locating the value of t that causes γ to become infinite (or at least very large). Since the neglect of plasma inertia is clearly invalid at large, but finite, values of γ it is not possible to know exactly when γ has grown large enough to to signal ideal instability. Luckily, the variation of γ with t near the marginal point is extremely fast. This allows us to estimate that this effect gives an error in t no more than $\Delta t < 0.02$. We would not expect that these two sources of error would yield opposite trends in the variation of t with δ_a.

The third, and probably major, cause for the discrepancy between the ePFC/vPFC and NEQ/GATO curves is the difference between the exact GATO displacement and the simple displacement trial function given in

Eq. (6.38). Examination of the unstable GATO displacement eigenfunctions indicates that Eq. (6.38) is a relatively good approximation when $\delta_a < 0.4$. However, experience has shown that subtle differences is the displacements can lead to a finite variation in the marginal wall position. One way to investigate this effect would be to substitute the exact GATO displacement into vPFC. Unfortunately, current versions of the vPFC code cannot accommodate such general displacements. When $\delta_a > 0.4$, the simple trial function in Eq. (6.38) becomes a less accurate approximation. This is illustrated in Fig. 6.19 which shows the GATO displacement eigenfunction for the $\delta_a = 0.5$ case. Note that the displacement appears to peak along the plasma surface and to vary with the Z-coordinate. Moreover, the displacement is not purely vertical everywhere. This suggests that to accurately model strongly shaped plasmas more elaborate trial functions are needed.

As a final note, approximately 3–5 minutes of Cray CPU time were needed to generate each of the points for the NEQ/GATO curve. This corresponds to a single run of NEQ to generate the equilibrium followed by 3–6 runs of GATO with different wall positions to find the marginal point. The corresponding CPU requirement for the ePFC/vPFC curves is 10–20 sec for the $\nu = 0$ points and 25–40 sec for the $\nu \neq 0$ points.

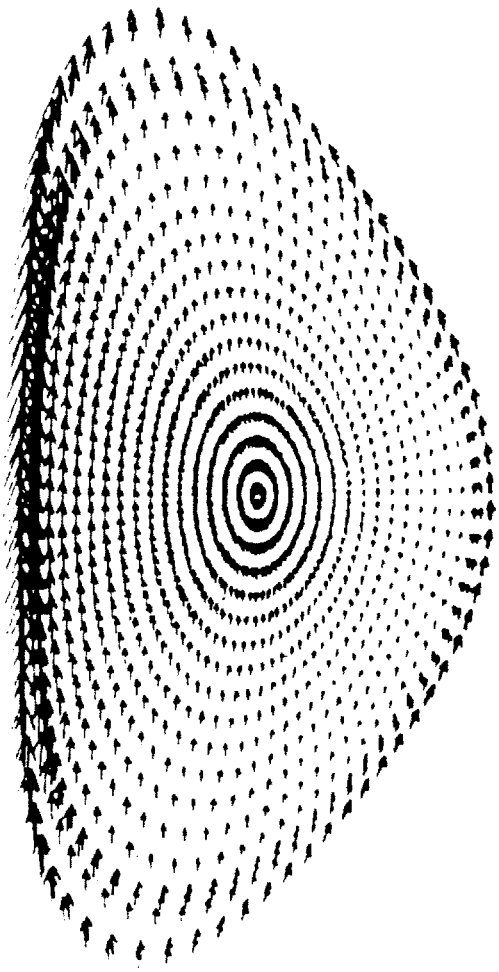

Figure 6.19: *Exact GATO eigenfunction for dee-shaped plasma ($\kappa_a = 2$, $\delta_a = 0.5$). The arrows give the local direction and magnitude of ξ.*

Appendix A

Derivation of the Inverse Grad-Shafranov Equation

In this appendix we transform the Grad-Shafranov equation from normal cylindrical (R, φ, Z) coordinates to inverse (ρ, φ, μ) coordinates. Recall that the Grad-Shafranov equation can be written

$$\psi_0 \left(\tilde{\psi}_{RR} + \tilde{\psi}_{ZZ} - \frac{1}{R} \tilde{\psi}_R \right) = -\mu_0 R J_\varphi(R, \tilde{\psi}), \tag{A.1}$$

where, for simplicity, subscripts have been used to denote partial differentiation.

Using the chain rule, we can simply obtain relations between derivatives in cylindrical coordinates and inverse coordinates:

$$\frac{\partial}{\partial R} = \frac{Z_\mu}{J} \frac{\partial}{\partial \rho} - \frac{Z_\rho}{J} \frac{\partial}{\partial \mu}, \tag{A.2}$$

$$\frac{\partial}{\partial Z} = -\frac{R_\mu}{J} \frac{\partial}{\partial \rho} + \frac{R_\rho}{J} \frac{\partial}{\partial \mu}, \tag{A.3}$$

where J is the Jacobian for the transformation defined

$$J = R_\rho Z_\mu - Z_\rho R_\mu. \tag{A.4}$$

With these relations, we can easily compute the first partials of $\tilde{\psi}$

$$\tilde{\psi}_R = \frac{1}{J}\left(Z_\mu \tilde{\psi}_\rho - Z_\rho \tilde{\psi}_\mu\right), \tag{A.5}$$

$$\tilde{\psi}_Z = \frac{1}{J}\left(R_\mu \tilde{\psi}_\rho - R_\rho \tilde{\psi}_\mu\right). \tag{A.6}$$

Furthermore, a little algebra yields the second partials

$$\tilde{\psi}_{RR} = \frac{1}{R}\tilde{\psi}_R + \frac{R}{J}\left\{\left[\frac{Z_\mu \tilde{\psi}_R}{R}\right]_\rho - \left[\frac{Z_\rho \tilde{\psi}_R}{R}\right]_\mu\right\}, \tag{A.7}$$

$$\tilde{\psi}_{ZZ} = -\frac{R}{J}\left\{\left[\frac{R_\mu \tilde{\psi}_Z}{R}\right]_\rho - \left[\frac{R_\rho \tilde{\psi}_Z}{R}\right]_\mu\right\}. \tag{A.8}$$

By substituting Eqs. (A.7) and (A.8) into Eq. (A.1) we finally obtain the inverse Grad-Shafranov equation

$$\left[\frac{Z_\mu \tilde{\psi}_R - R_\mu \tilde{\psi}_Z}{R}\right]_\rho - \left[\frac{Z_\rho \tilde{\psi}_R - R_\rho \tilde{\psi}_Z}{R}\right]_\mu = -\mu_0 J J_\varphi(\rho, \mu, \tilde{\psi}), \tag{A.9}$$

where $\tilde{\psi}_R$ and $\tilde{\psi}_Z$ are given by Eqs. (A.5) and (A.6).

Appendix B

Poloidal Field Circuit Finite Differencing Procedure

In this appendix, we describe the straightforward procedure used to finite difference various poloidal field circuit elements into a series of thin circular conductors. The cases of the PF/OH coils and the vacuum chamber wall are considered separately.

B.1 PF/OH Coils

The finite differencing of the PF and OH coils is extremely easy. For simplicity, we replace each PF/OH coil with a single thin circular conductor located at the same position (R_j, Z_j) as the original coil. Higher accuracy could be achieved by using more than one conductor to represent a given coil; however, for most applications, a single coil suffices.

The goal of the procedure is to reproduce the resistance and the external self-inductance of the original coil. Assuming that the coil has a rectangular cross-section of width w_j and height h_j, the resistance is found to be

$$\frac{1}{r_j} = \frac{h_j \sigma_j}{2\pi} \ln\left(\frac{R_j + \frac{1}{2}w_j}{R_j - \frac{1}{2}w_j}\right), \tag{B.1}$$

where σ_j is the conductivity of the material making up the coil. In principle, the external self-inductance is much harder to compute. However, we simply use the value that would be obtained if the rectangular coil were replaced with a large aspect ratio circular conductor with the same cross-sectional area:

$$\ell_j = \frac{\mu_0 R_j}{2\pi}\left[\ln\left(\frac{8\pi^{1/2}R_j}{(h_j w_j)^{1/2}}\right) - 2\right]. \tag{B.2}$$

B.2 Vacuum Chamber Wall

It is only somewhat more involved to finite difference the vacuum chamber wall. We assume that the inner surface of the wall is parameterized by $R = R_w(\mu)$, $Z = Z_w(\mu)$ where μ is the usual angular coordinate. We further assume that the wall has a thickness d and that $d \ll \bar{b}$ where $\bar{b}$ is the average radius of the wall. This is simply the thin wall assumption originally discussed in Chapter 5.

To finite difference the vacuum chamber wall into J conductors, it is necessary to break the wall into a number of segments. This is shown schematically in Fig. B.1. We replace each of the segments with a single conductor.

The conductor is located at the centroid of the wall segment it replaces. The coordinates of this centroid are given by

$$R_j = \frac{1}{L_j}\int_{\mu_j}^{\mu_{j+1}} R_w(\mu)\, Q_w(\mu)\, d\mu, \tag{B.3}$$

$$Z_j = \frac{1}{L_j}\int_{\mu_j}^{\mu_{j+1}} Z_w(\mu)\, Q_w(\mu)\, d\mu, \tag{B.4}$$

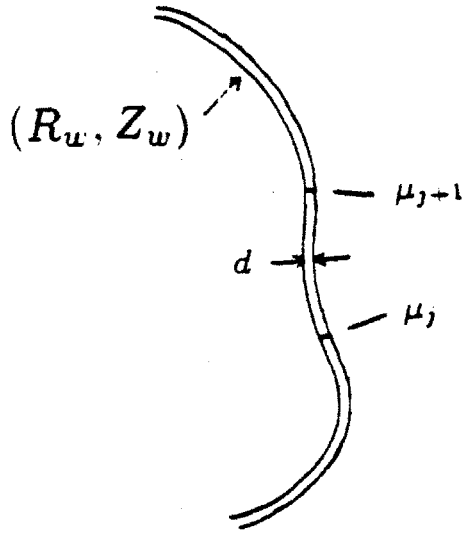

Figure B.1: *Vacuum chamber wall finite differencing scheme.*

where

$$Q_w = \sqrt{\left(\frac{dR_w}{d\mu}\right)^2 + \left(\frac{dZ_w}{d\mu}\right)^2}, \tag{B.5}$$

and

$$L_j = \int_{\mu_j}^{\mu_{j+1}} Q_w(\mu)\, d\mu. \tag{B.6}$$

The resistance of the conductor is simply written

$$r_j = \frac{2\pi R_j}{\sigma_j A_j}, \tag{B.7}$$

where A_j is the cross-sectional area of the segment given by

$$A_j = L_j\, d. \tag{B.8}$$

The external self-inductance of the conductor is again written using the thin circular assumption

$$\ell_j = \frac{\mu_0 R_j}{2\pi}\left[\ln\left(\frac{8\pi^{1/2}R_j}{A_j^{1/2}}\right) - 2\right]. \tag{B.9}$$

Bibliography

[1] FURTH, H.P., Nucl. Fusion **15** (1975) 487.

[2] FREIDBERG, J.P., Ideal Magnetohydrodynamics, Plenum Press (1987) 426.

[3] SYKES, A., TURNER, M.F., PATEL, S., in Controlled Fusion and Plasma Physics (Proc. 11th Europ. Conf. Aachen, 1983), Vol. 2, European Physical Society (1983) 363.

[4] YAMAZAKI, K., AMANO, T., NAITOU, H., HAMADA, Y., AZUMI, M., Nucl. Fusion **25** (1985) 1543.

[5] TROYON, F., GRUBER, R., SAURENMANN, H., SEMENZATO, S., SUCCI, S., Plasma Physics and Controlled Fusion **26** 1A (1984) 209.

[6] BERNARD, L.C., HELTON, F.J., MOORE, R.W., TODD, T.N., Nucl. Fusion **23** (1983) 1475.

[7] STAMBAUGH, R.D., MOORE, R.W., BERNARD, L.C.,KELLMAN, A.G., in Controlled Fusion and Plasma Physics (Proc. 10th Europ. Conf. London, 1984), Vol. 1, European Physical Society (1984) 217.

[8] STRAIT, E.J., *et al.*, Contributed paper at the 29th Annual Meeting of the Division of Plasma Physics, American Physical Society, San Diego, CA (1987) (unpublished).

[9] BAKER, C.C., ABDOU, M.A., DEFREECE, D.A., TRACHSEL, C.A., GRAUMANN, D.W., *et al.*, STARFIRE, A Commercial Tokamak Power Plant Study, Argonne National Lab. Report ANL/FPP-80-1 (1980).

[10] LECLAIRE, R.J., Conceptual Design of a Commercial Reactor Using Resistive Magnets, M.I.T. Plasma Fusion Center Report PFC/RR-86-17 (1986).

[11] SHEFFIELD, J., DORY, R.A., COHN, S.M., DELENE, J.G., PARSLY, L., Cost Assessment of a Generic Magnetic Fusion Reactor, Oak Ridge National Lab. Report ORNL-TM-9311 (1985).

[12] MURAKAMI, M., CALLEN, J.D., BERRY, L.A., Nucl. Fusion **16** (1976) 347.

[13] GRAD, H., RUBIN, H., in Proceedings of the Second United Nations International Conference on the Peaceful Uses of Atomic Energy, United Nations, Geneva, Vol. 31 (1958) 42.

[14] SHAFRANOV, V.D., Sov. Phys.-JETP **26** (1960) 682.

[15] MATHEWS, J., WALKER, R.L., Mathematical Methods of Physics, 2nd ed., Benjamin/Cummings Publishing Company (1970) 260.

[16] WESSON, J.A., Nucl. Fusion **18** (1978) 87.

[17] LAVAL, G., PELLAT, R., SOULE, J.S., Phys. Fluids **17** (1974) 835.

[18] DEWER, R.L., GRIMM, R.C., JOHNSON, J.L., FRIEMAN, E.A., GREENE, J.M., RUTHERFORD, P.H., Phys. Fluids **17** (1974) 930.

[19] HAAS, F.A., Nucl. Fusion **15** (1975) 407.

[20] BERNARD, L.C., BERGER, D., GRUBER, R., TROYON, F., Nucl. Fusion **18** (1978) 1331.

[21] GRAUER, R., REBHAN, E., J. Plasma Phys. **32** (1984) 99.

[22] STRATTON, J.A., Electromagnetic Theory, McGraw-Hill (1941) 250.

[23] HIVELY, L.M., Nucl. Fusion **17** (1977) 873.

[24] PARKER, R.R., GREENWALD, M., LUCKHARDT, S.C., MARMAR, E.S., PORKOLAB, M., WOLFE, S.M.,Nucl. Fusion **25** (1985) 1127.

[25] SCHMIDT, J.A., SHEFFIELD, G.V., BUSHNELL, C., CITROLO, J., FLEMING, R., *et al.*, in Controlled Fusion and Plasma Physics (Proc. 10th Europ. Conf. London, 1984), Vol. 3, European Physical Society (1984) 297.

[26] KAYE, S.M., GOLDSTON, R.J., Nucl. Fusion **25** (1985) 63.

[27] BORRASS, K., Nucl. Eng. Design/Fusion, Vol. 4, No. 3 (1987) 247.

[28] SPEARS, W.R., WESSON, J.A., Nucl. Fusion **20** (1980) 1525.

[29] LECLAIRE, R.J., private communication (1985).

[30] COPPI, B., Phys. Rev. Lett. **39** (1977) 939.

[31] GRIMM, R.C., CHANCE, M.S., TODD, A.M.M., MANICKAM, J., *et al.*, MHD Stability Properties of Bean Shaped Tokamaks, Princeton Plasma Physics Lab. Report 2090 (1984).

[32] OKABAYASHI, M., SHEFFIELD, G., Nucl. Fusion **14** (1974) 263.

[33] LAWSON, J.D., Proc. Phys. Soc. (London) **B70** (1957) 6.

[34] SMITH, D.L., MORGAN, G.D., ABDOU, M.A., BAKER, C.C., BERWALD, D.H., *et al.*, Blanket Comparison and Selection Study Final Report, Argonne National Lab. Report ANL/FPP-84-1 (1984).

[35] FREIDBERG, J.P., WESSON, J.A., Nucl. Fusion **25** (1985) 759.

[36] PENG, Y-K.M., Spherical Torus, Compact Fusion at Low Field, Oak Ridge National Lab. Report ORNL/FEDC-84/7 (1985).

[37] CHU, M.S., HARVEY, R.W., POLITZER, P.A., YAMAGISHI, T., Nucl. Fusion **25** (1985) 835.

[38] HILDEBRAND, F.B., Advanced Calculus for Applications, Prentice-Hall (1976).

[39] MUKHOVATOV, V.S., SHAFRANOV, V.D., Nucl. Fusion **11** (1971) 605.

[40] SHAFRANOV, V.D., in Reviews of Plasma Physics, edited by M.A. Leontovich, Consultants Bureau, Vol. 2 (1966) 103.

[41] WARE, A.A, HAAS, F.A., Phys. Fluids **9** (1966) 956.

[42] SOLEV'EV, L.S., Sov. Phys.-JETP **26** (1968) 400.

[43] HAAS, F.A., Phys. Fluids **15** (1972) 141.

[44] FREIDBERG, J.P., HAAS, F.A., Phys. Fluids **16** (1973) 1909.

[45] STRICKLER, D.J., MILLER, F.B., ROTHE, K.E., PENG, Y.-K.M., Equilibrium Modeling of the TFCX Poloidal Field Coil System, Oak Ridge National Lab. Report ORNL/FEDC-83/10 (1984).

[46] GRIMM, R.C., GREENE, J.M., JOHNSON, J.L., Meth. Comput. Phys. **16** (1976) 253.

[47] GRIMM, R.C., DEWAR, R.L., MANICKAM, J., J. Comput. Phys. **49** (1983) 94.

[48] HELTON, F.J., WANG, T.S., Nucl. Fusion **18** (1978) 1523.

[49] WEINSTOCK, R., Calculus of Variations, Dover (1952).

[50] LAO, L.L, HIRSHMAN, S.P., WIELAND, R.W., Phys. Fluids **24** (1981) 1431.

[51] LAO, L.L, GREENE, J., WANG, T.S., HELTON, F.J., ZAWADZKI, E.M., Phys. Fluids **28** (1985) 869.

[52] CHOE, W.H., FREIDBERG, J.P., Phys. Fluids **29** (1986) 1766.

[53] GREENE, J.M., JOHNSON, J.L., WEIMER, K.E., Phys. Fluids **14** (1971) 671.

[54] HAKKARAINEN, S.P., Equilibrium and Stability Studies of Strongly Shaped Tokamaks, Ph.D Thesis, Massachusetts Institute of Technology (1988).

[55] PRESS, W.H., FLANNERY, B.P. TEUOLSKY, S.A., VETTERING, W.T., Numerical Recipes in C, Cambridge University Press (1988) **290**.

[56] HARBISON, S.P., STEELE, G.L., C: A Reference Manual, 2nd ed., Prentice-Hall (1987).

[57] PAULSON, C., TODD, A.M.M., computer code *PGREEN*.

[58] FREIDBERG, J.P., HAAS, F.A., Phys. Fluids **17** (1974) 440.

[59] FREIDBERG, J.P., GROSSMAN, W., Phys. Fluids **18** (1975) 1494.

[60] FREIDBERG, J.P.,GROSSMAN, W., HAAS, F.A., Phys. Fluids **19** (1976) 1599.

[61] HAKKARAINEN, S.P., FREIDBERG, J.P., Reconstruction of Vacuum Flux Surfaces from Diagnostic Measurements in a Tokamak, M.I.T. Report PFC/RR-87-2 (1987).

[62] HAKKARAINEN, S.P., private communication (1987).

[63] ABRAMOWITZ M., STEGUN, I.A., Handbook of Mathematical Functions, 10th ed., U.S. Department of Commerce (1972) 591.

[64] PRESS, W.H., FLANNERY, B.P. TEUOLSKY, S.A., VETTERING, W.T., Numerical Recipes in C, Cambridge University Press (1988) 29.

[65] GILL, P.E., MURRAY, W., WRIGHT, M.H., Practical Optimization, 4th ed., Academic Press/Harcourt-Brace-Jovanovich (1984) 67.

[66] GOLUB, G.H., SIAM Review, **15** (1973) 318.

[67] PRESS, W.H., FLANNERY, B.P. TEUOLSKY, S.A., VETTERING, W.T., Numerical Recipes in C, Cambridge University Press (1988) 398.

[68] HELTON, F.J., GREENE, J.M., HELTON, J.W., On Necessary Conditions for Building a Large Non-circular Cross-section Tokamak, GA Technologies, Inc. Report GA-A18814 (1987).

[69] HELTON, F.J., GREENE, J.M., Contributed paper at the 1988 Sherwood Theory Conference, Gatlinburg, TN (1988) (unpublished).

[70] BERNSTEIN, I.B., FRIEMAN, E.A., KRUSKAL, M.D., KULSRUD, R.M., Proc. R. Soc. London, Ser. A **244** (1958) 17.

[71] WESSON, J.A., in Controlled Fusion and Plasma Physics (Proc. 7th Europ. Conf. Lausanne, 1975), Vol. 2, European Physical Society (1975) 102.

[72] JARDIN, S.C., Phys. Fluids **21** (1978) 10.

[73] FURTH, H.P., KILEEN, J., ROSENBLUTH, M.N., Phys. Fluids **6** (1963) 459.

[74] FREIDBERG, J.P., Ideal Magnetohydrodynamics, Plenum Press (1987) 307.

[75] PEARLSTEIN L.D., FREIDBERG, J.P., Phys. Fluids **21** (1978) 1207.

[76] LAVAL G., PELLAT R., in Controlled Fusion and Plasma Physics (Proc. 6th Europ. Conf. Moscow, 1973), Vol. 2, European Physical Society (1973) 640.

[77] REBHAN, E., Nucl. Fusion **15** (1975) 277.

[78] RAMOS, J.J., Contributed paper at the 1986 Sherwood Theory Conference, New York, NY (1986) (unpublished).

[79] JARDIN, S.C., LARABEE, D.A., Nucl. Fusion **22** (1982) 1095.

[80] NAGAYAMA, Y., OHKI, Y., MIYAMOTO, K., Nucl. Fusion **23** (1983) 1447.

[81] JENSEN, T.H., MCCLAIN, F.W., J. Plasma Phys. **32** (1984) 399.

[82] NEILSON, G.H., DYER, G.R., EDMONDS, P.H., Nucl. Fusion **24** (1984) 10.

[83] JARDIN, S.C., DELUCIA, J., OKABAYASHI, M., POMPHREY, N., REUSCH, M., *et al.*, Nucl. Fusion **27** (1987) 569.

[84] MORI, M., SUZUKI, N., SHOJI, T., YANAGISAWA, I., TANI, T., MATSUZAKI, Y., Nucl. Fusion **27** (1987) 725.

[85] THOME, R.J., PILLSBURY, R.D., MONTGOMERY, D.B., POLITZER, P.A., WOLFE, S.M., *et al.*, Passive and Active Circuits for Vertical Plasma Stabilization, M.I.T. Plasma Fusion Center Report PFC/RR-83-82 (1983).

[86] HUMPHREYS, D.A., HUTCHINSON, I.H., Contributed paper at the 28th Annual Meeting of the Division of Plasma Physics, American Physical Society, Baltimore, MD (1986) (unpublished).

[87] JARDIN, S.C., POMPHREY, N., DELUCIA, J., J. Comp. Phys. **66** (1986) 481.

[88] BERNARD, L.C., HELTON, F.J., MOORE, R.W., Comput. Phys. Commun. **24** (1980) 377.

[89] HOFFMANN, F., TURNBULL, A.D., MARCUS, F.B., Nucl. Fusion **27** (1987) 743.

[90] REBHAN, E., SALAT, A., Nucl. Fusion **16** (1976) 805.

[91] HUMPHREYS, D.A., private communication (1988).

[92] KESSEL, C.E., Linear Optimal Control of Plasma Shape, Position, and Current in a Tokamak Fusion Reactor, Ph.D Thesis, University of California, Los Angeles (1987).

[93] HUMPHREYS, D.A., HUTCHINSON, I.H., Contributed paper at the 29th Annual Meeting of the Division of Plasma Physics, American Physical Society, San Diego, CA (1987) (unpublished).

[94] CHANCE, M.S., GREENE, J.M., GRIMM, R.C., JOHNSON, J.J., MANICKAM, J., *et al.* J. Comp. Phys. **28** (1978) 333.